9-6-2019 3:00 PM

Shape-Controlled Nanoparticles as Effective Catalysts for Proton Exchange Membrane (PEM) Fuel Cells

Ali Feizabadi, *The University of Western Ontario*

Supervisor: Sham, Tsun-Kong, *The University of Western Ontario*
Joint Supervisor: Sun, Xueliang, *The University of Western Ontario*
A thesis submitted in partial fulfillment of the requirements for the Master of Science degree in Chemistry

Abstract

Polymer electrolyte membrane fuel cell (PEMFC), is considered a promising candidate for the next generation power sources in transportation, stationary and portable applications. However, oxygen reduction reaction (ORR), one of the key reactions occurring on PEMFC is kinetically slow; this has limited performance and further advancement in this kind of fuel cells. Thus, improving the PEMFC efficiency requires a thorough understanding of the ORR mechanism on the desired catalyst. To address the above-mentioned demands, the scope of this thesis is focused on the fundamental understanding of facet-controlled nanoparticles, metal-support interactions, and bimetallic platinum catalysts, utilizing synchrotron-based X-ray absorption, X-ray photoelectron spectroscopy, and electrochemical characterization methods.

It is found that particle size, shape, composition (Pd and Co are the other metals), and the supporting material not only can act as momentous parameters in enhancing the catalytic activity of NPs but also are functioning as vital criteria in boosting the stability.

Keywords

Oxygen reduction reaction (ORR), Polymer electrolyte membrane (PEM) fuel cell, X-ray absorption fine structure (XAFS), Electronic structure, Metal-Support interaction, Catalytic activity

Summary for Lay Audience

Climate change and deficiency of petroleum-based energy resources have risen concerns about the future of planet earth and have made scientist to be more focused on fuel cell technologies, due to their low emissions and high efficiencies. Low operation temperature, high power, and energy density have made the PEMFC, a promising candidate for the next generation power sources in transportation, stationary and portable applications. Low abundance, limited supply, and increasing demand have limited the commercial application of Pt, as a critical catalytic component in PEMFC. So finding out an efficient catalyst and substituting it with the current commercial ones can accelerate the utilization of this technology and can cease the current concerns about the climate change crises. DFAFCs as a subcategory of PEM fuel cells have also attracted lots of attentions in recent years due to their high energy conversion efficiency and non-toxic and safe fuel. The low stability of palladium, as a catalyst for DFAFC has also diminished its commercial applications and catalysts with higher stability will be required. This study will discuss more fundamentally the ways for satisfying the mentioned demands.

To my family

Acknowledgments

I take this opportunity to extend my gratitude to everyone who has played a role in my journey towards a master degree. Foremost, I would like to express my sincere gratitude and appreciation to my supervisors, Professor Tsun-Kong (T.K.) Sham and Professor Xueliang (Andy) Sun, for their guidance, advice, availability, and support from the beginning of the program to the completion of this thesis. It was a great privilege and honor to work and study under their guidance. Graduate school would have been much tougher without their always-positive encouragement.

I also want to thank Dr. Lei Zhang for his guidance on the review and kind assistance throughout the duration of this thesis. I would also like to express my gratitude to Dr. Mohammad Norouzi Banis for his advice on the research and thesis. It has been a great pleasure to work with such a knowledgeable and passionate mentor in my academic life. I also thank Mr. Jiatang Chen who has constantly provided invaluable assistance, advice, and friendship. I also thank Dr. Yun-Mui Yiu who has provided tremendous assistance and informative insights on the data simulation;

In addition, I would like to acknowledge the rest of the laboratory members: Dr. Zhiqiang Wang, Dr. Madalena Sophia Kozachuk, Ms. Lu Yao, Mr. Xuchun Wang in Prof. Sham's group as well as Dr. Ruying Li, Dr. Xulei Sui, Dr Hossein Yadegari, Dr. Xia Li, Dr. Xiaofei Yang, Dr. Weihan Li, Mr. Jiwei Wang, Mr. Changhong Wang, Ms. Xiaoting Lin, Mr. Jianneng Liang, Mr. Junjie Li, Ms. Xuejie Gao, Ms. Minsi Li, Mr. Keegan Adair, Mr. Fanpeng Kong, and Mr. Yipeng Sun in Prof. Sun's group. I really appreciate their valuable suggestions and constructive feedback.

I would also like to especially thank Prof. Clara Wren, Prof. James Noël, Prof. François Lagugné-Labarthet, and Dr. Jiju Joseph for their generous help and suggestions.

I also want to thank the technical supports from Dr. Ning Chen, Dr. Qunfeng Xiao, and Dr. Yongfeng Hu at the Canadian Light Source and Dr. Richard Gardiner from Biotron at the University of Western Ontario (UWO).

Last but not least, I thank my family and friends who supported me throughout the graduate program. I am especially grateful to my family for educating and preparing me for my future and providing all the means to fulfill my dreams.

Table of Contents

Abstract ii

Summary for Lay Audience iii

Acknowledgments v

Table of Contents vi

List of Tables ix

List of Figures x

List of Abbreviations xiv

Chapter 1 1

1 Introduction 1

1.1 Fuel Cell Basics 1

1.1.1 Classification of Fuel Cells 1

1.1.2 Fuel Types 3

1.2 Proton Exchange Membrane (PEM) Fuel Cell 4

1.2.1 Cell Components 4

1.2.2 Thermodynamics and Electrochemical Kinetics 5

1.3 Direct formic acid fuel cells 6

1.4 PEMFC Cathode Catalysts 7

1.4.1 Pure Pt Catalyst 7

1.4.2 Pt Alloy Catalysts 7

1.4.3 Shape-Controlled Pt Alloy Catalyst 10

1.5 Reaction Mechanism of the ORR 10

1.5.1 ORR Basics and reaction pathways 10

1.5.2 Electrochemical characterization and ORR activity measurements 11

1.6 Synchrotron Radiation Overview 14

1.6.1 The Generation of Synchrotron Radiation 14
1.6.2 The Advantages of Synchrotron 15
1.6.3 X-ray Absorption Fine Structure 15
1.7 Thesis Outline 20
1.8 References 22
Chapter 2 29
2 Morphology and Catalytic Performance of Pd Nanocubes 29
2.1 Introduction 29
2.2 Experimental Section 30
2.2.1 Material Synthesis 30
2.2.2 Characterization 30
2.3 Results and Discussion 31
2.3.1 Calcination 32
2.3.2 UV-Ozone Irradiation 34
2.3.3 Acid Washing 35
2.4 Conclusions 43
2.5 References 44
Chapter 3 48
3 Controlled growth of palladium nanoparticles and the origin of enhanced electrocatalytic activity with metal-support interactions 48
3.1 Introduction 48
3.2 Experimental Section 49
3.2.1 Material Synthesis 49
3.2.2 Characterization 49
3.2.3 Electrochemical Test 49
3.3 Results and Discussion 50

3.4 Conclusions 62

3.5 References 63

Chapter 4 66

4 Co-doped Pd@Pt core-shell nanoparticles: correlation between the electronic structure and the catalytic activity of the catalysts in ORR 66

4.1 Introduction 66

4.2 Experimental Section 67

4.2.1 Methodology 67

4.2.2 Material Synthesis 67

4.3 Results and Discussion 68

4.4 Conclusions 82

4.5 References 83

Chapter 5 87

5 Summary and Future Work 87

5.1 Conclusions 87

5.2 Future Work 88

5.3 References 90

Curriculum Vitae 91

List of Tables

Table 2-1 Comparison of the electrocatalytic properties of treated Pd/C samples for formic acid oxidation (FAO). 36

Table 2-2 Ratio of D-band and G-band peaks intensity, obtained from Raman spectra, after surfactant cleaning. 43

Table 3-1 Comparison of the catalytic activities for formic acid oxidation, stability, Impedance components and nanoparticle size and composition of Pd NPs on different carbon supports. 61

Table 3-2 X-ray photoelectron spectroscopy (XPS) peak positions of Pd on different carbon supports. 62

Table 4-1 Summary of XRD results regarding (111) facet. 75

Table 4-2 Electrochemical performance of cobalt doped Pd@Pt nanoparticles compared to Pd@Pt and commercial Pt/C. 77

List of Figures

Figure 1-1 A schematic of PEM fuel cell. 4

Figure 1-2 Volcanic type dependence of oxygen reduction activity to the binding energy of oxygen to the metal surface [50]. 7

Figure 1-3. Volcanic type activity (A = kBTln(r), where r is the rate per surface atom per second at a cell potential of 0.9 V) of Pt and Pt alloyed with transition metals [61]. 9

Figure 1-4 Hybridization of Pt d-band with the O_2 σ orbital to form the bonding orbital (d-σ) and anti-bonding orbital (d-σ)* on the Pt surface [62]. 9

Figure 1-5 Oxygen reduction mechanism on noble catalysts [70]. 11

Figure 1-6 Experimental setup for RRDE test: a) Rotator and bipotentiostat, b) RRDE, c) ORR Cell. 13

Figure 1-7 A schematic planar view of Left) synchrotron radiation Right) storage ring [84]..... 15

Figure 1-8 The photoelectric effect, in which an X-ray is absorbed by an atom and a core-level electron is promoted out of the atom, creating a photoelectron and leaving behind a hole in the core electron level [88]. 16

Figure 1-9 Schematic of an X-ray absorption measurement in transmission mode. 17

Figure 1-10 Typical experimental apparatus for XAS measurements. 19

Figure 2-1 A) SEM and B) TEM images of as-synthesized cubic Pd nanoparticles. C) TEM image of Pd nanocubes loaded on carbon black. 31

Figure 2-2 Schematic picture of PVP capped palladium before and after cleaning and the possible reaction pathways of formic acid oxidation on Pd/C nanocubes. 32

Figure 2-3 Cyclic voltammograms acquired on various calcinated Pd/C samples in the solution of A) 0.5 M H_2SO_4 at the scan rate of 50 mVs^{-1} B) 0.5 M HCOOH + 0.5 M H_2SO_4 at the scan

rate of 10 mVs^{-1}. C) Chronoamperometric curves for the oxidation of 0.5 M HCOOH in 0.5 M H_2SO_4 solution at the constant potential of 0.4 V_{RHE}. 33

Figure 2-4 Cyclic voltammograms acquired on various UV-treated Pd/C samples in the solution of A) 0.5 M H_2SO_4 at the scan rate of 50 mVs-1 B) 0.5 M HCOOH + 0.5 M H_2SO_4 at the scan rate of 10 mVs^{-1}. C) Chronoamperometric curves for the oxidation of 0.5 M HCOOH in 0.5 M H_2SO_4 solution at the constant potential of 0.4 V_{RHE}. 35

Figure 2-5 Cyclic voltammograms acquired on acid-treated Pd/C sample in the solution of A) 0.5 M H_2SO_4 at the scan rate of 50 mVs^{-1} B) 0.5 M HCOOH + 0.5 M H_2SO_4 at the scan rate of 10 mVs^{-1}. C) Chronoamperometric curves for the oxidation of 0.5 M HCOOH in 0.5 M H_2SO_4 solution at the constant potential of 0.4 V_{RHE}. 36

Figure 2-6 Relation of peak current density of treated samples with the square root of scan rates in 0.5 M H_2SO_4 solution containing 0.5 M HCOOH. The solid lines are based on a linear least-square fit of the data. 37

Figure 2-7 X-ray diffraction patterns of palladium catalysts before and after removal of surfactant with various treatment methods. 39

Figure 2-8 (A-C) Pd L_3-edge TEY-XANES spectra of carbon supported palladium catalysts after cleaning treatments, compared to untreated sample and Pd foil. D) Scheme proposed for the Pd nanoparticle interaction with PVP. 40

Figure 2-9 Raman spectra of Pd/C nanocubes before and after cleaning treatments. 42

Figure 3-1 TEM images of Pd nanocubes on A) Carbon black (Vulcan XC-72B) Graphene C) CNT D) NCNT supports. 50

Figure 3-2 X-ray diffraction patterns of palladium catalysts grown on different carbon supports. 51

Figure 3-3 A) Nitrogen adsorption (closed symbol) and desorption (open symbol) isotherms and B) multi-point BET plots of the investigated carbon supports. 52

Figure 3-4 Raman spectra of carbon Nanotube before and after doping with nitrogen. 53

Figure 3-5 CV of supported Pd nanocubes electrode in A) 0.5 M H_2SO_4 and B) 0.5 M H_2SO_4 + 0.5 M HCOOH solution. 54

Figure 3-6 Relation of FAO peak current density of different samples with the square root of scan rates. 55

Figure 3-7 Nyquist plots of supported Pd catalysts at 0.2 V (vs. RHE) in 0.5 M H_2SO_4 + 0.5 M HCOOH solution. The inset is showing the equivalent circuit used to fit the impedance spectra. 57

Figure 3-8 Chronoamperometric curves of Pd nanocubes, supported with different carbon materials, at 0.4 V. 58

Figure 3-9 XPS spectra of A) the Pd 3d region of the Pd nanocubes on different carbon supports and B) the N 1s region of NCNT before and after the catalyst growth. 59

Figure 3-10 X-ray absorption near-edge spectra of Pd samples grown on different carbon supports. 60

Figure 3-11 Schematic of the proposed interaction of Pd nanocubes with nitrogen sites in NCNT. 61

Figure 4-1 SEM images of A) Pd nanocubes and B) octahedrons that were used as seed for Pd@Pt core-shell synthesis. 69

Figure 4-2 Snapshot of the whole particle, showing the schematic illustration of the synthesis procedure of Pd@Pt-Co nanoparticles which can be divided to three main steps. 69

Figure 4-3 (A-D) HAADF STEM image and EDX composition maps of Octahedral-shaped Pd@Pt nanoparticle. E) Elemental line-scanning profiles along the direction marked by a white line in “A”. 70

Figure 4-4 (A, B) Bright-field TEM image of octahedral Pd@Pt-Co core-shell nanocrystal C) The typical low-resolution STEM image of the octahedral cobalt doped Pd-Pt nanocrystals D)

HAADF-STEM image of a single Pd@Pt-Co nanoparticle E) STEM-EDX elemental mapping images of Pd, Pt and Co and the merged image F) Elemental line-scanning profiles along the direction marked by a white line in “D”. 71

Figure 4-5 HR-TEM image of the octahedral Pd@Pt core-shell nanoparticles before (A, C) and after (B, D) doping with cobalt. 72

Figure 4-6 (A, C) HR-TEM image of the front and top view of the Pd@Pt octahedra nanocrystal. (B, D) The typical low-resolution STEM image of the Pd-Pt nanocrystals and their particle size distribution histogram. 73

Figure 4-7 XRD spectra of Pd@Pt/C and Pd@Pt-Co/C octahedra. 74

Figure 4-8 A) CVs and B) ORR polarization curves for the Pd@Pt/C and cobalt doped Pd@Pt/C catalysts. The current densities (j) were normalized against the geometric area of RDE (0.196 cm^2). C) Mass and D) Specific activities given as kinetic current densities (j_k) normalized against the mass of Pt and the ECSA of the catalyst, respectively. (Inset is showing the specific activity of the two catalysts at 0.9 V_{RHE}.). (E, F) linear sweep voltammetry of Pd@Pt-Co (E) and Pd@Pt (F) catalysts before and after 20,000 cycles between 0.6−1.0 V_{RHE} in O_2 saturated 0.1 M $HClO_4$ electrolyte. (Insets are showing the mass activity (at 0.9 V_{RHE}) of the catalysts before and after the accelerated durability tests. 75

Figure 4-9 (A, C) LSV curves at different rotation rates recorded for ORR at Pd@Pt/C (A) and Pd@Pt-Co/C (C) catalysts in oxygen-saturated 0.1 M HClO4. Scan rate: 10 mV s^{-1}. Rotation rate: 400, 600, 900, 1600. (B, D) Koutecky-Levich plots of Pd@Pt and Pd@Pt-Co catalysts at different electrode potentials..... 78

Figure 4-10 Cyclic voltammetry (CVs) of methanol oxidation for Pd@Pt/C and Pd@Pt-Co/C catalysts in 0.1 M $HClO_4$ and 1 M CH_3OH solution at 25 °C with a sweep rate of 10 mV s^{-1}.... 79

Figure 4-11 X-ray absorption studies of the Pd@Pt and cobalt doped Pd@Pt catalysts in comparison with Pt foil. A) The normalized XANES spectra at Pt L_3 edge and B) The K3-weighted Fourier transform spectra from EXAFS. Inset in (A) shows the enlarged spectra at Pt L_3 edge. 81

List of Abbreviations

AFS	Alkaline fuel cells
ALS	Advanced light source
CLS	Canadian light source
CV	Cyclic voltammetry
CVD	Chemical vapor deposition
DFT	Density functional theory
DI	De-ionized
EDX	Energy dispersive X-ray
EELS	Electron energy loss spectroscopy
EXAFS	Extended X-ray absorption fine structure
f.c.c	Face centered close-packed
FY	Fluorescence yield
HRTEM	High resolution transmission electron microscopy
HXMA	Hard X-ray MicroAnalysis
LINAC	Linear accelerator
LSV	Linear sweep voltammetry
MCFC	Molten carbonate fuel cells
NC	Nanocube
NCNT	Nitrogen-doped carbon nanotube
NP	Nanoparticle
NT	Nanotube

ORR	Oxygen reduction reaction
PAFC	Phosphoric acid fuel cells
PEM	Proton exchange membrane
PGM	Platinum group metal
RDE	Rotating disc electrode
ROI	Region of interest
RHE	Reversible hydrogen electrode
SEM	Scanning electron microscopy
SR	Synchrotron radiation
SOFC	Solid oxide fuel cells
SXRMB	Soft X-Ray microcharacterization beamline
TEM	Transmission electron microscopy
TEY	Total electron yield
UPD	Underpotential deposition
UV	Ultraviolet
WL	Whiteline
XAFS	X-ray absorption fine structure
XANES	X-ray absorption near edge structure
XAS	X-ray absorption spectroscopy
XPS	X-ray photoelectron spectroscopy
XRD	X-ray diffraction

Chapter 1

1 Introduction

1.1 Fuel Cell Basics

Fuel cell is an electrochemical cell that can produce energy through chemical reactions of supplied fuels and oxidants [1-3]. Fuel cell, which is first introduced by William Grove in 19th century, has various privileges over other common sources of energy [4]. Among all the fruitful characteristics of this renewable source of energy, having no specific pollution and producing water as the only waste have attracted lots of attentions [5]. Although the base of fuel cell is the same as battery, which is obtaining energy from the chemical energy of fuels, there will be no necessity for recharging in fuel cells and it will be working until the supplied fuel is used up [6]. In a world that all people are suffering from air pollutions and global warming, which are mainly occurring due to the high usage of fossil fuels, fuel cells with their environmentally-friendly structure and efficient energy conversion are known as the most promising substitute [7].

1.1.1 Classification of Fuel Cells

Fuel cells are usually categorized based on the fuel, electrolyte, and temperature that they are utilizing [8-10]. Polymer electrolyte membrane fuel cells (PEM fuel cells or PEMFCs), alkaline fuel cells (AFCs), phosphoric acid fuel cells (PAFCs), molten carbonate fuel cells (MCFCs) and solid oxide fuel cells (SOFCs) can be mentioned as the most common known fuel cells.

1.1.1.1 Proton Exchange Membrane Fuel Cells (PEMFC)

Polymer exchange membrane fuel cells consist of an ion exchange membrane which is isolating the anode and cathode electrodes [2, 11, 12]. As water will be the only solution in this cell, corrosion and electrolyte management problems will be in the lowest level possible and this can assist to their commercialization [13]. Although the highest working temperature in this cell will be around 80°C, due to the aqueous solution, these cells are having the highest power density and can alter their output to as high as 250 kW [14]. Apart from their prodigious features, these cells are really sensitive to the impurities in the supplied fuel, and the employed catalysts in these cells can be easily poisoned [15]. In addition, the water level in the cell should be always monitored to

make sure evaporation is not happening more rapidly than the water production and the membrane is always being hydrated.

1.1.1.2 Alkaline Fuel Cells (AFC)

Alkaline fuel cells which are using alkaline electrolyte such as sodium hydroxide or potassium hydroxide, were first commercially employed by NASA in Apollo missions. Substitution of acid with alkaline have given numbers of advantageous to AFC compared to the other common fuel cells [16]. Due to the usage of alkaline electrolyte and higher boiling point of them, the temperature can be enhanced and this can promote AFC to the highest energy efficiency cell. In addition, oxygen reduction reaction with its sluggish kinetic will be more favorable in alkaline electrolyte compared to the acidic solutions [17]. Using wide variety of catalysts including noble and non-noble catalysts, have made them to be the desirable cell for most applications. However, the main obstacle in their commercialization process is their electrolyte sensitivity to CO_2 [18]. CO_2 can react with the alkaline electrolyte and the by-product of this reaction can clog the electrolyte pathways and hinder the desired features.

1.1.1.3 Phosphoric Acid Fuel Cells (PAFC)

Unless the low temperature fuel cells, which are sensitive to CO poisoning, high temperature in phosphoric acid fuel cell has given the benefit of carbon monoxide and impurity tolerance in the working conditions [19, 20]. Due to the employed electrolyte and its thermal and chemical stability, PAFC can be used at the temperature of 150-200 °C. In addition, concentrated acid has minimized the water vapor in the system and this has reduced the concerns regarding water management [21]. All these features have made PAFC the first commercialized fuel cell until now.

1.1.1.4 Molten Carbonate Fuel Cells (MCFC)

Molten carbonate fuel cells were first developed in 20^{th} century and are known for their high working temperature. Having high temperature can be advantageous in several aspects and can make MCFC a promising candidate for stationary power generation, with the possibility of using waste heat in other processes [22, 23]. High temperature is also fruitful in the employed catalyst and the high ORR kinetic in elevated temperatures will eliminate the necessity for noble materials as catalyst [24]. These cells will usually utilize alkali metal carbonate electrolyte, such as molten

lithium, sodium or potassium carbonates kept in a ceramic matrix. Due to the limited conductivity of molten carbonate electrolyte, enhanced temperature will be needed to promote carbonate ion for higher ion conductivity [25]. Although the elevated temperature can eventuate in cheaper catalysts and higher efficiency, it can be also detrimental to the cell in terms of corrosion and oxidation of cell components.

1.1.1.5 Solid Oxide Fuel Cells (SOFC)

Another promising candidate for the industrial applications is solid oxide fuel cell which is employing solid oxide materials, mainly ceramics, as electrolyte [26, 27]. This solid electrolyte has given the chance of enhancing temperature to as high as approximately 1000 °C, in which oxygen ions will provide the required ion conductivity. Similar to the other high temperature cells, SOFC operation will not entail noble metal catalysts and the high kinetic of ORR in these cells have reduced the final price due to the usage of non-noble electrocatalysts. Still, corrosion and chemical instability at elevated temperatures are the main hindrances to the commercialization process [28, 29].

1.1.2 Fuel Types

Fuel cells are usually categorized by the type of fuels they are using. The most prevalent fuel is pure H_2 now, which is mainly used in PEM fuel cells and its combination with oxygen can produce electricity and water, as the only waste. Although pure H_2 can lead to the highest power density and efficiency, several difficulties regarding their storage and compression have limited its application [30, 31]. There can be also another possible pathway for supplying hydrogen to the cell by reforming methanol, ethanol or natural gas, but the CO produced in the reforming process as by-product can poison and deactivate the catalysts and alter the cell efficiency.

To overcome this challenge, formic acid, methanol, or ethanol can be directly supplied to the cell for direct oxidation [32]. In this way, the mentioned obstacles related to pure H_2 can be avoided and high open circuit potential and finite fuel crossover can be obtained [33, 34]. However, these fuels have their own operational impediments and their low oxidation kinetic on anode side and high oxidation on cathode side, which will lead to mixed potential, have limited their industrial applications [35].

1.2 Proton Exchange Membrane (PEM) Fuel Cell

Among all these types of fuel cells, PEMFCs which have high power density, high energy conversion efficiency, low-temperature operation and, the ability for portable power applications have attracted more attention [36]. Since this research concerns with catalysts for PEM Fuel Cells, it will be described in some details below.

1.2.1 Cell Components

A schematic of a typical PEMFC is shown in Figure 1-1, in which anode and cathode are separated by Nafion®, which is acting as the polymer electrolyte and is ion conductive and are electronically connected with an external circuit [37, 38]. The two electrodes will be supported with bipolar plates, which will be responsible for supplying fuels and oxidants to the electrodes. All these components will be hot-pressed to obtain Membrane Electrode Assembly, a sandwich structure which is the main part of fuel cell [39].

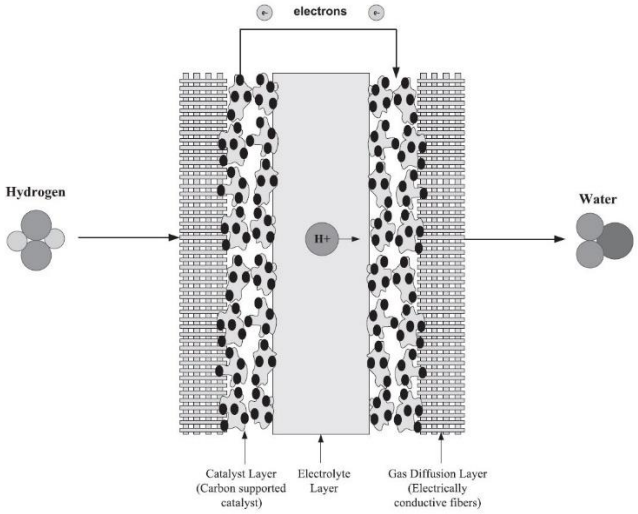

Figure 1-1 A schematic of PEM fuel cell.

As it is shown in the schematic, hydrogen will be supplied to the anode and will be decomposed to protons and electrons. The generated protons will travel along the PEM and the negatively charged electrons will pass through an external circuit to get to the cathode side. At the cathode side, these protons and electrons will react with the oxygen, that is being supplied from air, and will produce water.

With having a look at the whole process of PEM fuel cell, water, heat and electricity current are the only results of the electrochemical reactions and there will be no specific pollution. The reactions in which energy is being produced by H_2 and O_2 are as follows [2]:

Anode: $$H_2(g) \rightarrow 2H^+(aq) + 2e^- \quad (1)$$

Cathode: $$\frac{1}{2}O_2(g) + 2H^+(aq) + 2e^- \rightarrow H_2O(l) \quad (2)$$

Overall: $$H_2(g) + \frac{1}{2}O_2(g) \rightarrow H_2O(l) + electricity\ energy + heat \quad (3)$$

1.2.2 Thermodynamics and Electrochemical Kinetics

Electrical energy is the outcome of chemical reactions in fuel cells. With the operation of chemical reactions in fuel cells, a maximum electrical work of W_e can be obtained. Using the following equation, electrical work of fuel cells, at a constant temperature and pressure, can be acquired [40].

$$W_e = \Delta G = -nFE \quad (4)$$

n, *F*, and *E* are number of electrons involved in the reaction, Faraday's constant, and the cell potential respectively.

Using the enthalpy and entropy change, Gibbs free energy change which is required in electrical work calculation, can be obtained. The formula is mentioned as follows:

$$\Delta G = \Delta H - T\Delta S \quad (5)$$

In a general cell reaction, like the one in Equation 6, the Gibbs free energy change can be calculated for the reaction using the following equation.

$$\alpha A + \beta B = \nu C + \delta D \quad (6)$$

$$\Delta G = \Delta G_0 + RT\ ln\frac{[C]^\nu[D]^\delta}{[A]^\alpha[B]^\beta} \quad (7)$$

ΔG_0 and *[X] (X: A, B, C and D)* are the Gibbs free energy change at standard temperature and pressure and concentration of species, respectively.

By substituting Equations 4 and 7, the Nernst's equation will be obtained [41]. This equation can be employed to calculate the ideal cell voltage of a fuel cell. If we consider the overall reaction of PEM fuel cell like the one in Equation 9, the cell voltage can be calculated using the Nernst's equation as shown in Equation 10.

$$E = E_0 - \frac{RT}{nF} ln \frac{[C]^{\nu}[D]^{\delta}}{[A]^{\alpha}[B]^{\beta}} \quad (8)$$

$$H_2(g) + \frac{1}{2} O_2(g) \rightarrow H_2O(l) \quad (9)$$

$$E = E_0 + \frac{RT}{nF} ln\left(P_{H_2} P_{O_2}^{0.5}\right) \quad (10)$$

By following these calculations, it is obvious that the reaction of H_2 and O_2 is occurring in the ideal cell voltage of 1.23 V and this voltage can be reduced to 1.18 V if the product alters from liquid water to gaseous water.

1.3 Direct formic acid fuel cells

Obstacles in the commercialization of PEM fuel cells, because of the high cost and risk of storing hydrogen, and DMFCs, because of the high fuel crossover rate, have increased interest for specific types of PEMFCs called direct formic acid fuel cells [42, 43]. In these fuel cells, formic acid will not be reformed and will be fed directly to the anode. Due to their unique specifications such as high energy density and open circuit potential, utilization of non-flammable and non-toxic fuel, and higher energy conversion efficiency, they are substituting the current common cells for portable applications [44]. The cathode, anode and overall reactions occurring in a direct formic acid fuel cell are mentioned as follows:

Anode: $HCOOH \rightarrow CO_2 + 2H^+ + 2e^-$ $E^0 \sim -0.25\, V_{RHE}$ (11)

Cathode: $\frac{1}{2} O_2 + 2H^+ + 2e^- \rightarrow H_2O$ $E^0 \sim 1.23\, V_{RHE}$ (12)

Overall: $HCOOH + \frac{1}{2} O_2 \rightarrow CO_2 + H_2O$ $E^0 \sim 1.48\, V_{RHE}$ (13)

1.4 PEMFC Cathode Catalysts

1.4.1 Pure Pt Catalyst

Although the tremendous role of platinum in oxygen reduction reaction rate is not deniable, still there is a big gap between platinum activity for ORR and the desired activity for commercialization [45, 46]. Other than the direct four-electron reduction, there are other parallel reactions occurring on the Pt surface which is leading to lower activity in the oxygen reduction reaction [47]. An ideal catalyst should have sufficient active sites on its surface and should be able to allow oxygen species to adsorb strongly enough on its surface [48]. On the other hand, the binding between catalyst and oxygen species should be weak enough to let the products (OH*) desorb from surface and provide free surface for further reactions. Having a weak interaction will cease the high reaction rate and the strong interaction will block the available surface for new reactants. This principle will bring us to the volcano plot which is comparing the ORR activity with adsorption energy [49]. As shown in Figure 1-2, platinum has the highest activity compared to the other bulk metals.

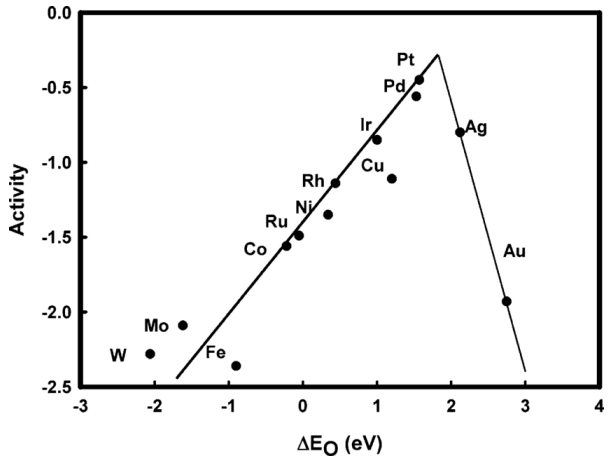

Figure 1-2 Volcanic type dependence of oxygen reduction activity to the binding energy of oxygen to the metal surface [50].

1.4.2 Pt Alloy Catalysts

Although platinum is known as the best catalyst for Anode and Cathode reactions, PEM fuel cell commercialization is still in need of catalysts with higher activity [51-53]. Platinum can be used to split hydrogen molecule easily on the anode side but splitting of stronger oxygen molecule on

the cathode side is still a matter of concern [54]. Therefore, to overcome the sluggish kinetics of ORR and to enhance the performance of PEM fuel cell, we need to have more active and stable electrocatalysts. The kinetics of ORR on platinum-based catalysts is highly dependent on the dissociation energy of the O-O bond and the OH bonding energy on the platinum surface. Theoretical and experimental results have confirmed that Pt d-band vacancy (electronic structure) and Pt-Pt bonding length (geometric effect) can have a tremendous effect on these energies, so the most influential path toward further enhancing the electrocatalytic activity of platinum will be modifying its electronic and geometric structure. It is known that making a compressed strain in the platinum structure can lower its d-band center. This effect can lead to the formation of occupied antibonding orbitals and the outcome will be a surface which will bind to oxygen-containing intermediates weaker compared to the unaffected Pt. Having more available surface can be also advantageous for continuing the reaction and increasing its activity. Electronic interactions such as charge transfer can be also effective in determining the reaction activity. It is proved that platinum with lower d band vacancies can lower the Pt-O bond strength. This can make platinum surface be less covered by oxygen-containing intermediates and can provide more available active sites on its surface. Having all these features together have made us to utilize platinum alloys which can be effective in altering both geometric and electronic structure of Pt. Considering Pt-M alloys, it is proven that M (transition metals) not only can alter the electronic structure of platinum by their electron transfer with platinum but also can cause lattice contraction in Pt [55]. Therefore, Pt-based alloys can generate more desirable Pt-Pt distance for the dissociative adsorption of O_2 and can weaken the O-O bonds [56]. This phenomenon is occurring due to the transfer of transition metal d-electrons to unfilled d-orbital of platinum which can lead to a higher number of d-band occupancy in Pt [57]. Based on the electronegativity of the utilized base elements, distinct influence will be observed on the electronic structure of platinum.

The correlation between ORR activity and the d-band center is shown in Figure 1-3. As it can be seen in Figure 1-3, which is famous as volcano-type behavior of Pt, two opposing features can influence Pt activity simultaneously [49]. For an optimum activity, Pt should have high absorption energy for O_2 or oxygen intermediate species and its surface should have low coverage by oxygen species. Considering the densities of states of platinum diagram, the volcano-type behavior of Pt can be easily explained [51]. As it is shown in Figure 1-4, although the downward shift of d-band center can generate more d-band vacancies, the band center should be optimized for the highest

expected activity [58]. Based on Sabatier's principle when d-band center is too close to the Fermi level, ORR will be constrained by the anion-free Pt sites because Pt will bond to oxygen, oxides or anions strongly [59]. On the other hand, when d-band center is too far from the Fermi level, the low absorption energy of O_2 on platinum will limit the required ORR rate by the restriction in electron and proton transfer [60].

Considering all these issues and the need for the utilization of low abundant and expensive platinum, researches have been focused on Pt alloy, which can have the following advantages over pure Pt:

a. Enhancement of electrochemical utilization of catalyst.
b. Fine-tuning the surface chemistry and electronic properties of Pt.
c. Reducing the final price of the obtained catalyst

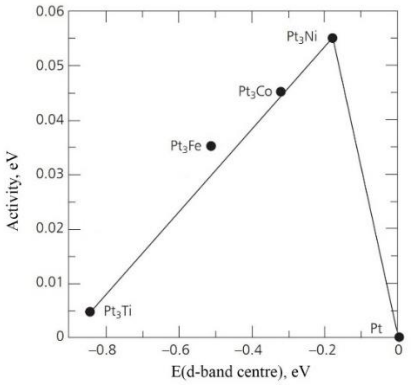

Figure 1-3. Volcanic type activity (A = kBTln(r), where r is the rate per surface atom per second at a cell potential of 0.9 V) of Pt and Pt alloyed with transition metals [61].

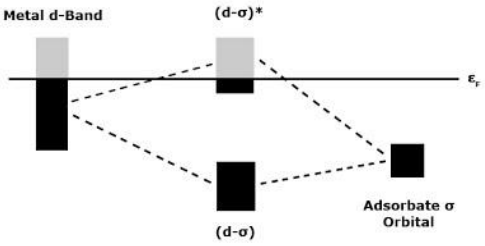

Figure 1-4 Hybridization of Pt d-band with the O_2 σ orbital to form the bonding orbital (d-σ) and anti-bonding orbital (d-σ)* on the Pt surface [62].

1.4.3 Shape-Controlled Pt Alloy Catalyst

Limited ORR activity of platinum has compelled us to modify its electronic structure through various methods such as facet-controlled synthesis which can alter the adsorption behavior of oxygen species and reaction intermediates [63, 64]. The activity dependence of ORR on diverse crystal facets of platinum have been investigated in recent years and its advancement with other techniques such as alloying has made a turning point in enhancing the overall performance of Pt catalysts [65].

In order to acquire a shape-controlled nanoparticle, colloidal chemistry will be utilized. In colloidal chemistry, organic agents and stabilizers will be employed and their selective adsorption on specific surfaces of Pt will lead to a nanoparticle with controlled morphology [66]. Organic compounds can be also fruitful for the aggregation prevention. These surfactants will usually adsorb on the platinum surface with their carbon chains and their hydrophobic feature will hinder the aggregation.

1.5 Reaction Mechanism of the ORR

1.5.1 ORR Basics and reaction pathways

Oxygen reduction reaction which is important in various fields of research including biology and energy conversion, is the main reaction occurring in fuel cells. Oxygen reduction reaction (ORR) which is occurring on the cathode side, is the main obstacle in the commercialization process of PEM fuel cell [67]. Although the utilization of platinum as catalyst has enhanced the ORR activity compared to the other utilized bulk metals, slow kinetics of ORR is still recognized as the principal reason for high overpotential and low energy conversion efficiency of PEM fuel cells.

ORR entails several individual reactions and intermediates which are shown in Figure 1-5 [68]. Although the production of water through a 4-electron pathway is the desired reaction, hydrogen peroxide may be produced through a two-electron pathway too [69]. This incomplete reduction of oxygen to hydrogen peroxide can lower the energy conversion efficiency and can poison the catalyst by the harmful free radical species.

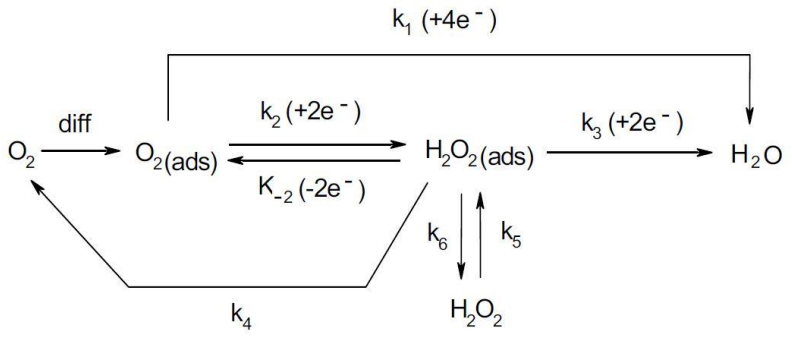

Figure 1-5 Oxygen reduction mechanism on noble catalysts [70].

1.5.2 Electrochemical characterization and ORR activity measurements

1.5.2.1 Cyclic Voltammetry

Scanning potential between two specific points and recording the passing current between working and counter electrode, is known as cyclic voltammetry [55]. The observed current can be categorized to anodic and cathodic, in which anodic (cathodic) current will increase when potential sweeps to higher(lower) numbers. The position of anodic and cathodic currents can be also used to find out the reversibility or irreversibility of reactions. Scanning potential just in one direction is useful when there is no special information in the reverse reaction and is called linear sweep voltammetry. The main aim for conducting cyclic voltammetry is obtaining electrochemical active surface area (ECSA). ECSA is showing the catalyst surface area which is participating in reactions. Using integrate charge of hydrogen absorption/desorption peak area from CV or oxidative stripping of carbon monoxide, can provide mass-specific surface area. In this study, potential was cycled between 0.05 and 1.10 V with the sweep rate of 0.05 V/s in N_2 purged 0.1 M $HClO_4$ solution. All the calculations were done by using the CV after 50 cycles, to clean the working electrode and obtain a stable CV curve. Following equation is used for obtaining ECSA in which L_{Pt} is the working electrode Pt loading (mg_{Pt} cm^{-2}) and A_g (cm^2) is the geometric surface area of the glassy carbon electrode (0.196 cm^2).

$$ECSA_{Pt}(m^2 g_{Pt}^{-1}) = \left[\frac{Q_{H-adsorption(C)}}{210\ \mu C\ cm_{pt}^{-2} L_{pt}(mg_{pt} cm^{-2}) A_g(cm^2)}\right] 10^5 \qquad (14)$$

1.5.2.2 Rotating (Ring) Disk electrode

As it is mentioned before, one of the main steps in an in-process reaction is the transportation of reactants to and from the catalyst [71]. This transportation and the resultant reaction is proceeding through diffusion or convection, which diffusion always dominant [72, 73]. Rotating electrodes in some experiments can be used to make the convection, the dominant path for mass transport. In the rotating electrode, reactant will be dragged, and the product will be spun away from the surface and this can provide more reactant to the catalyst. Although there will be both convection and diffusion mass transport, there is still a stagnant layer on the surface of electrode which its thickness is dependent to the rotation rate of electrode.

In some particular experiments, where we want to find out the product forming on the surface of electrode, Rotating Ring Disk Electrode will be beneficial. RRDE has the exact same structure as RDE but with an extra ring for probing the product forming on electrode. With having a constant potential for the ring, the product of oxidation (reduction) can be reduced (oxidized). By changing potential and observing the resultant current, different products with comparative quantities can be determined [74]. As it was mentioned before, ORR can be proceeded through different mechanism. To find out the mechanism and the products formed during the ORR, RRDE can be employed. RRDE can quantify the amount of produced H_2O_2 by evaluating the total number participated electrons and can distinguish the catalyst with peroxide generating tendency.

1.5.2.3 Accelerated Durability Test

The last step toward commercialization of a catalyst and making it a cost-effective choice for utilization in fuel cell is finding out its stability through accelerated durability test (ADT). An appropriate catalyst for an industrial usage should be able to tolerate a specific amount of operating time and this can be studied by ADT. Sweeping the potential under desired conditions and recording the resultant current before and after a specific amount of cycles can show the stability of catalysts in a particular time. In this study, ADT was conducted by applying CV in the potentials between 0.6-1.0 V with a scan rate of 0.1 V/s in O_2 purged solution. In this potential range, oxidation and reduction of platinum will occur and will cause dissolution of Pt as Pt^{2+}.

1.5.2.4 Electrochemical Impedance Spectroscopy

EIS is basically used to track the electrical properties of materials and their interface with electrolyte. It can be also used to ascertain the double layer capacitance of the interface [75]. All this information can give a good perspective about kinetic, mass and charge transfer resistance and that is why it is highly utilized in optimization of MEA, which is simulating the real working condition of fuel cell setup. Charge transfer resistant, which can be related to the resistant between the electrode and adsorbed species, will be reduced in ORR due to an increase in oxygen concentration. This Kinetic parameter can be obtained using EIS and can be utilized to find out exchange current density of ORR on different samples [76]. Exchange current density can be calculated using the following equation:

$$R_{ct} = -\frac{\eta}{i} = \frac{RT}{nFi_o} \qquad (15)$$

An overall picture of the whole electrochemical station is shown in Figure 1-6.

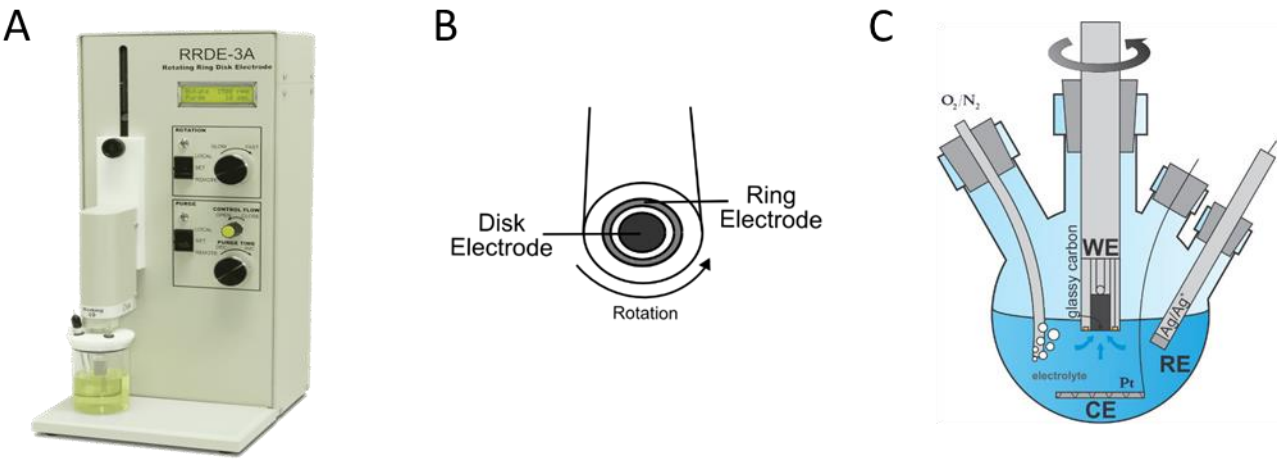

Figure 1-6 Experimental setup for RRDE test: a) Rotator and bipotentiostat, b) RRDE, c) ORR Cell.

1.6 Synchrotron Radiation Overview

As described above, ORR activity of Pt-based alloys is highly dependent to their electronic and geometric structure. In order to characterize the synthesized catalysts and compare their metallic d states occupancy and bonding distance, Synchrotron radiation is used in this work. The features and advantages of this powerful technique is explained below.

1.6.1 The Generation of Synchrotron Radiation

Synchrotron is an accelerator that generates electromagnetic radiation which will be emitted when electrons, at relativistic speed, are forced to alter their direction of motion under the influence of a magnetic field [77-79]. In synchrotron facilities, electrons are accelerated then directed to a storage ring and are driven by the magnetic field of bending magnets or other utilized supplies such as undulator or wigglers [80]. The implemented magnetic field, perpendicular to the electron motion, can generate electromagnetic radiation by bending the electrons [81]. Electrons will enter storage ring when they are accelerated by a linear accelerator or 'linac' to a desired energy, normally millions of electron volts (MeV) and then further accelerated by a booster ring that promotes their energy to billions or Giga electron volts (GeV).

Those electrons which have obtained the specific energy, will pass through a circular path by the force of a magnetic field. By this circulation, electrons will lose part of their energy by emitting synchrotron radiation and they will need to reobtain the missed energy [82]. In this condition, electrons will pass through Radio Frequency (RF) cavities and will regain the lost energy [83]. A schematic of a synchrotron radiation facility is shown in Figure 1-7.

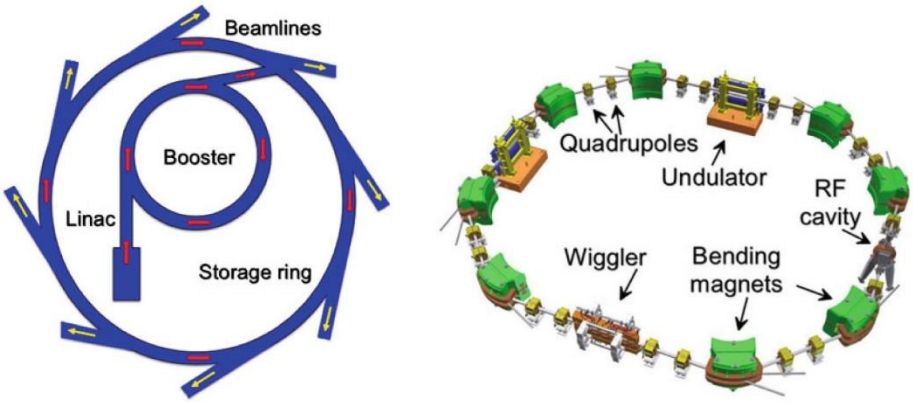

Figure 1-7 A schematic planar view of Left) synchrotron radiation Right) storage ring [84].

1.6.2 The Advantages of Synchrotron

Unique features of Synchrotron radiation have made it a remarkable source for various materials characterizations. The advantageous of SR over laboratory X-ray sources are as follows:

a. Its high photon energy tunability which can cover from IR to as far as hard X-ray.
b. Its high intensity can also be beneficial in fast and statistic measurements.
c. High collimation of SR, which is the result of small beam divergence, can be also helpful in high resolution measurements.
d. The pulsed time structure of SR, with having pulse duration of nanoseconds to picoseconds, can be also utilized in investigation on properties of materials dynamics.
e. High level of polarization and low emittance can be also mentioned as other strength points of SR over other techniques.

These features have made SR a reliable source for X-ray absorption spectroscopy.

1.6.3 X-ray Absorption Fine Structure

One of the advantageous characteristic methods utilizing SR is known as X-ray Absorption Fine-Structure (XAFS). XAFS can provide reliable information regarding chemical and physical properties of an atom and its surrounding which is being investigated [85]. In XAFS, SR will be used to tune the energy at and above a selected core-level binding energy of a specified element. Characterizing the local environment of different kinds of materials such as crystals, amorphous systems, glasses, quasicrystals, disordered films, membranes, solutions, liquids, metalloproteins,

and even molecular gases has further distinguished this element specific method [86]. The principle of XAFS is to find out how x-rays at different energies are being absorbed by the matter across a specific absorption edge, using X-ray absorption coefficient $\mu(E)$ [87].

X-rays with energies ranges from 500 eV-500 keV can be absorbed by all matter through photoelectric effect. In this phenomenon, an electron at core level can absorb X-ray with higher energy compared to its binding energy and may be excited to continuum. So, X-ray will be absorbed, and the excess energy of the binding energy will be ejected as photoelectron according to conservation law ($KE = h\nu - BE$ in gas phase) as shown in Figure 1-8.

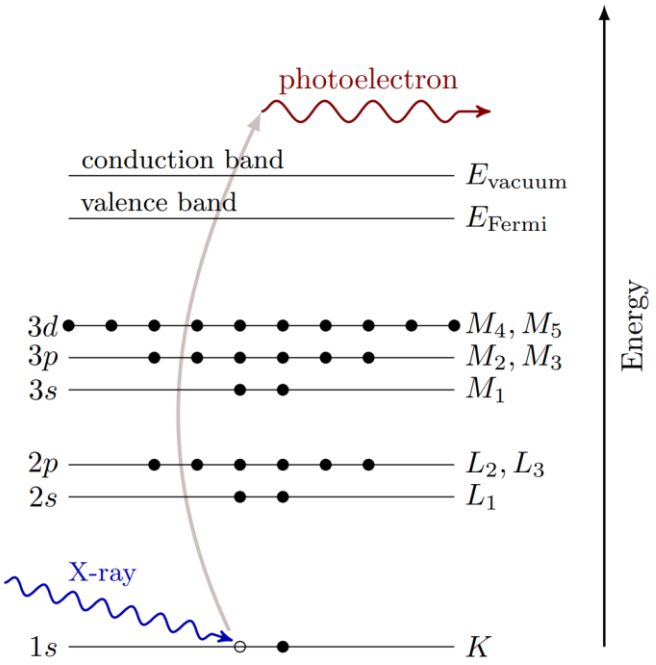

Figure 1-8 The photoelectric effect, in which an X-ray is absorbed by an atom and a core-level electron is promoted out of the atom, creating a photoelectron and leaving behind a hole in the core electron level [88].

The first concern in XAFS is discussing the probability of absorption of X-rays based on Beer's law:

$$I = I_0 e^{-\mu t} \qquad (16)$$

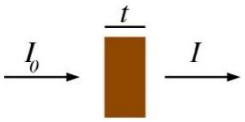

Figure 1-9 Schematic of an X-ray absorption measurement in transmission mode.

In this equation *I*, as shown in Figure 1-9, is the incident X-ray, I_0 is the transmitted x-ray and *t* is the thickness of homogeneous sample. The absorption coefficient, μ, can be obtained using the following equation:

$$\mu \approx \frac{\rho Z^4}{AE^3} \qquad (17)$$

In which *Z* is the atomic number, *A* is atomic mass, ρ is sample density and *E* is the X-ray energy. As it is obvious in Equation 17, absorption coefficient will be highly dependent on *Z* and *E* and that's the main reason for a good contrast between various materials in this technique. When an atom is placed in a chemical environment, the absorption coefficient will be modulated such that it exhibits modulation (oscillations) depending on the nature of the adjacent atoms and bonding. X-ray Absorption Fine Structure (XAFS) spectroscopy is the result of this modulation.

Relaxation of an excited core-hole state, with the absorption of X-ray, can be accomplished through two different mechanisms which are Auger electron and X-ray fluorescence [88]. In X-ray fluorescence, a core-hole will be filled with higher energy electron and an X-ray with specific energy will be released. In contrast, in Auger electron, an electron will be emitted to the continuum after filling the core-hole.

The name XAFS entails two different but closely relating techniques: XANES, EXAFS

Although the main concept of all these two techniques is the same, distinct approximation, terminology or theoretical approach may be used in each of them.

X-ray Absorption Near Edge Structure (XANES) which will be within 30 eV of the main absorption edge, can give information as follows:

Coordination chemistry (e.g., octahedral, tetrahedral coordination), Molecular orbitals, Band structure, and Multiple scattering.

All these interpretations can be obtained mostly semi-quantitatively by considering the shift and intensity of absorption edge, which is arising from the binding energy of the excited electron. Physically, electron excitation follows dipole selection rules and will be excited to the lowest unoccupied state at the threshold. Thus the $L_{3,2}$-edge of transition metals can provide advantageous information about their occupied and unoccupied d states which can be used for catalytic performance interpretation [89, 90].

The shift in absorption edge can be interpreted to find out the corresponding oxidation state. In cations for example, higher oxidation state will result in a positive shift as much as several eV.

Extended X-ray Absorption Fine Structure (EXAFS) is related to the oscillation occurring in the energies above the absorption edge. If the ejected photoelectron gets enough energy to escape the bound state, it may interact with the bound state of other electrons in the vicinity [91]. This interaction with other electrons in the vicinity can produce scattering. The interference of outgoing and backscattering waves in energies ranges 50-1000 eV above absorption edge, can generate some frequency oscillation in the absorption coefficient [92]. EXAFS is composed of these oscillations and can be quantitatively utilized for identifying type, number, and distribution of backscattering atoms [93].

EXAFS will be focused on oscillations above absorption edge and the following equation will be used to define EXAFS function $\chi(E)$ as the fractional modulation in the X-ray absorption modulation:

$$\chi(E) = \frac{\mu(E) - \mu_0(E)}{\Delta\mu_0(E)} \qquad (18)$$

Where $\mu(E)$ is absorption coefficient, $\mu_0(E)$ is absorption coefficient in the absence of EXAFS influence (free atom) and $\Delta\mu_0$ in the measured jump in the absorption $\mu(E)$ at E_0.

It is obvious that EXAFS is usually known as the wave behavior of photoelectrons, so it is common to convert the energy of X-ray to k which is the wavenumber of the photoelectrons. This conversion can be accomplished through the following equation where m is the electron mass, h is Planck's constant and E_0 is the energy of absorption edge:

$$k=\sqrt{\frac{2m(E-E_0)}{h^2}} \quad (19)$$

χ(E), which is usually known as "the EXAFS", is oscillatory and will decay rapidly. So in order to display and emphasize oscillation in different *k* regions, *χ(E)* will be multiplied by a power of *k* (usually k^2 or k^3).

EXAFS can demonstrate various features such as the number of scattering atoms by checking the oscillation amplitude, the absorber-scatter distance which can be determined by oscillation frequency and identity of the scatter atom which can be clarified using oscillation shape [94].

Equation 20 will be also utilized for quantitative analyses of EXAFS in which, *f(k)*, the backscattering amplitude, and *δ(k)*, the phase, are scattering properties of the atoms neighboring the excited atom; *δ(k)*, in fact has both absorbing and backscattering atom contributions; *N* is the number of neighboring atoms, *R* is the distance to the neighboring atom, and σ^2 is the disorder in the neighbor distance.

With *f(k)* and *δ(k)*, the EXAFS equation can be used to determine *N*, *R*, and σ^2.

$$\chi(E)=\sum_j \frac{N_j f_j(k) e^{-2k^2\sigma_j^2}}{kR_j^2} sin\left[2kR_j+\delta_j(k)\right] \quad (20)$$

As it is presented in Figure 1-10, there are two main modes in measuring XAFS, transmission, and fluorescence. Unless the transmission mode which will measure the intensity of X-ray beam before and after its incident with the sample, secondary emission will be measured in fluorescence.

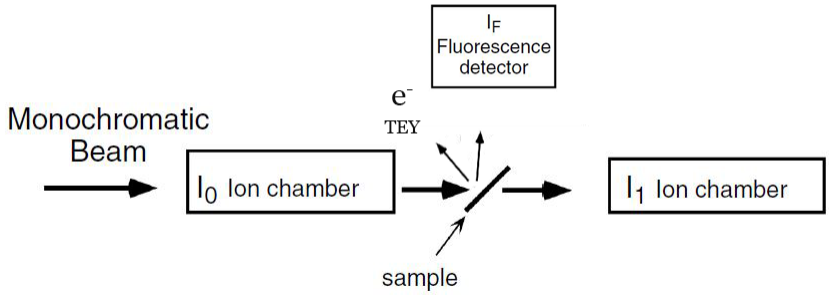

Figure 1-10 Typical experimental apparatus for XAS measurements.

X-ray absorption coefficient will be measured distinctly in each mode and the related equation is mentioned as follows [95]:

Transmission : $\mu(E) = ln\left(\frac{I_o}{I}\right)$ (21)

Fluorescence : $\mu(E) \propto \frac{I_f}{I_o}$ (22)

1.7 Thesis Outline

Climate change and deficiency of petroleum-based energy resources have risen concerns about the future of planet earth and have made scientist to be more focused on fuel cell technologies, due to their low emissions and high efficiencies. Low operation temperature, high power, and energy density have made the PEMFC, a promising candidate for the next generation power sources in transportation, stationary and portable applications. Low abundance, limited supply, and increasing demand have limited the commercial application of Pt, as a critical catalytic component in PEMFC. So finding an efficient catalyst and substituting it with the current commercial ones can accelerate the utilization of this technology and can mitigate the current concerns about the climate change crises. DFAFCs as a subcategory of PEM fuel cells have also attracted lots of attentions in recent years due to their high energy conversion efficiency and non-toxic and safe fuel. The low stability of palladium, as a catalyst for DFAFC has also diminished its commercial applications and catalysts with higher stability will be required.

This study will discuss more fundamentally in 5 chapters for satisfying the mentioned demands.

In chapter 1, anintroduction of platinum-based NPs as a required catalyst for fuel cell is described. Oxygen reduction reaction as a rate determining step in the whole fuel cell reactions is discussed, and X-ray absorption spectroscopy as an efficient way of studying electronic structure, is presented.

In chapter 2, various methods are used to eliminate the surfactant which is blocking the NP surface and hindering the optimum catalytic activity of Pd nanocubes.

In chapter 3, the influence of metal-support interactions on not only electronic structure but also electrochemical performance is reported.

In chapter 4, Pd@Pt core-shell NPs were surface doped with cobalt and the ORR activity and stability results are correlated with the acquired information about their electronic structure using XAS.

Al the reported studies will be concluded in chapter 5 and it comprises a brief summary of the thesis and future research proposal.

1.8 References

1. *Vielstich, W., Lamm, A. and Gasteiger, H.A., Handbook of fuel cells: fundamentals technology and applications. Vol. 2. 2003: Wiley New York.*

2. *Barbir, F., PEM fuel cells: theory and practice. 2012: Academic Press.*

3. *Kordesch, K. and Simader, G., Fuel cells and their applications. Vol. 117. 1996: VCh Weinheim.*

4. *Carrette, L., Friedrich, K. and Stimming, U., Fuel cells–fundamentals and applications. Fuel cells, 2001.* ***1****(1): p. 5-39.*

5. *Srinivasan, S., Fuel cells: from fundamentals to applications. 2006: Springer Science & Business media.*

6. *Winter, M. and Brodd, R.J., What are batteries, fuel cells, and supercapacitors?, 2004, ACS Publications.*

7. *Stambouli, A.B. and Traversa, E., Fuel cells, an alternative to standard sources of energy. Renewable and sustainable energy reviews, 2002.* ***6****(3): p. 295-304.*

8. *Andújar, J.M. and Segura, F., Fuel cells: History and updating. A walk along two centuries. Renewable and sustainable energy reviews, 2009.* ***13****(9): p. 2309-2322.*

9. *Carrette, L., Friedrich, K.A. and Stimming, U., Fuel cells: principles, types, fuels, and applications. ChemPhysChem, 2000.* ***1****(4): p. 162-193.*

10. *Spiegel, C., Designing and building fuel cells. Vol. 87. 2007: Citeseer.*

11. *Zhang, J., Xie, Z., Zhang, J.et al., High temperature PEM fuel cells. Journal of power Sources, 2006.* ***160****(2): p. 872-891.*

12. *Litster, S. and McLean, G., PEM fuel cell electrodes. Journal of power sources, 2004.* ***130****(1-2): p. 61-76.*

13. *Mehta, V. and Cooper, J.S., Review and analysis of PEM fuel cell design and manufacturing. Journal of power sources, 2003.* ***114****(1): p. 32-53.*

14. *Cleghorn, S., Ren, X., Springer, T.et al., PEM fuel cells for transportation and stationary power generation applications. International Journal of Hydrogen Energy, 1997.* ***22****(12): p. 1137-1144.*

15. *Basu, S., Fuel cell science and technology. 2007: Springer.*

16. *Merle, G., Wessling, M. and Nijmeijer, K., Anion exchange membranes for alkaline fuel cells: A review. Journal of Membrane Science, 2011.* ***377****(1-2): p. 1-35.*

17. *Kordesch, K., Hacker, V., Gsellmann, J.et al., Alkaline fuel cells applications. Journal of Power Sources, 2000.* ***86****(1-2): p. 162-165.*

18. *Gülzow, E., Alkaline fuel cells: a critical view. Journal of Power Sources, 1996.* ***61****(1-2): p. 99-104.*

19. *Sammes, N., Bove, R. and Stahl, K., Phosphoric acid fuel cells: Fundamentals and applications. Current opinion in solid state and materials science, 2004.* ***8****(5): p. 372-378.*

20. *Blomen, L.J. and Mugerwa, M.N., Fuel cell systems. 2013: Springer Science & Business Media.*

21. *Ellis, M.W., Von Spakovsky, M.R. and Nelson, D.J., Fuel cell systems: efficient, flexible energy conversion for the 21st century. Proceedings of the IEEE, 2001.* ***89****(12): p. 1808-1818.*

22. *Dicks, A.L., Molten carbonate fuel cells. Current Opinion in Solid State and Materials Science, 2004.* ***8****(5): p. 379-383.*

23. *Luo, M., Hong, Y., Yao, W.et al., Facile removal of polyvinylpyrrolidone (PVP) adsorbates from Pt alloy nanoparticles. Journal of Materials Chemistry A, 2015. 3(6): p. 2770-2775.*

24. *Antolini, E., The stability of molten carbonate fuel cell electrodes: A review of recent improvements. Applied energy, 2011.* ***88****(12): p. 4274-4293.*

25. *Bischoff, M., Molten carbonate fuel cells: A high temperature fuel cell on the edge to commercialization. Journal of Power Sources, 2006.* ***160****(2): p. 842-845.*

26. *Ormerod, R.M., Solid oxide fuel cells. Chemical Society Reviews, 2003.* ***32****(1): p. 17-28.*

27. *Jacobson, A.J., Materials for solid oxide fuel cells. Chemistry of Materials, 2009.* ***22****(3): p. 660-674.*

28. *Yamamoto, O., Solid oxide fuel cells: fundamental aspects and prospects. Electrochimica Acta, 2000.* ***45****(15-16): p. 2423-2435.*

29. *Lashtabeg, A. and Skinner, S.J., Solid oxide fuel cells—a challenge for materials chemists? Journal of Materials Chemistry, 2006.* ***16****(31): p. 3161-3170.*

30. *Mekhilef, S., Saidur, R. and Safari, A., Comparative study of different fuel cell technologies. Renewable and Sustainable Energy Reviews, 2012.* ***16****(1): p. 981-989.*

31. *Appleby, A.J., Fuel cell handbook. 1988.*

32. *Ogden, J.M., Steinbugler, M.M. and Kreutz, T.G., A comparison of hydrogen, methanol and gasoline as fuels for fuel cell vehicles: implications for vehicle design and infrastructure development. Journal of power sources, 1999.* ***79****(2): p. 143-168.*

33. *Kreuer, K., On the development of proton conducting polymer membranes for hydrogen and methanol fuel cells. Journal of membrane science, 2001.* ***185****(1): p. 29-39.*

34. *Thomas, C., James, B.D., Lomax Jr, F.D.et al., Fuel options for the fuel cell vehicle: hydrogen, methanol or gasoline? International Journal of Hydrogen Energy, 2000.* ***25****(6): p. 551-567.*

35. *Dohle, H., Divisek, J. and Jung, R., Process engineering of the direct methanol fuel cell. Journal of Power Sources, 2000.* ***86****(1-2): p. 469-477.*

36. *Barbir, F. and Gomez, T., Efficiency and economics of proton exchange membrane (PEM) fuel cells. International Journal of Hydrogen Energy, 1996.* ***21****(10): p. 891-901.*

37. *Haile, S.M., Fuel cell materials and components. Acta Materialia, 2003.* ***51****(19): p. 5981-6000.*

38. *Steele, B.C. and Heinzel, A., Materials for fuel-cell technologies, in Materials For Sustainable Energy: A Collection of Peer-Reviewed Research and Review Articles from Nature Publishing Group. 2011, World Scientific. p. 224-231.*

39. *Frey, T. and Linardi, M., Effects of membrane electrode assembly preparation on the polymer electrolyte membrane fuel cell performance. Electrochimica Acta, 2004.* ***50****(1): p. 99-105.*

40. *Hussain, M., Baschuk, J., Li, X.et al., Thermodynamic analysis of a PEM fuel cell power system. International Journal of Thermal Sciences, 2005.* ***44****(9): p. 903-911.*

41. *Larminie, J., Dicks, A. and McDonald, M.S., Fuel cell systems explained. Vol. 2. 2003: J. Wiley Chichester, UK.*

42. *Debe, M.K., Electrocatalyst approaches and challenges for automotive fuel cells. Nature, 2012.* ***486****(7401): p. 43.*

42. *Ge, J., et al., Controllable Synthesis of Pd Nanocatalysts for Direct Formic Acid Fuel Cell (DFAFC) Application: From Pd Hollow Nanospheres to Pd Nanoparticles. The Journal of Physical Chemistry C, 2007.* ***111****(46): p. 17305-17310.*

43. *Choi, J.H., et al., Formic acid oxidation by carbon-supported palladium catalysts in direct formic acid fuel cell. Korean Journal of Chemical Engineering, 2008.* ***25****(5): p. 1026-1030.*

44. *Zhu, Y., Z. Khan, and R. Masel, The behavior of palladium catalysts in direct formic acid fuel cells. Journal of Power Sources, 2005.* ***139****(1-2): p. 15-20.*

45. *Debe, M.K., Electrocatalyst approaches and challenges for automotive fuel cells. Nature, 2012.* ***486****(7401): p. 43.*

46. *Zhang, J., PEM fuel cell electrocatalysts and catalyst layers: fundamentals and applications. 2008: Springer Science & Business Media.*

47. *Bing, Y., Liu, H., Zhang, L.et al., Nanostructured Pt-alloy electrocatalysts for PEM fuel cell oxygen reduction reaction. Chemical Society Reviews, 2010. 39(6): p. 2184-2202.*

48. *Di Noto, V. and E. Negro, Development of nano-electrocatalysts based on carbon nitride supports for the ORR processes in PEM fuel cells. Electrochimica Acta, 2010.* ***55****(26): p. 7564-7574.*

49. *Stamenkovic, V.R., Mun, B.S., Arenz, M.et al., Trends in electrocatalysis on extended and nanoscale Pt-bimetallic alloy surfaces. Nature materials, 2007. 6(3): p. 241.*

50. *Long, N.V., et al., The development of mixture, alloy, and core-shell nanocatalysts with nanomaterial supports for energy conversion in low-temperature fuel cells. Nano Energy, 2013.* ***2****(5): p. 636-676.*

51. *Stamenkovic, V.R., Fowler, B., Mun, B.S.et al., Improved oxygen reduction activity on Pt3Ni (111) via increased surface site availability. science, 2007. 315(5811): p. 493-497.*

52. *Greeley, J., Stephens, I., Bondarenko, A.et al., Alloys of platinum and early transition metals as oxygen reduction electrocatalysts. Nature chemistry, 2009. 1(7): p. 552.*

53. *Zhang, J., Vukmirovic, M.B., Xu, Y.et al., Controlling the catalytic activity of platinum-monolayer electrocatalysts for oxygen reduction with different substrates. Angewandte Chemie International Edition, 2005. 44(14): p. 2132-2135.*

54. *Vukmirovic, M.B., Zhang, J., Sasaki, K.et al., Platinum monolayer electrocatalysts for oxygen reduction. Electrochimica Acta, 2007. 52(6): p. 2257-2263.*

55. *Mukerjee, S. and S. Srinivasan, Enhanced electrocatalysis of oxygen reduction on platinum alloys in proton exchange membrane fuel cells. Journal of Electroanalytical Chemistry, 1993.* ***357****(1-2): p. 201-224.*

56. *Jayasayee, K., Van Veen, J.R., Manivasagam, T.G.et al., Oxygen reduction reaction (ORR) activity and durability of carbon supported PtM (Co, Ni, Cu) alloys: Influence of particle size and non-noble metals. Applied Catalysis B: Environmental, 2012. 111: p. 515-526.*

57. *Antolini, E., Salgado, J., Giz, M.et al., Effects of geometric and electronic factors on ORR activity of carbon supported Pt–Co electrocatalysts in PEM fuel cells. International Journal of Hydrogen Energy, 2005. 30(11): p. 1213-1220.*

58. *Toyoda, E., Jinnouchi, R., Hatanaka, T.et al., The d-band structure of Pt nanoclusters correlated with the catalytic activity for an oxygen reduction reaction. The Journal of Physical Chemistry C, 2011. 115(43): p. 21236-21240.*

59. *Fouda-Onana, F., S. Bah, and O. Savadogo, Palladium–copper alloys as catalysts for the oxygen reduction reaction in an acidic media I: Correlation between the ORR kinetic parameters and intrinsic physical properties of the alloys. Journal of Electroanalytical Chemistry, 2009.* ***636****(1-2): p. 1-9.*

60. *Nilekar, A.U. and M. Mavrikakis, Improved oxygen reduction reactivity of platinum monolayers on transition metal surfaces. Surface Science, 2008.* ***602****(14): p. L89-L94.*

61. *Jaksic, J.M., et al., Electrocatalysis for hydrogen electrode reactions in the light of fermi dynamics and structural bonding FACTORS—I. individual electrocatalytic properties of transition metals. International journal of hydrogen energy, 1998.* ***23****(12): p. 1121-1156.*

62. *Leppert, L., R. Kempe, and S. Kümmel, Hydrogen binding energies and electronic structure of Ni–Pd particles: a clue to their special catalytic properties. Physical Chemistry Chemical Physics, 2015.* ***17****(39): p. 26140-26148.*

63. *Wang, C., Daimon, H., Onodera, T.et al., A general approach to the size-and shape-controlled synthesis of platinum nanoparticles and their catalytic reduction of oxygen. Angewandte Chemie International Edition, 2008. 47(19): p. 3588-3591.*

64. *Peng, Z. and H. Yang, Designer platinum nanoparticles: Control of shape, composition in alloy, nanostructure and electrocatalytic property. Nano Today, 2009.* ***4****(2): p. 143-164.*

65. *Chen, J., Lim, B., Lee, E.P.et al., Shape-controlled synthesis of platinum nanocrystals for catalytic and electrocatalytic applications. Nano Today, 2009. 4(1): p. 81-95.*

66. *Narayanan, R. and M.A. El-Sayed, Shape-dependent catalytic activity of platinum nanoparticles in colloidal solution. Nano letters, 2004.* ***4****(7): p. 1343-1348.*

67. *Nørskov, J.K., Rossmeisl, J., Logadottir, A.et al., Origin of the overpotential for oxygen reduction at a fuel-cell cathode. The Journal of Physical Chemistry B, 2004. 108(46): p. 17886-17892.*

68. *Song, C. and J. Zhang, Electrocatalytic oxygen reduction reaction, in PEM fuel cell electrocatalysts and catalyst layers. 2008, Springer. p. 89-134.*

69. *Marković, N., Schmidt, T., Stamenković, V.et al., Oxygen reduction reaction on Pt and Pt bimetallic surfaces: a selective review. Fuel cells, 2001. 1(2): p. 105-116.*

70. *Marković, N. and P. Ross Jr, Surface science studies of model fuel cell electrocatalysts. Surface Science Reports, 2002.* ***45****(4-6): p. 117-229.*

71. *Schmidt, T., Gasteiger, H., Stäb, G.et al., Characterization of high-surface-area electrocatalysts using a rotating disk electrode configuration. Journal of The Electrochemical Society, 1998. 145(7): p. 2354-2358.*

72. *Paulus, U., Schmidt, T., Gasteiger, H.et al., Oxygen reduction on a high-surface area Pt/Vulcan carbon catalyst: a thin-film rotating ring-disk electrode study. Journal of Electroanalytical Chemistry, 2001. 495(2): p. 134-145.*

73. *Merzougui, B. and S. Swathirajan, Rotating disk electrode investigations of fuel cell catalyst degradation due to potential cycling in acid electrolyte. Journal of the Electrochemical Society, 2006.* ***153****(12): p. A2220-A2226.*

74. *Hsueh, K., E. Gonzalez, and S. Srinivasan, Electrolyte effects on oxygen reduction kinetics at platinum: a rotating ring-disc electrode analysis. Electrochimica Acta, 1983.* ***28****(5): p. 691-697.*

75. *Wagner, N., Characterization of membrane electrode assemblies in polymer electrolyte fuel cells using ac impedance spectroscopy. Journal of Applied Electrochemistry, 2002.* ***32****(8): p. 859-863.*

76. *Park, J.-S., Choi, J.-H., Woo, J.-J.et al., An electrical impedance spectroscopic (EIS) study on transport characteristics of ion-exchange membrane systems. Journal of colloid and interface science, 2006. 300(2): p. 655-662.*

77. *Winick, H. and S. Doniach, Synchrotron radiation research. 2012: Springer Science & Business Media.*

78. *Sokolov, A.A. and I.M. Ternov, Synchrotron radiation. Akademia Nauk SSSR, Moskovskoie Obshchestvo Ispytatelei prirody. Sektsia Fiziki. Sinkhrotron Radiation, Nauka Eds., Moscow, 1966 (Russian title: Sinkhrotronnoie izluchenie), 228 pp., 1966.*

79. *Koch, E.-E., Handbook on synchrotron radiation. Vol. 1. 1983.*

80. *Onuki, H. and P. Elleaume, Undulators, wigglers and their applications. 2003: CRC Press.*

81. *Kunz, C., Synchrotron radiation. 1974.*

82. *Sham, T.-K., Chemical applications of synchrotron radiation. 2002: World Scientific.*

83. *Sham, T. and M.L. Rivers, A brief overview of synchrotron radiation. Reviews in mineralogy and geochemistry, 2002.* ***49****(1): p. 117-147.*

84. *Balerna, A. and S. Mobilio, Introduction to synchrotron radiation, in Synchrotron radiation. 2015, Springer. p. 3-28.*

85. *Koningsberger, D., Mojet, B., Van Dorssen, G.et al., XAFS spectroscopy; fundamental principles and data analysis. Topics in catalysis, 2000. 10(3-4): p. 143-155..*

86. *Bunker, G., Introduction to XAFS: a practical guide to X-ray absorption fine structure spectroscopy. 2010: Cambridge University Press.*

87. *Newville, M., IFEFFIT: interactive XAFS analysis and FEFF fitting. Journal of synchrotron radiation, 2001.* ***8****(2): p. 322-324.*

88. *Newville, M., Fundamentals of XAFS. Reviews in Mineralogy and Geochemistry, 2014.* ***78****(1): p. 33-74.*

89. *Alia, S.M., Ngo, C., Shulda, S.et al., Exceptional oxygen reduction reaction activity and durability of platinum–nickel nanowires through synthesis and post-treatment optimization. ACS Omega, 2017. 2(4): p. 1408-1418.*

90. *Mansour, A., J. Cook Jr, and D. Sayers, Quantitative technique for the determination of the number of unoccupied d-electron states in a platinum catalyst using the L2, 3 X-ray absorption edge spectra. The Journal of Physical Chemistry, 1984.* ***88****(11): p. 2330-2334.*

91. *Teo, B. and D. Joy, EXAFS spectroscopy. Techniques and Applications, 1981.*

92. *Teo, B.K., EXAFS: basic principles and data analysis. Vol. 9. 2012: Springer Science & Business Media.*

93. *Iwasawa, Y., K. Asakura, and M. Tada, XAFS techniques for catalysts, nanomaterials, and surfaces. 2017: Springer.*

94. *Koningsberger, D. and R. Prins, X-ray absorption: principles, applications, techniques of EXAFS, SEXAFS, and XANES. 1988.*

95. *Jaklevic, J., Kirby, J., Klein, M.et al., Fluorescence detection of exafs: Sensitivity enhancement for dilute species and thin films. Solid State Communications, 1977. 23(9): p. 679-682.*

Chapter 2

2 Morphology and Catalytic Performance of Palladium Nanocubes

2.1 Introduction

High power density, lower fuel crossover through the Nafion® membrane and the feasibility of using less expensive catalysts have made direct formic acid fuel cell (DFAFC) a promising alternative for current energy resources [1-3].

Palladium nanoparticles have shown to have an incredible activity for catalyzing the formic acid oxidation [4, 5]. Tuning the particle size, shape, and composition can further enhance the catalytic activity of these NPs and this can be achieved by the utilization of colloidal chemistry [6-8]. The capping agents and the surfactants that are being used for colloidal synthesis not only control the growth of NPs in the desired directions but also inhibit the NPs aggregation [9]. However, the adsorbed capping agents on NPs can be problematic in term of limiting the access of reactant molecules to the surface of the catalyst which can confine the catalyst activity [9, 10].

Although there are various implemented methods for removal of capping agents, their influence on the electrocatalytic activity of catalysts is still not obvious. So, developing an efficient way for eliminating the surfactant and capping agents from the surface of nanoparticles, with considering the catalytic activity, will be the matter of this study. In order to optimize the elimination of Poly(vinylpyrrolidone) (PVP) from Pd nanocube, different procedures such as calcination, acid washing, and UV-Ozone irradiation were utilized in this study. Monitoring the influences of cleaning processes on NPs has been conducted by the usage of transmission electron microscopy (TEM), X-ray diffraction (XRD), Raman, and X-ray absorption spectroscopy (XAS). Among all the studied cleaning procedures, low-temperature calcination (170 ℃) is found to be simultaneously efficient in PVP elimination, catalytic activity enhancement, and morphology and size preserving.

2.2 Experimental Section

2.2.1 Material Synthesis

The first step in optimizing the surfactant cleaning procedures is synthesizing cubic palladium. To obtain the size-controlled palladium nanocubes, poly(vinylpyrrolidone) (105 mg), ascorbic acid (60 mg), and potassium bromide (600 mg) were all pre-heated in 8 mL of DI water at the temperature of 80 °C. After 10 minutes of heating and stirring, an aqueous solution containing Na_2PdCl_4 (57 mg) was pipetted into the vial and the reaction was proceeded at the same temperature for another 3 hours [11]. Synthesized products were then collected by centrifugation and were dispersed in DI water for further utilization. SEM and TEM figures of the as-synthesized product confirm that they are palladium nanocubes as shown in Figure 2-1.

As the as-synthesized catalysts are not sufficiently clean for electrochemical applications and their surface is blocked because of the surfactant utilization, various methods were employed in this study to eliminate the organic compounds from the catalysts surface. Removing surfactant and capping agents can make the synthesized catalysts agglomerated, so catalysts were first loaded on carbon support before performing any of the cleaning procedures [12]. To obtain 20% loading of palladium, a specific amount of carbon black was added to the palladium suspension, of which its concentration was known by ICP-MS, and the obtained mixture was ultrasonicated overnight. The obtained supported catalysts are shown in Figure 2-1-C.

2.2.2 Characterization

A wide variety of characterization methods is used to determine the features of these NPs. Fundamental and performance behavior of these catalysts is revealed utilizing Scanning Electron Microscope (SEM, Zeiss 1540XB), Transmission Electron Microscope (TEM, Phillips CM10), X-ray Powder Diffraction (XRD), Inductively coupled plasma mass spectrometry (ICP-MS), Raman spectroscopy, and XAS at Canadian Light Source. All electrochemical measurements were carried out with CHI-610C potentiostat in a three-electrode cell. A Glassy carbon electrode, Ag/AgCl electrode and platinum wire were used as working, reference and counter electrode in the electrochemical measurements.

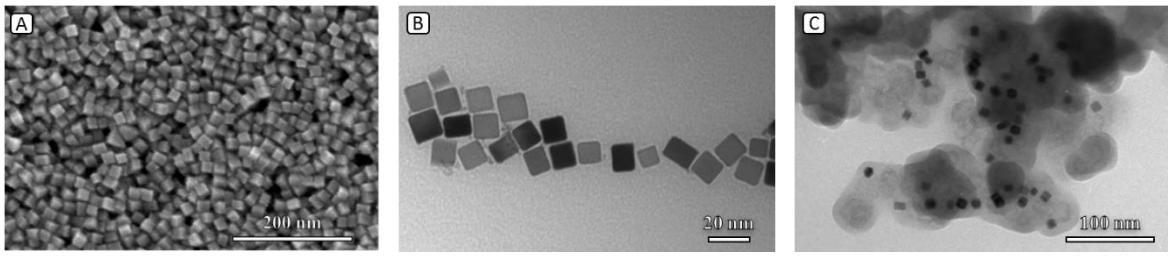

Figure 2-1 A) SEM and B) TEM images of as-synthesized cubic Pd nanoparticles. C) TEM image of Pd nanocubes loaded on carbon black.

2.3 Results and Discussion

It is well-known that synthesizing catalyst in some specific size, shape, and composition can enhance their catalytic activity and can make them get close to the desired requirements. One of the most recent ways in synthesizing nanoparticles in the desired facet is colloidal chemistry, which uses some specific organic compounds as surfactant [13]. Although colloidal chemistry with all its particular features can overcome the challenges of shape and size controlling, the necessity of utilizing organic compounds is still an obstacle in catalysis science [14]. These organic compounds which are mostly poly(vinylpyrrolidone) (PVP), oleylamine, or hexadecyl trimethyl ammonium bromide (CTAB) will adhere to the initial nuclei of the reduced metal and will hinder its growth to a favorable direction [15]. These organic compounds, with their high affinity to the metal surface, will also reduce the chance of aggregation in nanoparticles and will alter the surface energy of reduced metals. While having a strong adsorption will be the first requirement of these surfactants, their elimination after the synthesis procedure will have an equal importance [16]. Adsorbed surfactants on the surface of nanoparticles will block the active sites and they will be an impediment in the utilization of nanoparticles as catalysts, of which a clean surface with available active sites is critical [17].

PVP, the most prevalent surfactant, is being used in our study. This organic compound will adhere to the surface of nanoparticles and will block their active sites from contacting the electrolyte [16, 18]. This detrimental role of PVP, which is affecting the catalytic activity of synthesized nanoparticles, is shown in a schematic in Figure 2-2. As it is obvious in Figure 2-2, the surface of palladium is completely covered with PVP and its existence on the surface is hindering the faradaic reactions and the surface contact with reactants. So, it is necessary to find an efficient way for

removing these surfactants and capping agents and that the surface sites can enhance their electrochemical activity.

In order to optimize the elimination of PVP from Pd nanocube, different procedures such as calcination, acid washing, and UV-Ozone irradiation were utilized in this study. While each cleaning procedure can be adequately efficient in surfactant elimination, their influence on nanoparticle morphology and catalytic performance is still unclear [19]. Herein, the acquired nanoparticles, after each cleaning method were used as a catalyst for formic acid oxidation to determine the most efficient surfactant removal method.

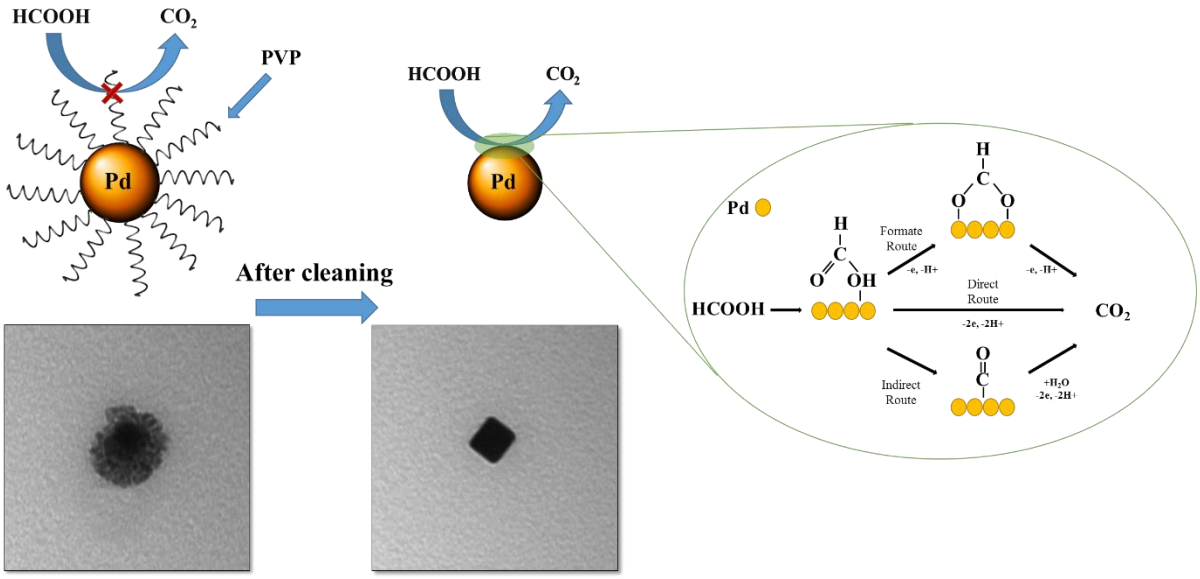

Figure 2-2 Schematic picture of PVP capped palladium before and after cleaning and the possible reaction pathways of formic acid oxidation on Pd/C nanocubes.

2.3.1 Calcination

One of the most advantageous ways of removing PVP is using calcination procedure [16]. In this procedure the catalyst first will be heated up to the PVP decomposition temperature (170–450 °C) in a 20% O_2/Ar atmosphere and then the heat-treated catalyst will be exposed to the 20% H_2/Ar atmosphere at the same temperature to reduce the probable oxidized catalysts. This is an efficient way of removing PVP, however in high temperature, particle aggregation and shape change cannot be avoided [20]. So optimizing the temperature and the time of calcination is essential to not only

remove the maximum amount of PVP but also keep the initial shape and size. In order to find an efficient temperature for calcination, Pd nanocubes were exposed to a range of temperatures starting from 170 °C, which will be the initial temperature of PVP decomposition. Samples were then dispersed in a solution containing DI water, 2-propanol, and Nafion to obtain the required ink for electrochemical characterizations. The prepared ink was then loaded on glassy carbon electrode for obtaining their cyclic voltammetry curves in H_2SO_4 electrolyte, with and without formic acid. Employing ICP-MS, palladium loading on the electrode was controlled to be 30 µg.cm^{-2} for all the catalysts.

As it is shown in Figure 2-5, CV of untreated sample is not showing any specific features of palladium nanoparticle and there is no underpotential deposited hydrogen (H_{upd}) region, which is representative of surface active sites. After calcination of samples at the temperature of 170-300 °C, hydrogen adsorption/desorption region, which is in the potential range of 0.06–0.40 V_{RHE}, will start to arise and surfactants will be oxidized from the surface. The CVs of these calcinated samples are shown in Figure 2-3 and their change based on temperature is vivid. Based on the obtained electrochemical surface active area and FAO activity, 170 °C will be the optimum temperature and higher temperature will oxidize the surface and further decrease the catalytic performance of Pd. It is also imperative to know the stability of these catalysts after cleaning procedures. By employing chronoamperometry method at a constant potential of 0.4 V_{RHE}, HT-170 sample has kept a higher fraction of its initial current. Calculated ECSA, mass activity, and stability are all presented in Table 2-1.

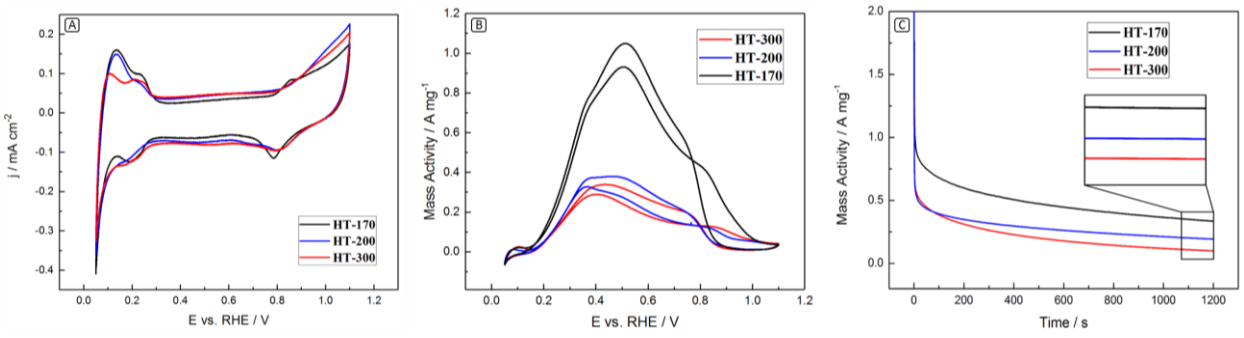

Figure 2-3 Cyclic voltammograms acquired on various calcinated Pd/C samples in the solution of A) 0.5 M H_2SO_4 at the scan rate of 50 mVs^{-1} B) 0.5 M HCOOH + 0.5 M H_2SO_4

at the scan rate of 10 mVs^{-1}. C) Chronoamperometric curves for the oxidation of 0.5 M HCOOH in 0.5 M H_2SO_4 solution at the constant potential of 0.4 V_{RHE}.

2.3.2 UV-Ozone Irradiation

UV-Ozone has been widely used for cleaning purposes and it can decompose organic impurities to volatile materials such as water or carbon dioxide. UV-Ozone is composed of ultraviolet light, emitting wavelengths of 185 nm, which can produce ozone out of molecular oxygen, and 257 nm, which can be beneficial in the excitation of organic impurities [21]. All these features together can be an advantageous technique for the elimination of carbon-containing compounds from palladium surface [22]. In order to clean the synthesized Pd/C, samples were placed in a custom-made chamber with having a specific distance from ultraviolet lamp's tube. These samples were irradiated for particular times under a Bulbtronics 16 W low-pressure mercury lamp and then were taken out of the chamber. Although this technique can maintain the morphology of Pd nanocubes because of its low employed temperature, the strong oxidizing environment of UV-Ozone chamber can change the catalysts surface [23]. The atomic oxygen, which will be produced in the process of ozone formation and decomposition, will have a high oxidizing capability and can even oxidize the catalysts surface in long exposure time. UV-Ozone treatment can be also unpredictable in producing some organic intermediates out of the initial organic impurity [24]. All these will lead us to that optimizing the exposure time to UV-Ozone is so essential to remove the maximum amount of PVP and increasing the catalytic activity, simultaneously.

In order to compare the catalytic performance of palladium nanoparticles after UV-Ozone treatment, CVs of treated samples with and without formic acid is shown in Figure 2-4. Based on the presented CV in Figure 2-4, by starting from 10 minutes to 30 minutes of treatment, the ECSA is increasing and its mass activity towards FAO is maximized. By further increasing the exposure time of UV-Ozone, the active sites of Pd are again decreasing and this will lead to a limited mass activity for formic acid oxidation. Unless the previous references which were knowing the higher exposure time as an efficient way of surfactant removal, the high exposure time will partially oxidize the surface of the catalyst and can decompose PVP to some undesirable intermediates such as CO, which have high affinity to the Pd and can block its surface [25].

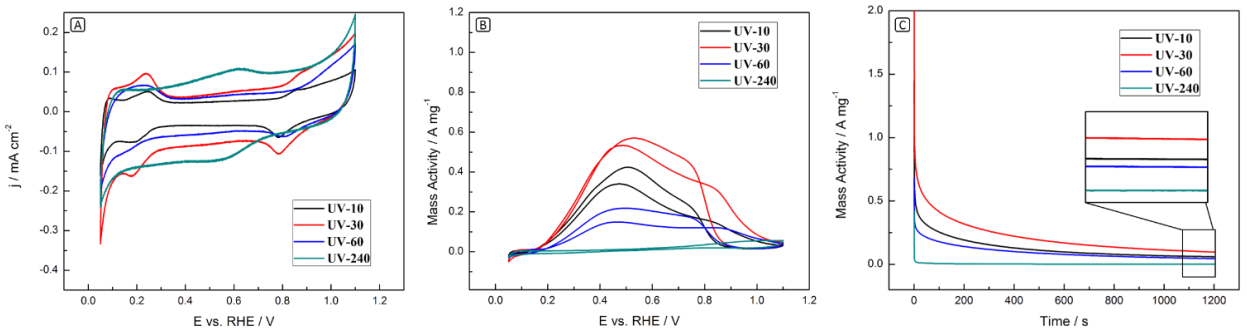

Figure 2-4 Cyclic voltammograms acquired on various UV-treated Pd/C samples in the solution of A) 0.5 M H_2SO_4 at the scan rate of 50 mVs-1 B) 0.5 M HCOOH + 0.5 M H_2SO_4 at the scan rate of 10 mVs^{-1}. C) Chronoamperometric curves for the oxidation of 0.5 M HCOOH in 0.5 M H_2SO_4 solution at the constant potential of 0.4 V_{RHE}.

2.3.3 Acid Washing

Using acetic acid at the temperature of 60°C can be known as another efficient way for removing capping agent and is being used in recent research [16]. By utilizing acetic acid, the protonated amino groups of the surfactant will lose their strong affinity to the metal surface and will be much easier to wash surfactants by further ethanol/water washing.

The disadvantage of using acetic acid is that although it removes PVP partly, you will introduce a large amount of oxygen functional groups to the carbon support and this will influence the stability and conductivity of the carbon support [26]. In addition, acid washing can leach out some of the metals from NPs and this can influence their shape and composition.

By comparing their electrochemical performance, which is presented in Figure 2-5, it is shown that acid washing has enhanced the electrochemical surface-active area and mass activity of palladium catalyst. The chronoamperometry curve is also showing an enhancement in stability of the catalyst after acid washing. These CVs are confirming the positive influence of acetic acid in eliminating the PVP. However, by having a look at all cleaning methods, acid washing is still not the best cleaning procedure based on the measured catalytic performance.

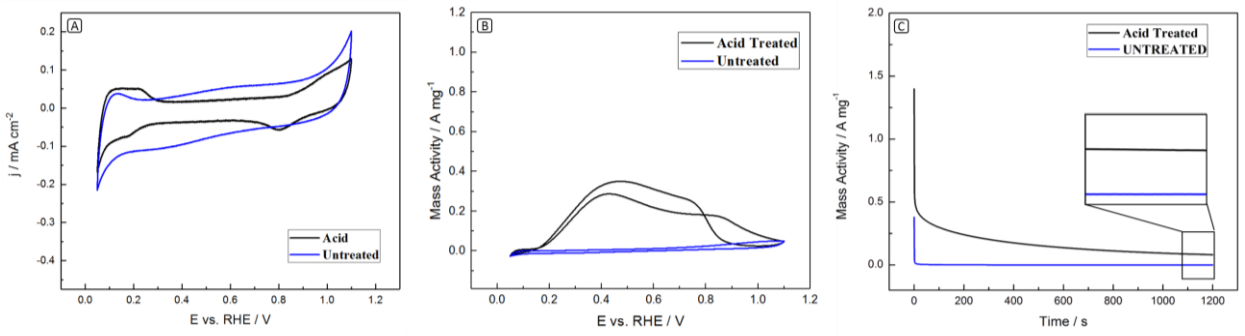

Figure 2-5 Cyclic voltammograms acquired on acid-treated Pd/C sample in the solution of A) 0.5 M H_2SO_4 at the scan rate of 50 mVs^{-1} B) 0.5 M HCOOH + 0.5 M H_2SO_4 at the scan rate of 10 mVs^{-1}. C) Chronoamperometric curves for the oxidation of 0.5 M HCOOH in 0.5 M H_2SO_4 solution at the constant potential of 0.4 V_{RHE}.

All these electrochemical performances are quantitatively presented in Table 2-1. The first shown parameter is ECSA which is showing electrochemical surface active area. An efficient PVP elimination method should provide more active sites on Pd surface and enhance its ECSA as a resultant. Among all the employed methods, HT-170 is showing to have the highest ratio of active sites compared to others. Having higher mass activity is also an imperative parameter for comparing the catalytic performance of catalysts. This parameter which is obtained by dividing the peak current of forming acid oxidation by the utilized amount of palladium, is confirming the efficiency of HT-170 treatment compared to other procedures. Lower onset potential of calcination method is also showing the facile pathway for the start of FAO on its surface. Comparing these vital parameters with catalysts stability, it is obvious that HT-170 sample will have the highest activity and stability towards formic acid oxidation (FAO).

Table 2-1 Comparison of the electrocatalytic properties of treated Pd/C samples for formic acid oxidation (FAO).

Sample	ECSA (m^2/g)	I_p ($A\ mg^{-1}$)	E_{onset} (mV)	$\frac{j\ t = 1200\ s}{j\ t = 10\ s}$
Acid Treated	19.5	0.29	164	20.0 %
HT-170	60.9	0.93	88	40.5 %
HT-200	42.8	0.32	165	39.7 %

HT-300	30.0	0.29	167	19.4 %
UV-10	9.9	0.34	160	15.8 %
UV-30	28.4	0.53	160	15.6 %
UV-60	17.3	0.14	198	18.1 %
UV-240	0.5	-	-	-
Untreated	-	-	-	-

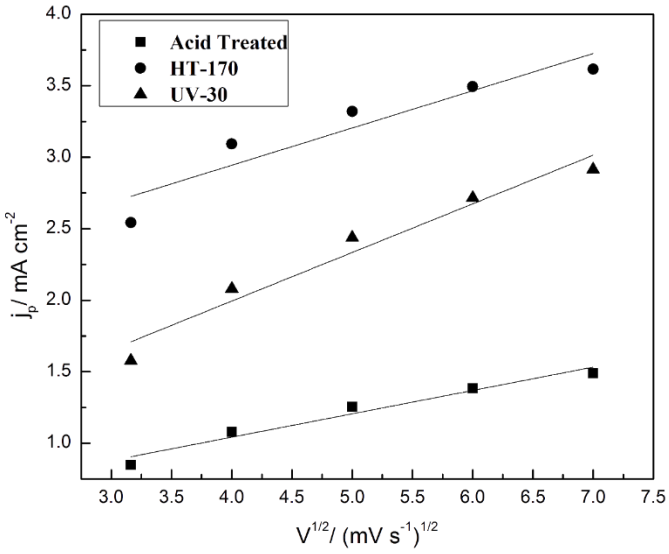

Figure 2-6 Relation of peak current density of treated samples with the square root of scan rates in 0.5 M H_2SO_4 solution containing 0.5 M HCOOH. The solid lines are based on a linear least-square fit of the data.

Now the optimum condition of each cleaning method, HT-170 in calcination method, UV-30 in UV-Ozone treatment and acid washing, will be chosen and be compared with each other in terms of the reaction mechanism. As it can be seen in Figure 2-6, the peak current of FAO depends linearly on the square root of scan rate for these samples. This linear relation demonstrates that the FA oxidation on these samples is a diffusion-controlled process [27]. This is showing that the formic acid oxidation reaction is being controlled by the diffusion of reactant species to the electrode surface. The value of the diffusion coefficient (*D*), which is showing the charge transfer within the diffusion layer adjacent to the electrode, can be obtained by using the following equation and can assist in opting the best treated catalyst.

$$i_p = (2.69 \times 10^5) n^{3/2} A D_0^{1/2} C_0^* v^{1/2} \quad (1)$$

Where *n*, *A*, C_0* are defining electron transfer number, electrode area, and initial concentration respectively.

Considering the same number of *n*, *A*, C_0* for all these catalysts, diffusion coefficient, *D*, can be obtained. The higher diffusion coefficient will confirm the existence of higher active surface sites and higher availability for oxidation on catalysts and the following equation is used to compare this important parameter.

$$D_{\text{HT-170}} > D_{\text{UV-30}} > D_{\text{Acid Treated}}$$

It is calculated that calcination at the temperature of 170°C can enhance the Pd diffusion coefficient to the highest value possible.

Until now, the electrochemical characterizations have shown us the best cleaning methods for surfactant removal from Pd surface. However, the influence of these methods on surface of catalysts and the surface alteration resulted from these methods is still unclear. To further discuss these effects and to fundamentally investigate the morphology and structure of treated samples, X-ray absorption spectroscopy, Raman Spectroscopy and XRD were utilized.

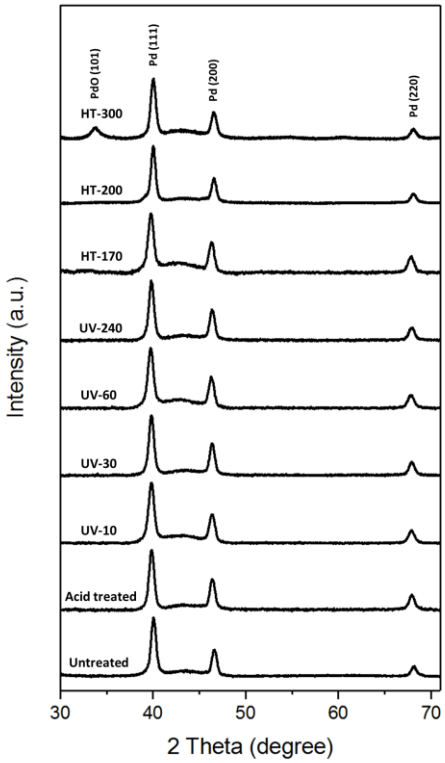

Figure 2-7 X-ray diffraction patterns of palladium catalysts before and after removal of surfactant with various treatment methods.

To further discuss on the morphology of these nanoparticles before and after treatment, XRD measurements were employed and are shown in Figure 2-7. XRD data is confirming the existence of metallic f.c.c Pd structure on almost all samples, even after a prolonged exposure to oxidizing environments. The only obvious oxidation is regarding to the HT-300 in which the high temperature calcination of the sample has oxidized the surface of Pd and has diminished its activity and a PdO peak appears. Some broad features could be also observed due to the presence of amorphous materials on the surface. Although there is no additional peak in other XRD patterns of treated samples, there is still a big chance that the surface change induced by cleaning methods is not identifiable by XRD, because of its low surface sensitivity and bulk measurement. So other techniques have been employed in this study to determine the surface alteration of these catalysts.

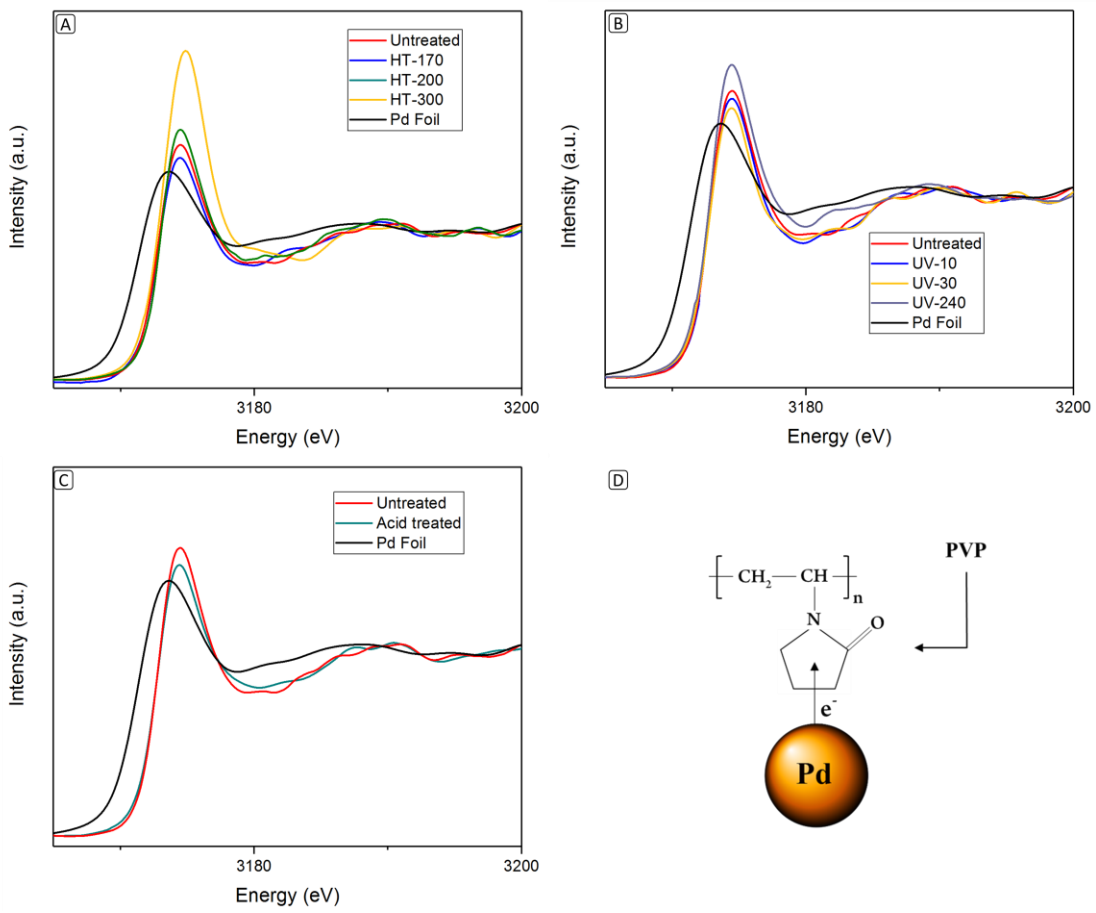

Figure 2-8 (A-C) Pd L_3-edge TEY-XANES spectra of carbon supported palladium catalysts after cleaning treatments, compared to untreated sample and Pd foil. D) Scheme proposed for the Pd nanoparticle interaction with PVP.

Because of the limited capability of previous techniques in probing the surface features of Pd nanocubes, after undergoing the treatments, XANES has been utilized in this study. X-ray absorption near edge structures, which can provide fundamental information about chemical bonding, electronic structure, and surface chemistry, has been acquired in surface-sensitive total electron yield (TEY) mode and has revealed the PVP/Pd interaction [28].

The palladium L_3-edge of carbon supported Pd nanocubes are shown in Figure 2-8. The first sharp peak in the data, which is the resultant of $2p_{3/2}$ to $4d_{5/2,3/2}$ transition, is called whiteline and is the main characteristic of unoccupied palladium densities of 4d state at the Fermi level [29]. The higher intensity of whiteline is confirming the higher number of d-band vacancies, which is allowing the transition of higher number of electrons to $4d_{5/2,\ 3/2}$ [30]. By having a look at XANES

data in Figure 2-8, it is obvious that samples are having lower whiteline intensity after the first steps of treatment. This is endorsing the PVP/Pd interaction which is a charge transfer from Pd to PVP [31] resulting in a threshold shift to higher photon energy and a sharper WL though narrower. By eliminating the PVP, lower numbers of electrons will be transferred to PVP and this will make palladium to have less unoccupied d state and this will lower its whiteline intensity in XANES measurements [32]. This can be a characteristic feature of PVP elimination for future studies, utilizing XAS measurement. Although the PVP removal should lower the whiteline intensity of palladium samples, calcination and UV-Ozone treatment are showing a distinct behavior after their employment. Thus, PVP removal is inevitably accompanied by surface oxidation but to a lesser extent than a fully oxidized PdO. These data are further confirming our assumption in previous sections that calcination at higher temperatures and UV irradiation for longer time can harmfully alter the catalyst surface and can partially oxidize it [33]. So, there will be an optimum time for UV treatment which is 30 minutes and after that with having more exposure time, although PVP is being removed, the surface is being oxidized simultaneously. There is a same situation for calcination and treating samples with higher temperature than 170°C can oxidize the catalyst and influence its electrochemical behavior. A partially oxidized surface is still more effective than a surface blocked by PVP and active sites can be regenerated with hydrogen.

As shown in Figure 2-8, after cleaning treatments, the area under the whiteline is decreasing and this is confirming the decrease in the 4d unoccupied density of states. This feature is showing that Pd is donating an electron to the PVP and this is unveiling that PVP being adsorbed on Pd surface with its N atom in the ring, as O atom in PVP will have the electron donor feature [34]. Therefore, among the two common cases of PVP chemisorption on Pd surface with either O atom or N atom, PVP ligand is having an interaction through its N atom and this electron donation is being done by its nitrogen atom [35].

It is obvious that the surface chemistry of the support will not only influence the catalytic activity of the catalyst but also will be imperative in its operational stability [36]. Raman spectroscopy with its specific features is a fruitful technique which can determine the graphitic and disordered structure of carbon materials and can analyze their surface chemistry [37]. In our study, Raman can be advantageous to show the surface modification of the carbon support after implementation of various cleaning procedures. The ratio of I_D to I_G bands, which are centered at 1350 cm^{-1} and

1600 cm^{-1} respectively, is mainly a characteristic parameter in this technique and is employed in this study to unveil the disordered structure of carbon material. Raman spectroscopy of supported palladium, which is shown in Figure 2-9, is confirming that each treatment can have different effects on the carbon support and can modify its crystal structure distinctly. Multiple Raman spectra were recorded for each sample and the averaged spectrum is shown in Figure 2-9. Based on the obtained I_D/I_G ratio, which is presented in Table 2-2, by calcinating the samples at high temperatures, carbon support will be oxidized and the defects will be increased. This enhancement in the defects ratio which is coming from oxidizing the surface and introducing oxygen functional groups to the support, is detrimental for the ultimate performance of the catalyst for formic acid oxidation [38, 39]. The evolution of Raman spectroscopy as a result of UV irradiation time is also showing an increase in defect peak compared to the G band. It can be concluded that UV-Ozone treatment can introduce a high level of functional groups to the surface of carbon even in the lowest exposure time and can generate defects sites through the graphitic crystal structure of carbon. Acid washed sample with its highest defect to graphitic ratio is also confirming the detrimental influence of acid washing on the carbon support and its role to adsorb a high ratio of oxygen functional groups on the surface [26].

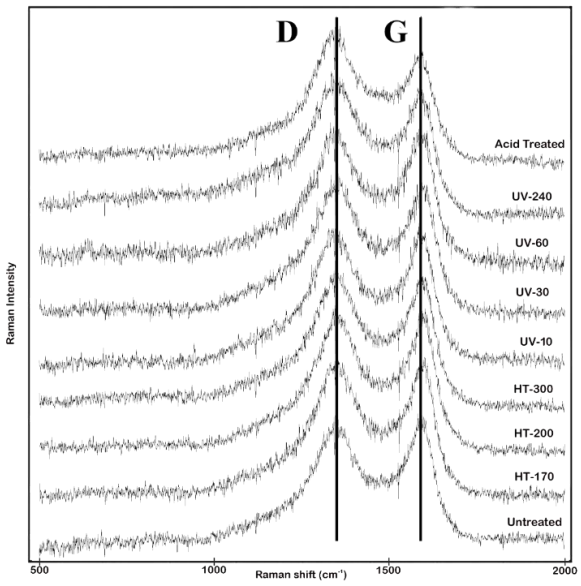

Figure 2-9 Raman spectra of Pd/C nanocubes before and after cleaning treatments.

The introduced defects to the carbon support through any of these cleaning techniques can be representative of the elimination of π-conjugated electron states near the Fermi level [40]. This alteration in the electronic structure of carbon support can lead to an enhanced electrical resistance which can be disadvantageous for the electrochemical outcome. It is also worth mentioning that the high oxidizing environment of UV-Ozone treatment is a result of the high reactive singlet oxygen atom which can have the role of oxidizing for the current defects or generating new defects.

Table 2-2 Ratio of D-band and G-band peaks intensity, obtained from Raman spectra, after surfactant cleaning.

Treatment Method	I_D/I_G
Acid Treated	1.09
HT-170	0.96
HT-200	1.01
HT-300	1.04
UV-10	0.97
UV-30	1.01
UV-60	1.03
UV-240	1.08
Untreated	0.98

2.4 Conclusions

All the above-discussed results will lead us to the conclusion that surfactant removal procedures should be tried to be optimum in both temperature and time. By having an extended time for the cleaning, more features of the catalyst and its support will be changed and this will not be acceptable for their required electrochemical performance. Although increasing temperature for calcination and time for UV-Ozone treatment can remove a higher percentage of PVP, it can influence the surface of the catalyst and its carbon support as well. Oxidizing the catalyst in high temperature calcination, adsorption of oxygen-containing intermediates on catalyst and surface oxidizing the NPs in UV-Ozone treatment and influencing the catalyst support in acid washing, has made 170°C calcination a promising cleaning procedure for elimination of PVP surfactant from Pd nanoparticles.

2.5 References

1. *Wang, Y., He, Q., Wei, H.et al., Optimal Electrocatalytic Pd/MWNTs nanocatalysts toward formic acid oxidation. Electrochimica acta, 2015.* ***184****: p. 452-465.*

2. *Morgan, R.D., Salehi-khojin, A. and Masel, R.I., Superior formic acid oxidation using carbon nanotube-supported palladium catalysts. The Journal of Physical Chemistry C, 2011.* ***115****(39): p. 19413-19418.*

3. *Wang, Q., Wang, Y., Guo, P.et al., Formic acid-assisted synthesis of palladium nanocrystals and their electrocatalytic properties. Langmuir, 2014.* ***30****(1): p. 440-446.*

4. *Klinkova, A., De Luna, P., Sargent, E.H.et al., Enhanced electrocatalytic performance of palladium nanoparticles with high energy surfaces in formic acid oxidation. Journal of Materials Chemistry A, 2017.* ***5****(23): p. 11582-11585.*

5. *Yang, S., Dong, J., Yao, Z.et al., One-pot synthesis of graphene-supported monodisperse Pd nanoparticles as catalyst for formic acid electro-oxidation. Scientific reports, 2014.* ***4****: p. 4501.*

6. *Wang, Y., Xie, S., Liu, J.et al., Shape-controlled synthesis of palladium nanocrystals: a mechanistic understanding of the evolution from octahedrons to tetrahedrons. Nano letters, 2013.* ***13****(5): p. 2276-2281.*

7. *Vidal-Iglesias, F.J., Aran-Ais, R.M., Solla-Gullon, J.et al., Shape-dependent electrocatalysis: formic acid electrooxidation on cubic Pd nanoparticles. Physical Chemistry Chemical Physics, 2012.* ***14****(29): p. 10258-10265.*

8. *Kim, S.-W., Park, J., Jang, Y.et al., Synthesis of monodisperse palladium nanoparticles. Nano Letters, 2003.* ***3****(9): p. 1289-1291.*

9. *Liu, Z., Shamsuzzoha, M., Ada, E.T.et al., Synthesis and activation of Pt nanoparticles with controlled size for fuel cell electrocatalysts. Journal of power sources, 2007.* ***164****(2): p. 472-480.*

10. *Koenigsmann, C., Santulli, A.C., Gong, K.et al., Enhanced electrocatalytic performance of processed, ultrathin, supported Pd–Pt core–shell nanowire catalysts for the oxygen reduction reaction. Journal of the American Chemical Society, 2011.* ***133****(25): p. 9783-9795.*

11. *Liu, X., Li, Z., Wang, K.et al., Facile Synthesis of Pd Nanocubes with Assistant of Iodide and Investigation of Their Electrocatalytic Performances Towards Formic Acid Oxidation. Nanomaterials, 2019.* ***9****(3): p. 375.*

12. *Niu, Z. and Li, Y., Removal and utilization of capping agents in nanocatalysis. Chemistry of Materials, 2013.* ***26****(1): p. 72-83.*

13. *Lee, H., Utilization of shape-controlled nanoparticles as catalysts with enhanced activity and selectivity. RSC Advances, 2014.* ***4****(77): p. 41017-41027.*

14. *Søbjerg, L.S., Lindhardt, A.T., Skrydstrup, T.et al., Size control and catalytic activity of bio-supported palladium nanoparticles. Colloids and Surfaces B: Biointerfaces, 2011.* ***85****(2): p. 373-378.*

15. *Kronberg, B., Holmberg, K. and Lindman, B., Surface chemistry of surfactants and polymers. 2014: John Wiley & Sons.*

16. *Li, D., Wang, C., Tripkovic, D.et al., Surfactant removal for colloidal nanoparticles from solution synthesis: the effect on catalytic performance. Acs Catalysis, 2012.* ***2****(7): p. 1358-1362.*

17. *Rioux, R., Song, H., Grass, M.et al., Monodisperse platinum nanoparticles of well-defined shape: synthesis, characterization, catalytic properties and future prospects. Topics in Catalysis, 2006.* ***39****(3-4): p. 167-174.*

18. *Luo, M., Hong, Y., Yao, W.et al., Facile removal of polyvinylpyrrolidone (PVP) adsorbates from Pt alloy nanoparticles. Journal of Materials Chemistry A, 2015.* ***3****(6): p. 2770-2775.*

19. *Lopez-Sanchez, J.A., Dimitratos, N., Hammond, C.et al., Facile removal of stabilizer-ligands from supported gold nanoparticles. Nature chemistry, 2011.* ***3****(7): p. 551.*

20. *Campisi, S., Schiavoni, M., Chan-Thaw, C.et al., Untangling the role of the capping agent in nanocatalysis: recent advances and perspectives. Catalysts, 2016.* ***6****(12): p. 185.*

21. *Vig, J.R., UV/ozone cleaning of surfaces. Journal of Vacuum Science & Technology A: Vacuum, Surfaces, and Films, 1985.* ***3****(3): p. 1027-1034.*

22. *Aliaga, C., Park, J.Y., Yamada, Y.et al., Sum frequency generation and catalytic reaction studies of the removal of organic capping agents from Pt nanoparticles by UV− ozone treatment. The Journal of Physical Chemistry C, 2009.* ***113****(15): p. 6150-6155.*

23. *Menard, L.D., Xu, F., Nuzzo, R.G.et al., Preparation of TiO2-supported Au nanoparticle catalysts from a Au13 cluster precursor: Ligand removal using ozone exposure versus a rapid thermal treatment. Journal of Catalysis, 2006.* ***243****(1): p. 64-73.*

24. *Crespo-Quesada, M., Andanson, J.-M., Yarulin, A.et al., UV–ozone cleaning of supported poly (vinylpyrrolidone)-stabilized palladium nanocubes: effect of stabilizer removal on morphology and catalytic behavior. Langmuir, 2011.* ***27****(12): p. 7909-7916.*

25. *Pang, S., Kurosawa, Y., Kondo, T.et al., Decomposition of monolayer coverage on gold nanoparticles by UV/ozone treatment. Chemistry letters, 2005.* ***34****(4): p. 544-545.*

26. *Düngen, P., Prenzel, M., Van Stappen, C.et al., Investigation of different pre-treated multi-walled carbon nanotubes by Raman spectroscopy. Materials Sciences and Applications, 2017.* ***8****(8): p. 628-641.*

27. *Yang, S., Shen, C., Lu, X.et al., Preparation and electrochemistry of graphene nanosheets–multiwalled carbon nanotubes hybrid nanomaterials as Pd electrocatalyst support for formic acid oxidation. Electrochimica Acta, 2012.* ***62****: p. 242-249.*

28. *Qiu, L., Liu, F., Zhao, L.et al., Evidence of a unique electron donor− acceptor property for platinum nanoparticles as studied by XPS. Langmuir, 2006.* ***22****(10): p. 4480-4482.*

29. *Harada, M. and Kamigaito, Y., Nucleation and aggregative growth process of platinum nanoparticles studied by in situ quick XAFS spectroscopy. Langmuir, 2012.* ***28****(5): p. 2415-2428.*

30. *Krishnankutty, N. and Vannice, M.A., The effect of pretreatment on Pd/C catalysts: I. adsorption and absorption properties. Journal of catalysis, 1995.* ***155****(2): p. 312-326.*

31. *Borodko, Y., Habas, S.E., Koebel, M.et al., Probing the Interaction of Poly (vinylpyrrolidone) with Platinum Nanocrystals by UV− Raman and FTIR. The Journal of Physical Chemistry B, 2006.* ***110****(46): p. 23052-23059.*

32. *Witjens, L.C., Bitter, J., Van Dillen, A.et al., Pd L 3 edge XANES investigation of the electronic and geometric structure of Pd/Ag–H membranes. Physical Chemistry Chemical Physics, 2004.* ***6****(14): p. 3903-3906.*

33. *Tsunoyama, H., Ichikuni, N., Sakurai, H.et al., Effect of electronic structures of Au clusters stabilized by poly (N-vinyl-2-pyrrolidone) on aerobic oxidation catalysis. Journal of the American Chemical Society, 2009.* ***131****(20): p. 7086-7093.*

34. *Xian, J., Hua, Q., Jiang, Z.et al., Size-dependent interaction of the poly (N-vinyl-2-pyrrolidone) capping ligand with Pd nanocrystals. Langmuir, 2012.* ***28****(17): p. 6736-6741.*

35. *Borodko, Y., Humphrey, S.M., Tilley, T.D.et al., Charge-transfer interaction of poly (vinylpyrrolidone) with platinum and rhodium nanoparticles. The Journal of Physical Chemistry C, 2007.* ***111****(17): p. 6288-6295.*

36. *Huang, H. and Wang, X., Pd nanoparticles supported on low-defect graphene sheets: for use as high-performance electrocatalysts for formic acid and methanol oxidation. Journal of Materials Chemistry, 2012.* ***22****(42): p. 22533-22541.*

37. *Wang, Y., Alsmeyer, D.C. and McCreery, R.L., Raman spectroscopy of carbon materials: structural basis of observed spectra. Chemistry of Materials, 1990.* ***2****(5): p. 557-563.*

38. *Simmons, J., Nichols, B., Baker, S.et al., Effect of ozone oxidation on single-walled carbon nanotubes. The journal of physical chemistry B, 2006.* ***110****(14): p. 7113-7118.*

39. *Ma, R., Yoon, D., Chun, K.-Y.et al., The effects of UV/ozone treatments on the electrical transport behavior of single-walled carbon nanotube arrays. Chemical Physics Letters, 2009.* ***474****(1-3): p. 158-161.*

40. Osbeck, S., Bradley, R., Liu, C.et al., Effect of an ultraviolet/ozone treatment on the surface texture and functional groups on polyacrylonitrile carbon fibres. Carbon, 2011. ***49****(13): p. 4322-4330.*

Chapter 3

3 Controlled growth of palladium nanoparticles and the origin of enhanced electrocatalytic activity with metal-support interactions

3.1 Introduction

It is proved that the final catalytic activity of catalysts towards electrochemical catalytic reactions is highly dependent on their active surface area. Loading catalysts on supports can be an advantageous way of enhancing the mentioned demand. Supported catalysts can have higher stability in terms of agglomeration, better electric conductivity in terms of electron transfer from the catalyst to the external circuit and superior dispersion in terms of reagent to particle contact area, compared to the unsupported catalysts [1-3]. Currently, carbon supports have attracted a lot of attention due to their high surface area and electric conductivity; however, carbon corrosion is still an undeniable impediment through their utilization [4, 5]. Palladium catalyst isolation is the most prevalent result of carbon corrosion that is influencing the direct formic acid fuel cell stability. Considering the oxidation of amorphous carbon supports, substituting them with newer types of carbon substrates such as graphene or carbon nanotube which are having higher sp^2 carbon content, are coming to matter of attention [6]. In addition to all these physical effects of supports on catalysts, it is recently revealed that they can modify the catalytic behavior of catalyst through their interaction. The strong metal-support interaction (SMSI) which was first introduced in 1978, is recognized as a fruitful path for tuning the electronic structure of catalysts [7]. The metal-support interaction not only will result in higher activity but also can enhance the stability of catalysts through encapsulation.

Distinguishing the best support out of the common carbon supports is important and it can further enhance the activity of palladium. Determining a support with high conductivity, surface area, corrosion resistance, and metal support interaction is conducted in this study. Uniform palladium nanocubes were directly grown on carbon, graphene, carbon nanotube and nitrogen-doped carbon nanotube, using colloidal chemistry explained in chapter 2. As these catalysts were grown directly on carbon supports, instead of just loading on them, the MSI will be maximized. Different

characterization methods are used to find out the best support for obtaining the desired requirements.

3.2 Experimental Section

3.2.1 Material Synthesis

In order to investigate metal-support interactions, palladium nanoparticles (NPs) with controllable shape were directly grown on different carbon supports. To synthesize these cubic Pd NPs, the same synthesis procedure as the one mentioned in chapter 2 was employed and 50.0 mL of an aqueous solution containing:

Poly(vinyl pyrrolidone) (105 mg, acting as a stabilizer), ascorbic acid (60 mg), potassium bromide (600 mg, acting as capping agent), and a specific amount of the support was placed in a 100 mL vial and sonicated for an hour and then pre-heated in air under magnetic stirring at 80 °C for 10 min. Then, 3.0 mL of an aqueous solution containing Na2PdCl4 (57 mg) was added to the solution and the reaction was allowed to proceed at the same temperature for 3 h [8]. Afterward, products were collected by centrifugation and they were washed 3 times with the mixture of ethanol and water to remove excess Polyvinylpyrrolidone (PVP). The final obtained supported catalysts are shown in Figure 3-1.

3.2.2 Characterization

A wide variety of characterization methods are used to determine the features of these NPs. Fundamental and performance behavior of these catalysts is revealed utilizing Scanning Electron Microscope (SEM, Zeiss 1540XB), Transmission Electron Microscope (TEM, Phillips CM10), X-ray Powder Diffraction (XRD), Inductively coupled plasma mass spectrometry (ICP-MS), Brunauer-Emmett-Teller (BET) surface area analysis, and XAS at Canadian Light Source.

3.2.3 Electrochemical Test

Optimizing the performance of catalysts and correlating it with other influential parameters such as electronic structure is momentous. A simple electrochemical reaction on the catalyst entails different steps like reactant absorption on the surface catalyst, reduction or oxidation of reactant, and separation of product from the catalyst. All these steps can be tracked by performing

electrochemical testing and electrochemical surface active area, catalyst activity and catalyst long-time stability can be derived from that.

3.3 Results and Discussion

Following the afore-mentioned procedure for synthesizing Pd nanocube and adding an appropriate amount of carbon support in the main solution will result in some size and shape controlled NPs which are shown in Figure 3-1.

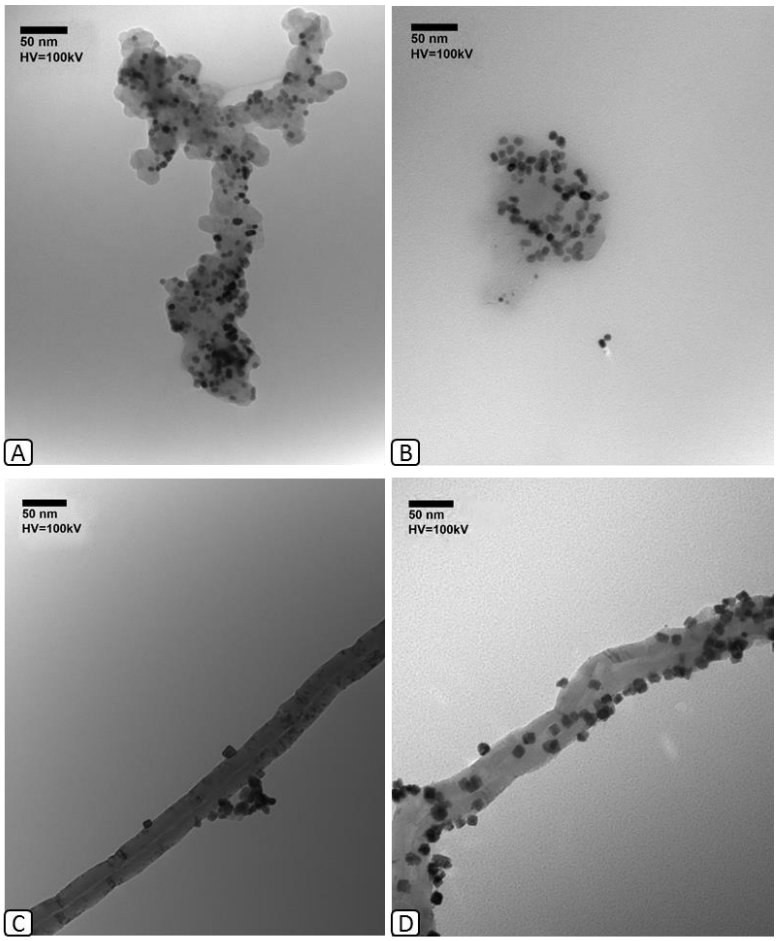

Figure 3-1 TEM images of Pd nanocubes on A) Carbon black (Vulcan XC-72B) Graphene C) CNT D) NCNT supports.

To further confirm that synthesized Pd nanocubes are mostly enclosed by cubic {100} facets, XRD data are reported in Figure 3-2. XRD data are showing three distinct diffraction peaks which are assigned to (111), (200), and (220) planes of face-centered cubic Pd. Acquired XRD results are

used to determine the average particle size of Pd catalysts, based on Scherrer equation. The calculated average particle size are shown in Table 3-1.

$$t = \frac{0.9\lambda}{\beta \cos\theta} \quad (1)$$

t is the mean size of the particles, λ is the X-ray wavelength, β is the line broadening at half the maximum intensity and θ is the Bragg angle in the Scherrer equation [9].

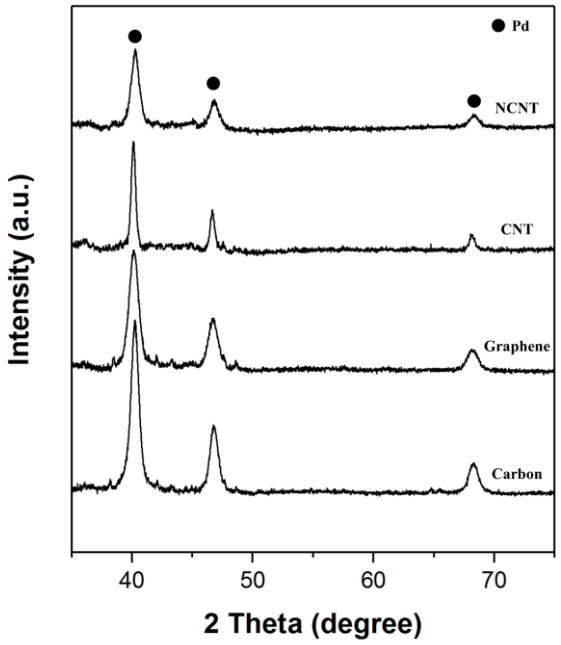

Figure 3-2 X-ray diffraction patterns of palladium catalysts grown on different carbon supports.

As the chemical composition of each sample will be imperative in their electrochemical performance, inductively coupled plasma mass spectrometry was used to find out the weight percentage of palladium loaded on carbon supports in each sample. All samples showed almost similar metal mass loading and the obtained results by ICP-MS are shown in Table 3-1.

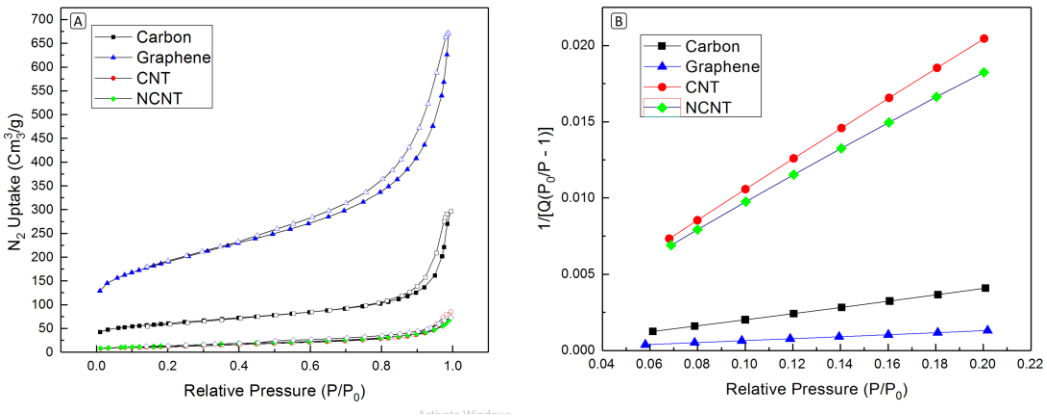

Figure 3-3 A) Nitrogen adsorption (closed symbol) and desorption (open symbol) isotherms and B) multi-point BET plots of the investigated carbon supports.

Having higher surface area can be an undeniable parameter for enhancing the dispersion of catalysts and its exposure to electrolyte during electrochemical processes [10]. Therefore, choosing a substrate with higher surface area can be influential in the synthesis procedure and can be advantageous for obtaining the desirable supported catalyst. In this study, Brunauer-Emmett-Teller (BET) method has been employed to find out the surface area of the utilized carbon supports. In order to use this method, samples were first outgassed at the temperature of 250 °C overnight and then the temperature was reduced to as low as 77 K to obtain the nitrogen adsorption-desorption isotherms. BET graph which is $1/[Q(P/P_o-1)]$ versus (P/P_o) is then plotted using the obtained adsorption data [11]. Nitrogen adsorption-desorption isotherms and multi-point BET plots are shown in Figure 3-3. The straight line in BET graph is now having a slope (S) and an intercept (Y_{Int}) which can be employed in the following equation and the outcome will be the specific surface area [12].

$$S_{BET} = \frac{0.1620\ nm^2.(6.023\times10^{23})}{(22414\ cm^3_{STP}).\left(10^{18}\frac{nm^2}{m^2}\right).(S+Y_{Int})} \qquad (2)$$

Carbon, Graphene, Carbon nanotube, and NCNT exhibit BET surface area values of 214.3, 672.1, 43.6, and 49.7 $m^2 \cdot g^{-1}$, respectively.

Considering both the carbon supports surface area and the ultimate palladium morphology, it is worth to mention that although surface area is an imperative parameter for enhancing the catalyst

dispersion, there are still some other key parameters which can influence the morphology of synthesized catalyst. In this study, carbon is having higher surface area compared to NCNT but the nitrogen defects on the surface of nanotubes and their anchoring role have been found to be more effective in dispersing the catalyst and enhancing their electrochemical performance [13, 14]. These nitrogen defects have also made NCNT have higher surface area compared to the nitrogen-free carbon nanotube.

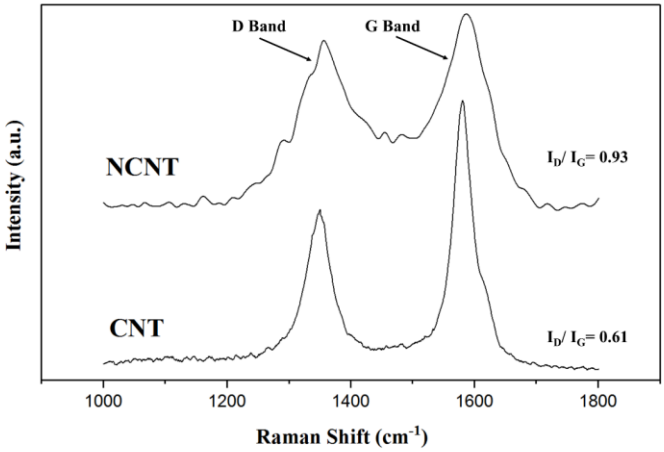

Figure 3-4 Raman spectra of carbon Nanotube before and after doping with nitrogen.

Raman spectroscopy is a powerful technique to show the graphitization and disorder of various carbon samples [15]. As it is shown in Figure 3-4, each Raman spectra show two characteristic peaks of D and G band. The first peak positioned at around 1350 cm^{-1} is D (defect) band and is showing the defects in an infinite perfect graphite structure. The second peak at around 1590 cm^{-1} corresponds to G (graphite) band, which is related to sp^2-hybridized carbon vibrations [16]. The ratio between D and G band intensities (I_D/I_G) is also an important parameter which is being used to quantify the graphitic and disorder properties of samples [17]. As shown in the Raman spectra, the intensity ratio (I_D/I_G) has increased after nitrogen doping and it is confirming the higher ratio of defects in the NCNT substrate.

It is also obvious that D and G band in CNT is being broadened and shifted to higher frequency after doping with nitrogen. The shift is mainly related to the C-C expansion and electronic structure modification by nitrogen dopants [13, 18]. The broadening is also occurring due to an increase in defects after nitrogen doping, which is introducing disorder structure and defects to the crystals.

These defects on the surface of NCNT are a big assist for anchoring Pd nanoparticles and can be fruitful for formic acid oxidation performance.

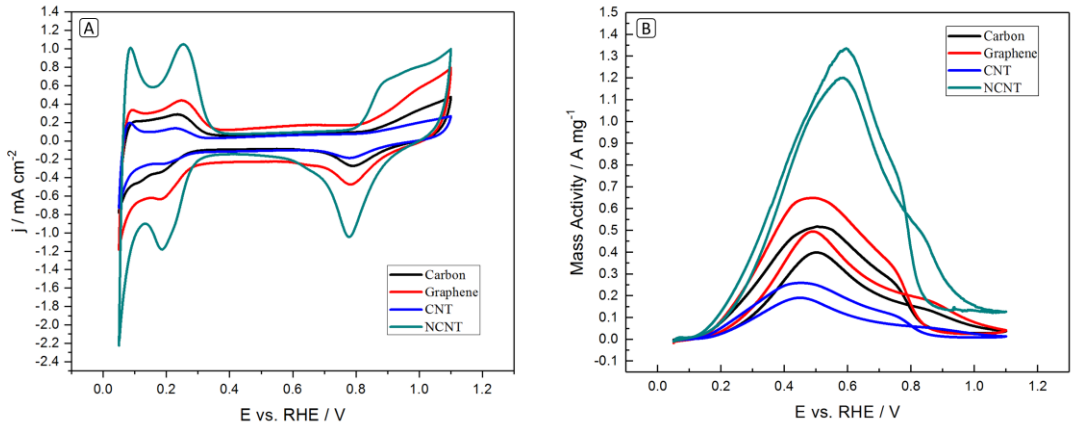

Figure 3-5 CV of supported Pd nanocubes electrode in A) 0.5 M H_2SO_4 and B) 0.5 M H_2SO_4 + 0.5 M HCOOH solution.

Cyclic Voltammograms of Pd/C, Pd/G, Pd/CNT and, Pd/NCNT catalysts in 0.5 M H_2SO_4 at a scan rate of 50 mV s^{-1} with potential ranging from 0.05 to 1.1 V are shown in Figure 3-5. Using the charge related to hydrogen adsorption peaks, ECSA of these catalysts are calculated [19]. As Pd catalysts are showing a tremendous activity toward formic acid oxidation, their activities are determined in 0.5 M H_2SO_4 containing 0.5 M HCOOH electrolyte. As potential increase from 0.05 V, an increase in the current will be observed which is indicating the initiation of HCOOH oxidation. By further increase in potential, more poisoning CO will be produced, and it will block the available surface for more oxidation. The main oxidation peaks in Figure 3-5, correspond to the oxidation of fresh HCOOH. Calculated peak current density which is relative to the utilized Pd is shown in Table 3-1.

In general, formic acid oxidation can proceed through two main mechanisms of direct and indirect pathways of dehydrogenation and dehydration. Although the final product of both pathways is CO_2, adsorbed CO intermediate in dehydration pathway, also known as poisoning route, can poison the metal surface and cease further reactions [20, 21]. CO can be adsorbed on the surface of catalyst with high affinity and can block the active sites on the metal surface and reduce their catalytic activity drastically [22].

$$HCOOH \xrightarrow[(Direct)]{Dehydrogenation} CO_2 + 2H^+ + 2e^- \quad (3)$$

$$HCOOH \xrightarrow[(Indirect)]{Dehydration} CO_{ads} + H_2O \rightarrow CO_2 + 2H^+ + 2e^- \quad (4)$$

Considering these reaction pathways, Equations 3 and 4, formic acid oxidation is proceeding through both dehydrogenation and dehydration pathways on Pd nanocubes.

In the anodic scan, the first peak at the potential of approximately 0.4 V is corresponding to dehydrogenation and the second peak which is arising at the potential of 0.7 V is ascribed to dehydration pathways. The intensities ratio of the first and second peak in anodic scan can be used to determine the dominant pathway and the higher value of this ratio is mainly an indicator of its higher activity and lower CO intermediate production. It is obvious in Figure 3-5 that Pd/NCNT is having the highest ratio for direct to indirect FAO pathways and this is confirming that this catalyst is inhibiting the formation of poisonous CO.

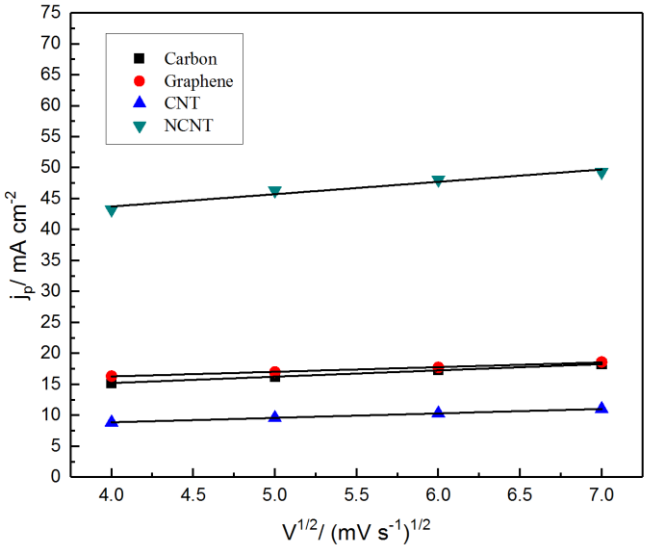

Figure 3-6 Relation of FAO peak current density of different samples with the square root of scan rates.

As it can be seen in Figure 3-6, the peak current density of different samples depends linearly on the square root of scan rate of the potential, *v*, and it is increasing with enhancing the potential. This linear relation is defining these reactions as a diffusion-controlled process and its positive slope is confirming its reversibility, which follows Randles–Sevcik formula (Equation 5) [23]. Considering the same number of *n*, *A*, C_0^* for all these catalysts, diffusion coefficient, *D*, can be obtained. The higher diffusion coefficient will confirm the existence of higher active surface sites and higher availability for oxidation on catalysts and the following equation is used to compare this important parameter.

$$i_p = (2.69 \times 10^5) n^{3/2} A D_0^{1/2} C_0^* v^{1/2} \quad (5)$$

Where *n*, *A*, C_0^* are defining electron transfer number, electrode area, and initial concentration respectively.

Using Equation 5, diffusion coefficient of supported nanocubes can be compared as follows:

$$D_{NCNT} > D_G > D_C > D_{CNT} \quad (6)$$

The higher value for diffusion coefficient of Pd/NCNT is endorsing the positive effect of nitrogen on catalytic activity of palladium nanocube and its influence on diffusion and removal of by-products and providing more active site for further reactions.

EIS is another advantageous technique which can characterize the kinetics of electrochemical reactions on the surface of catalysts and can disclose the mechanism of formic acid oxidation in our study [24]. As it is shown in Figure 3-7, EIS was done at the potential of 0.2 V_{RHE} in the frequency range of 10 mHz to 100 kHz. To discuss each part of this plot in depth, acquired data were fitted utilizing ZVIEW software and the equivalent circuit is shown as an inset in Figure 3-7. Based on the fitted data in all catalysts, the first semicircle raised at high frequency is corresponding to a resistant in parallel to a constant capacitive element. By going to lower frequencies, a straight line with a slope of 45° appears which is generally showing the Warburg diffusion resistance [25]. As it is explicit in the EIS data, all catalysts are having the same equivalent circuit, and this is confirming that all the synthesized catalysts are having the same

structure at the interface of catalyst and electrolyte and they are following the same mechanism for electrooxidation of formic acid. The diameter of the first semicircle can be used to determine the charge transfer resistance (R_{CT}) and can show the resistance of charge transfer at the electrochemical interface of catalyst and electrolyte. Other parameters such as R_S and CPE, which are shown in the equivalent circuit, are corresponding to the solution resistance and double layer capacitance respectively and all can be quantified by fitting data [26].

By having a thorough consideration of the data, the difference between diameters is vivid. Charge transfer resistance which is R_{CT} in the equivalent circuit is smaller in the Pd/NCNT and this lower resistance, which is derived from smaller diameter of a semicircle, has made the Pd/NCNT catalyst showing the highest catalytic activity towards formic acid oxidation. The larger diameter of Pd/C is also showing the difficulty in charge transferring and is confirming the obstacles in formic acid oxidation on its surface. The fitted parameters of these samples are all presented in Table 3-1. Therefore, NCNT with its lower charge transfer resistance is having higher electrical conductivity for electrochemical reactions on its surface and this correlation can be used for comparing other catalysts as well.

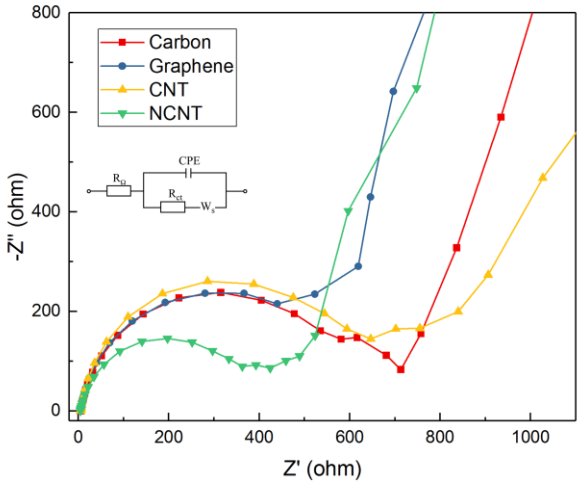

Figure 3-7 Nyquist plots of supported Pd catalysts at 0.2 V (vs. RHE) in 0.5 M H_2SO_4 + 0.5 M HCOOH solution. The inset is showing the equivalent circuit used to fit the impedance spectra.

Corrosion of carbon materials is the main obstacle in their utilization as support for catalysts. Therefore, chronoamperometry (i-t curve) is used in this study to evaluate the stability of these catalysts. As it is obvious in Figure 3-8, electrodes were kept at a constant potential of 0.4 V for 5000 s and the effect of intermediate species such as CO on the catalyst and long-term exposure of Carbon to the corrosive environment is investigated. Each catalyst has kept a specific amount of its initial current density after 5000s of testing and the gradual decrease in current density is confirming the poisoning effects of intermediates on all catalysts. The initial point for this test is considered as 10 s, due to the double layer charging. The stability performances are shown in Table 3-1. NCNT and Carbon showed to have the highest and lowest resistant to the stability test, respectively.

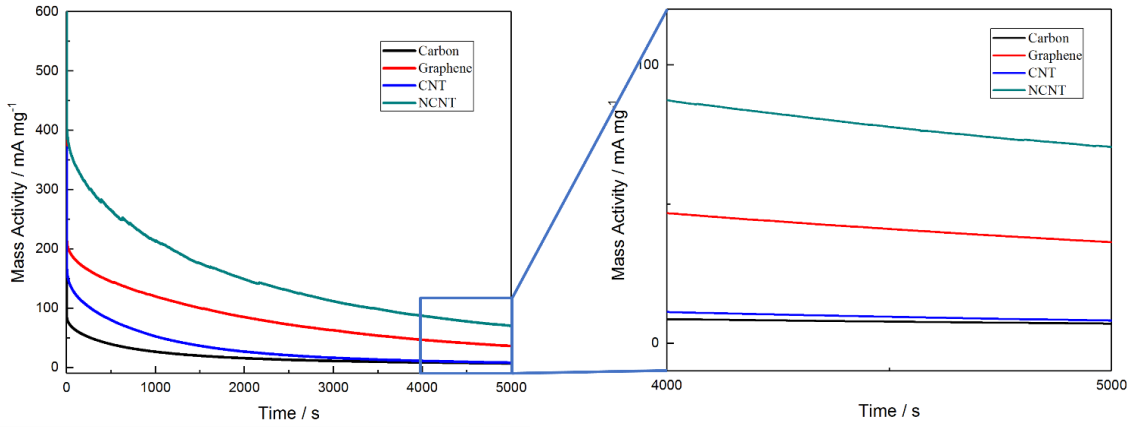

Figure 3-8 Chronoamperometric curves of Pd nanocubes, supported with different carbon materials, at 0.4 V.

One of the main reasons of conducting this research was determining the SMSI effect on the electronic structure of catalysts. An advantageous way of determining the interaction between two material and thoroughly determining the concept of interaction is X-ray Photoelectron Spectroscopy (XPS). The XPS profile of Pd nanocubes containing $3d_{3/2}$ and $3d_{5/2}$ electrons of palladium are shown in Figure 3-9 and they are calibrated via alignment of the C (sp^2) peak position in the C_{1s} spectrum to its reference value of 284.8 eV. The peak positions of these spectra are all mentioned in Table 3-2. Peaks, Pd_1 and Pd_2 represent slightly different Pd site on the surface and Pd_3, accounts for the asymmetry arising from many-body effects arising from a narrow unoccupied d band just above the Fermi level. It is obvious that Pd/NCNT is experiencing a shift

to lower energies compared to other samples, indicating more noticeable charge redistribution at the Pd site with the NCNT substrate [27, 28]. This is confirming that Pd gains d charge which has a larger coulombic interaction, F(3d, 4d) than F(3d, 5s), resulting in a shift in the binding energy. The two Pd_1 and Pd_2 peaks can be also assigned to metallic Pd, on the surface of nanoparticle and in its bulk. Due to the approximately large size of particles, the bulk is not experiencing the same interaction as surface and carbon-metal interaction on the near surface is producing two peaks for the nanoparticles.

To determine the origin of the shift in Pd/NCNT, N_{1s} XPS spectra of NCNT before and after growing Pd is acquired. As it is obvious in Figure 3-9, the N_{1s} spectra can be assigned to five components of N_P (pyridinic N), N_{Pyr} (pyrrolic N), N_G (graphitic N), N_{OX} (N-oxides), and N_{ads} (chemisorbed N) from low to high energies [29]. Shift to higher energies after growing palladium NPs is obvious in N_{1s} spectra and it is confirming that there is an electron transfer from nitrogen to palladium.

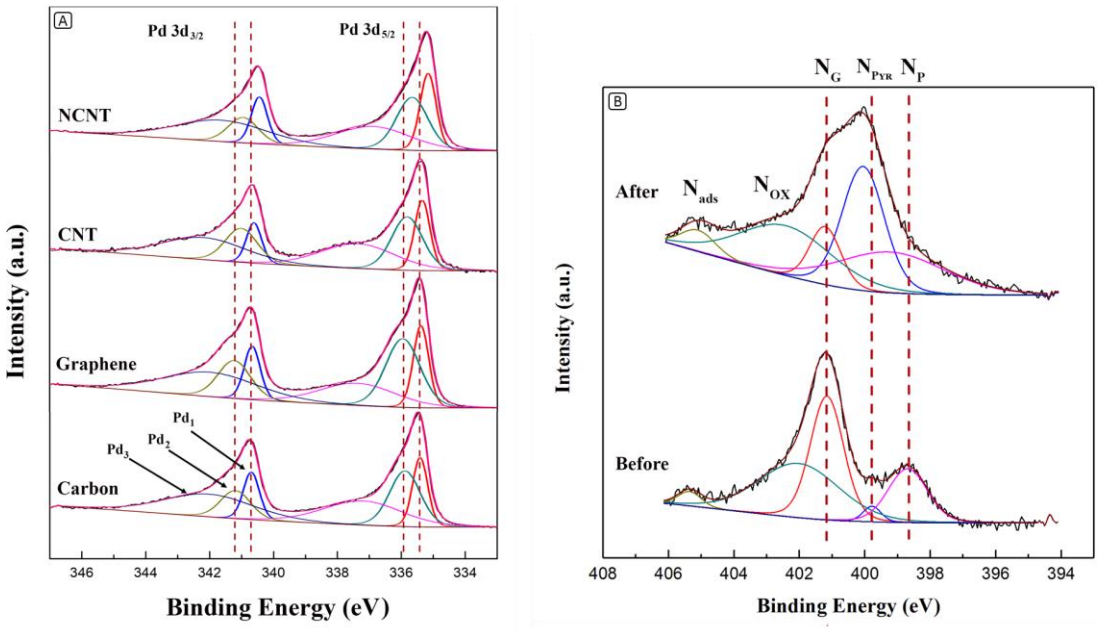

Figure 3-9 XPS spectra of A) the Pd 3d region of the Pd nanocubes on different carbon supports and B) the N 1s region of NCNT before and after the catalyst growth.

Confirming XPS results and tracking the electronic structure of these catalysts can be easily conducted using XAS. XANES data of L_3-edge, which is collected in TEY mode in this study and

is more surface sensitive, are presented in Figure 3-10. Comparing their whitelines, the first sharp peak at the edge arising from $2p_{3/2}$ to $4d_{5/2,3/2}$ transition, which probes the unoccupied densities of states of Pd 4d character at the Fermi level, will show their interaction with carbon supports and change of their d-band vacancies above the Fermi level [30, 31, 32].

As it is shown in Figure 3-10, the whiteline corresponding to palladium NPs grown on NCNT is having the lowest intensity and this is further confirming the electron transfer from nitrogen to palladium. By having an electron transfer from nitrogen to the catalyst, there will be lower d holes upper Fermi level so there will be lower vacancies for excited electrons and this will lower the whiteline intensity [28,30]. The trend in whiteline intensity is showing the same result as energy shifts in XPS data, as the highest shift to lower energies is having the lowest whiteline intensity and vice versa. A schematic displayed in Figure 3-11 is showing the interaction of palladium with nitrogen sites in NCNT. This interaction not only is assisting in anchoring Pd NPs on NCNT surface but also is altering palladium electronic structure by electron transfer from nitrogen sites to palladium. All these features together have made Pd/NCNT to have more active sites for formic acid oxidation and be more stable in encountering poisonous intermediates.

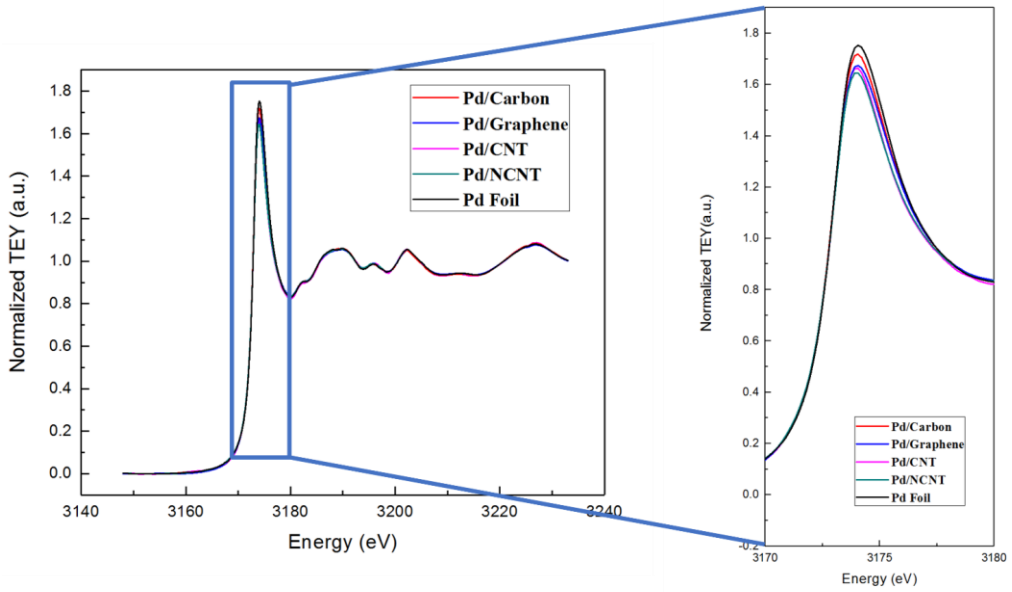

Figure 3-10 X-ray absorption near-edge spectra of Pd samples grown on different carbon supports.

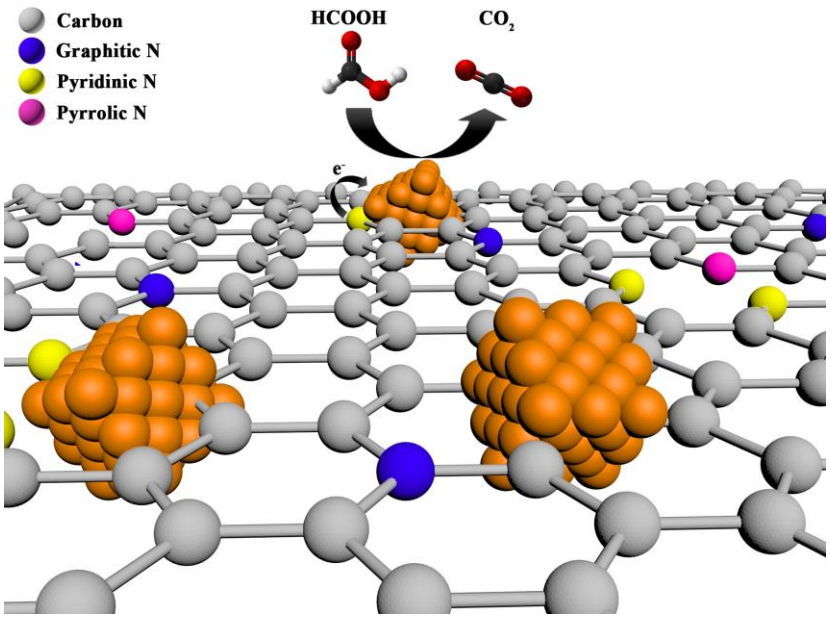

Figure 3-11 Schematic of the proposed interaction of Pd nanocubes with nitrogen sites in NCNT.

Table 3-1 Comparison of the catalytic activities for formic acid oxidation, stability, Impedance components and nanoparticle size and composition of Pd NPs on different carbon supports.

Sample	Particle Size (nm)	Palladium concentration	R_{CT} (Ω)	ECSA (m^2/g)	I_p (A mg^{-1})	E_p (mV)	$\frac{j_{t=5000\,s}}{j_{t=10\,s}}$
Pd/C	15.7	49 %	424.1	18.60	0.3992	0.50186	9.31 %
Pd/G	14.2	47 %	309.9	21.97	0.49542	0.49011	18.18 %
Pd/CNT	24.4	42 %	487.1	9.71	0.19089	0.44846	5.55 %
Pd/NCNT	15.5	46 %	250.8	42.52	1.20021	0.57663	18.62 %

Table 3-2 X-ray photoelectron spectroscopy (XPS) peak positions of Pd on different carbon supports.

Sample	Pd_1 (eV)	Pd_2 (eV)
Pd/C	335.41	335.88
Pd/G	335.39	335.96
Pd/CNT	335.37	335.84
Pd/NCNT	335.16	335.66

3.4 Conclusions

Cubic palladium catalysts were directly grown on different carbon supports and the influence of metal support interaction on performance and electronic structure of Pd was determined. It is apparent that doping carbon nanotube with nitrogen will not only enhance the catalyst distribution by generating surface defects on CNT but also enhance the catalytic activity by tuning electronic structure through electron transfer with Pd. An interesting point in XPS data is observing two slightly different chemical sites of Pd. As these catalysts are grown on carbon supports, the carbon-palladium interactions have made this shift and the reason for the second peak is that the synthesized catalysts are approximately large so the part that does not have any interaction with support will not experience that interaction and shift. Normal carbon nanotube did not show a good activity, as it has low surface area and lacks active sites (defects), and most of the catalysts will agglomerate on each other. Nitrogen and nitrogen induced defects on the surface of carbon nanotubes have helped to anchor the nanoparticles and this will cease the nanoparticle detachment which will be necessary in enhancing the stability of catalysts. It is also determined that π sites on graphene structure have helped to have a strong interaction with nanoparticles and this has increased the electrochemical performance of graphene compared to carbon.

3.5 References

1. *Yang, S., Zhang, X., Mi, H.et al., Pd nanoparticles supported on functionalized multi-walled carbon nanotubes (MWCNTs) and electrooxidation for formic acid. Journal of Power Sources, 2008.* ***175****(1): p. 26-32.*

2. *Qin, Y.-H., Jia, Y.-B., Jiang, Y.et al., Controllable synthesis of carbon nanofiber supported Pd catalyst for formic acid electrooxidation. international journal of hydrogen energy, 2012.* ***37****(9): p. 7373-7377.*

3. *Zhu, Y., Kang, Y., Zou, Z.et al., Facile preparation of carbon-supported Pd nanoparticles for electrocatalytic oxidation of formic acid. Fuel Cells Bulletin, 2008.* ***2008****(7): p. 12-15.*

4. *Chen, X., Wu, G., Chen, J.et al., Synthesis of "clean" and well-dispersive Pd nanoparticles with excellent electrocatalytic property on graphene oxide. Journal of the American Chemical Society, 2011.* ***133****(11): p. 3693-3695.*

5. *Huang, S.-Y., Ganesan, P. and Popov, B.N., Titania supported platinum catalyst with high electrocatalytic activity and stability for polymer electrolyte membrane fuel cell. Applied Catalysis B: Environmental, 2011.* ***102****(1-2): p. 71-77.*

6. *Shih, C.-J., Vijayaraghavan, A., Krishnan, R.et al., Bi-and trilayer graphene solutions. Nature Nanotechnology, 2011.* ***6****(7): p. 439.*

7. *Tauster, S. and Fung, S., Strong metal-support interactions: occurrence among the binary oxides of groups IIA–VB. Journal of Catalysis, 1978.* ***55****(1): p. 29-35.*

8. *Park, J., Zhang, L., Choi, S.-I.et al., Atomic layer-by-layer deposition of platinum on palladium octahedra for enhanced catalysts toward the oxygen reduction reaction. ACS nano, 2015.* ***9****(3): p. 2635-2647.*

9. *Jiang, L., Hsu, A., Chu, D.et al., Size-dependent activity of palladium nanoparticles for oxygen electroreduction in alkaline solutions. Journal of the Electrochemical Society, 2009.* ***156****(5): p. B643-B649.*

10. *Wang, Q., Wang, Y., Guo, P.et al., Formic acid-assisted synthesis of palladium nanocrystals and their electrocatalytic properties. Langmuir, 2014.* ***30****(1): p. 440-446.*

11. *Mori, K., Miyawaki, K. and Yamashita, H., Ru and Ru–Ni nanoparticles on TiO2 support as extremely active catalysts for hydrogen production from ammonia–borane. Acs Catalysis, 2016.* ***6****(5): p. 3128-3135.*

12. *Sevilla, M., Ferrero, G.A., Diez, N.et al., One-step synthesis of ultra-high surface area nanoporous carbons and their application for electrochemical energy storage. Carbon, 2018.* ***131****: p. 193-200.*

13. *Wei, Y., Zhang, X., Luo, Z.et al., Nitrogen-doped carbon nanotube-supported Pd catalyst for improved electrocatalytic performance toward ethanol electrooxidation. Nano-micro letters, 2017.* ***9****(3): p. 28.*

14. *Chen, Y., Wang, J., Liu, H.et al., Nitrogen Doping Effects on Carbon Nanotubes and the Origin of the Enhanced Electrocatalytic Activity of Supported Pt for Proton-Exchange Membrane Fuel Cells. The Journal of Physical Chemistry C, 2011.* ***115****(9): p. 3769-3776.*

15. *Wang, Y., Alsmeyer, D.C. and McCreery, R.L., Raman spectroscopy of carbon materials: structural basis of observed spectra. Chemistry of Materials, 1990.* ***2****(5): p. 557-563.*

16. *Molina-Duarte, J., Espinosa-Vega, L., Rodríguez, A.et al., Raman spectra of single walled carbon nanotubes at high temperatures: pretreating samples in a nitrogen atmosphere improves their thermal stability in air. Physical Chemistry Chemical Physics, 2017.* ***19****(10): p. 7215-7227.*

17. *Wei, Z., Pan, R., Hou, Y.et al., Graphene-supported Pd catalyst for highly selective hydrogenation of resorcinol to 1, 3-cyclohexanedione through giant π-conjugate interactions. Scientific reports, 2015.* ***5****: p. 15664.*

18. *Chernyak, S.A., Ivanov, A.S., Stolbov, D.N.et al., N-doping and oxidation of carbon nanotubes and jellyfish-like graphene nanoflakes through the prism of Raman spectroscopy. Applied Surface Science, 2019.* ***488****: p. 51-60.*

19. *Yang, S., Shen, C., Tian, Y.et al., Synthesis of cubic and spherical Pd nanoparticles on graphene and their electrocatalytic performance in the oxidation of formic acid. Nanoscale, 2014.* ***6****(21): p. 13154-13162.*

20. *Cuesta, A., Cabello, G., Osawa, M.et al., Mechanism of the Electrocatalytic Oxidation of Formic Acid on Metals. ACS Catalysis, 2012.* ***2****(5): p. 728-738.*

21. *Kang, Y. and Murray, C.B., Formic Acid Oxidation, in Encyclopedia of Applied Electrochemistry, G. Kreysa, K.-i. Ota and R.F. Savinell, Editors. 2014, Springer New York: New York, NY. p. 895-901.*

22. *Jiang, K., Zhang, H.-X., Zou, S.et al., Electrocatalysis of formic acid on palladium and platinum surfaces: from fundamental mechanisms to fuel cell applications. Physical Chemistry Chemical Physics, 2014.* ***16****(38): p. 20360-20376.*

23. *Yang, S., Shen, C., Lu, X.et al., Preparation and electrochemistry of graphene nanosheets–multiwalled carbon nanotubes hybrid nanomaterials as Pd electrocatalyst support for formic acid oxidation. Electrochimica Acta, 2012.* ***62****: p. 242-249.*

24. *Huang, H. and Wang, X., Pd nanoparticles supported on low-defect graphene sheets: for use as high-performance electrocatalysts for formic acid and methanol oxidation. Journal of Materials Chemistry, 2012.* ***22****(42): p. 22533-22541.*

25. *Wang, Y., He, Q., Wei, H.et al., Optimal Electrocatalytic Pd/MWNTs nanocatalysts toward formic acid oxidation. Electrochimica acta, 2015.* ***184****: p. 452-465.*

26. *Qu, W.-L., Wang, Z.-B., Jiang, Z.-Z.et al., Investigation on performance of Pd/Al 2 O 3–C catalyst synthesized by microwave assisted polyol process for electrooxidation of formic acid. Rsc Advances, 2012.* ***2****(1): p. 344-350.*

27. *He, Z., Dong, B., Wang, W.et al., Elucidating Interaction between Palladium and N-Doped Carbon Nanotubes: Effect of Electronic Property on Activity for Nitrobenzene Hydrogenation. ACS Catalysis, 2019.* ***9****(4): p. 2893-2901.*

28. *Jackson, C., Smith, G.T., Inwood, D.W.et al., Electronic metal-support interaction enhanced oxygen reduction activity and stability of boron carbide supported platinum. Nature Communications, 2017.* ***8****: p. 15802.*

29. *Zhang, L., Wang, X., Wang, R.et al., Structural evolution from metal–organic framework to hybrids of nitrogen-doped porous carbon and carbon nanotubes for enhanced oxygen reduction activity. Chemistry of Materials, 2015.* ***27****(22): p. 7610-7618.*

30. *Sham, T.K., L-edge x-ray-absorption spectra of PdA13 and PdClq. A study of charge redistribution in compounds of an element with a nearly full 4d shell . Physical Review B, 1985, 31(4): p. 1903-1908.*

31. *Zhou, J., Zhou, X., Sun, X.et al., Interaction between Pt nanoparticles and carbon nanotubes–An X-ray absorption near edge structures (XANES) study. Chemical physics letters, 2007.* ***437****(4-6): p. 229-232..*

32. *Tanaka, T., Yamamoto, T., Kohno, Y.et al., Application of XANES spectra to supported catalysts. Japanese Journal of Applied Physics, 1999.* ***38****(S1): p. 30.*

Chapter 4

4 Co-doped Pd@Pt core-shell nanoparticles: correlation between the electronic structure and the catalytic activity of the catalysts in ORR

4.1 Introduction

Platinum (Pt) is a critical catalytic component used in polymer electrolyte membrane fuel cells (PEMFCs). However, its low abundance, limited supply, and increasing demand have limited the commercial application of this metal. One of the most recent ways to satisfy the mentioned demands is to utilize Pt-based bimetallic nanoparticles. Using Pt metal as the shell material of the catalyst not only increases the surface area but also make an interfacial interaction between the core metal and platinum, which will result in enhanced catalytic activity. Octahedral Pd@Pt nanoparticles with controllable Pt shell has recently shown to have greatly enhanced activity and durability compared to the commercial Pt/C. In this chapter, we describe a specific project in which Pd@Pt nanoparticle will be first synthesized by loading platinum on octahedral palladium NP, which was completely studied in chapter 2. Then the core-shell structure will be surface doped with cobalt to further boost its durability and activity. In this way, we will be capable of combining the two main strategies of synthesizing an efficient catalyst, alloying and core-shell structure. Characterizing the synthesized catalyst with XANES and EXAFS at Pt L_3-edge and cobalt K-edges, together with performance test, have revealed information about the effect of the dopants on the catalytic activity of catalysts. Results about the local and electronic structure of the catalyst are correlated with electrocatalytic activity of the electrocatalyst to optimize performance. Cobalt has been found to be simultaneously efficient in enhancing catalytic activity and reducing the platinum content in the catalyst.

4.2 Experimental Section

4.2.1 Methodology

The difference between the obtained NPs will be investigated through ICP-MS, XRD, XAS, TEM, SEM, HRTEM, and XPS, which will provide helpful information such as crystallinity, local and electronic structure, morphology, and composition of these bimetallic nanoparticles. These techniques have been described in chapter 1 and throughout chapters 2 and 3 as appropriate. Fundamental information about these NPs, their morphology, structure and electronic properties, will be correlated with their catalytic activity for ORR.

4.2.2 Material Synthesis

As properties of NPs highly depend on their size and shape, a previous explained colloidal chemistry method was used in this study to synthesize Pd nanoparticles with tunable size and shape [1]. To prepare the core-shell catalysts, the first step is to synthesize the Pd seed with different morphologies. To synthesize cubic Pd NP, as mentioned in chapter 2, 8.0 mL of an aqueous solution containing: Poly(vinyl pyrrolidone) (PVP, 105 mg, acting as a stabilizer), ascorbic acid (AA, 60 mg) and, potassium bromide (KBr, 600 mg, acting as capping agent) was placed in a 20 mL vial and pre-heated for 10 min at the temperature of 80 °C. Then, 3.0 mL of an aqueous solution containing Na2PdCl4 (57 mg) was injected to the solution and the reaction was proceeded for another 3 h, at the same temperature [2]. Afterward, products were collected by centrifugation and they were washed at least 3 times with the mixture of ethanol and water for PVP elimination. The obtained cleaned product was finally dispersed in 10 ml of water. SEM figure of cubic Pd NPs is shown in Figure 4-1-A.

To correlate the NP morphology with their performance, Pd octahedral NPs are synthesized as well. The procedure was almost the same and Pd NCs were used as seeds for octahedral ones. Heating the following solution: poly(vinyl pyrrolidone) (105 mg), formaldehyde (0.1 ml), pure water (8 ml), cubic seeds (0.3 ml) at the temperature of 60 °C for 5 min and adding 2.9 mL of an aqueous solution containing Na_2PdCl_4 (29 mg), will result in octahedral Pd NPs after 3 hours of reaction proceeding. It is necessary to wash samples with a mixture of water and ethanol for at least three times [3]. The final product was dispersed in EG. SEM images of the as-synthesized cubic and octahedral palladium NPs are shown in Figure 4-1.

Then Pd seeds were used to synthesize octahedral Pd@Pt core-shell nanoparticle. In order to have a smooth platinum shell covering the palladium core, water-based system is utilized [4]. Higher amount of acquired sample and significant lower reaction time, are the principal privileges of this water-based procedure over the other common methods [5]. To deposit four layers of Pt, 35 mg of PVP, 60 mg of citric acid and 10 mL of octahedral Pd (acquired in the first step) were pre-heated for 10 min at the temperature of 95°C. After heating the solution for the mentioned time, 3 mL of K_2PtCl_4 (1.4 mg mL^{-1}) was added in one pot to the solution and the reaction was proceeded for a whole day under magnetic stirring. The samples were collected using a centrifuge and there were further doped with Co to determine its direct influence in ORR kinetics. Doping was done by dispersing the core-shell NPs and dopant precursor in DMF and heating the solution for 48 hours at 170 °C [6]. A schematic of the synthesis procedure is shown in Figure 4-2. Final doped NPs were then centrifuged, washed and loaded on carbon black to investigate on their electrochemical behavior. Using inductively coupled plasma mass spectrometry (ICP-MS), the metal loading (Pd+Pt) on carbon black was attempted to be 20%.

4.3 Results and Discussion

Depletion of petroleum-based energy resources and the severe climate change have made fuel cell technologies a reliable alternative for the current power sources [7, 8]. However, the necessity of using platinum-based catalysts and the sluggish kinetics of cathodic reactions in PEM fuel cells are still an obstacle in their largescale commercialization [9]. To overcome these challenges, surface active area and specific activity of the catalysts should be enhanced and this can be achieved through three main strategies. The first strategy would be tuning the Pt d-band center of catalysts, by alloying it with other 3d transition metal such as Ni, Co or Fe [10]. The second way of enhancing ORR activity of platinum would be hindering its shape to some specific facets [11]. In both cases, Pt d-band center will be downshifted and this will end in reduced oxygen binding energy on platinum [12]. It is proved by Stamenkovic et al. that d-band center will have an optimum value and the highest specific activity is following a volcano plot in relation to oxygen binding energy [13, 14]. The third strategy is reducing the platinum loading and enhancing its overall activity by coating a thin layer of platinum on a less-expensive core [15-17]. Although this core-shell structure will have the exact same surface active area as the same size pure platinum nanoparticle, its mass activity can be elevated due to the lower platinum usage. To maximize

platinum usage and activity, all these three strategies are combined together and a shape-controlled Pd@Pt-Co is synthesized in this study. The overall schematic of the obtained catalyst is shown in Figure 4-2 and the required steps in synthesizing these shape-controlled nanoparticles are shown as well.

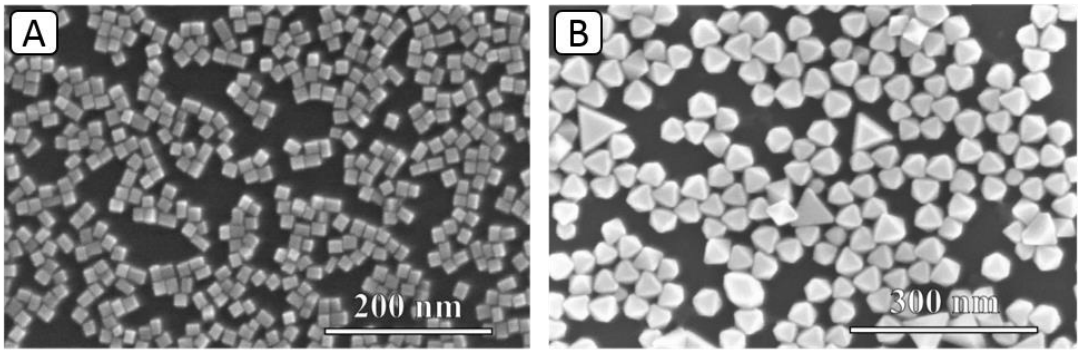

Figure 4-1 SEM images of A) Pd nanocubes and B) octahedrons that were used as seed for Pd@Pt core-shell synthesis.

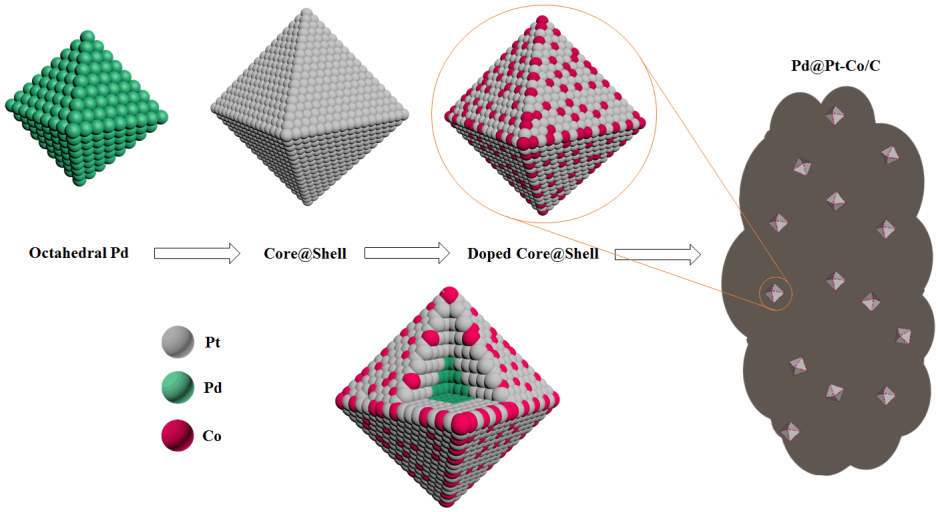

Figure 4-2 Snapshot of the whole particle, showing the schematic illustration of the synthesis procedure of Pd@Pt-Co nanoparticles which can be divided to three main steps.

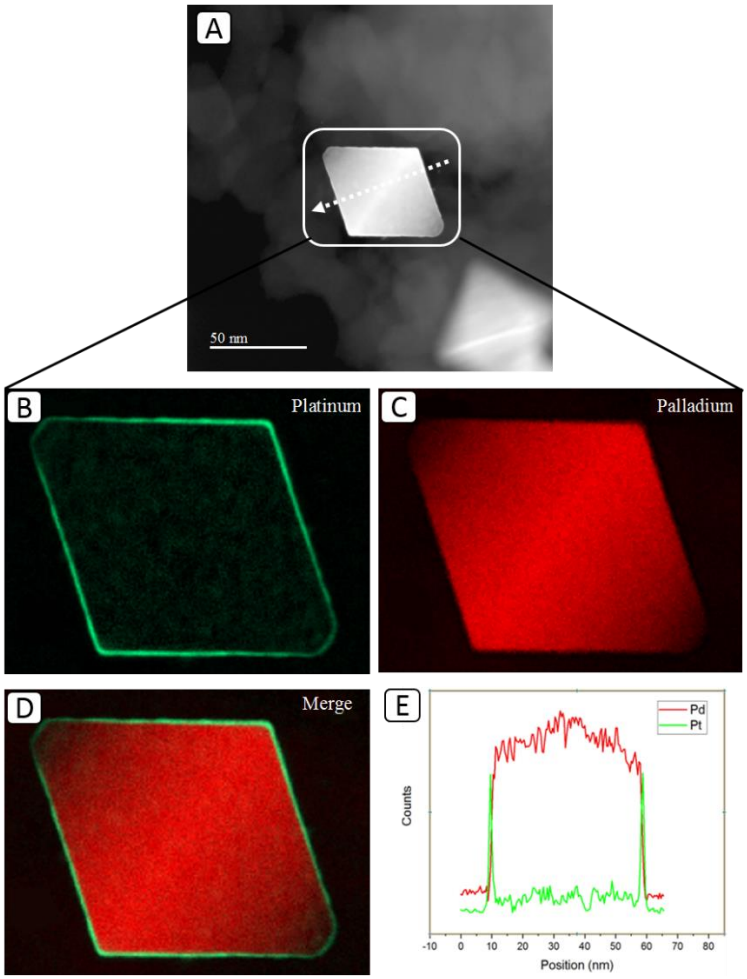

Figure 4-3 (A-D) HAADF STEM image and EDX composition maps of Octahedral-shaped Pd@Pt nanoparticle. E) Elemental line-scanning profiles along the direction marked by a white line in "A".

High-angle annular dark-field (HAADF) scanning transmission electron microscopy (STEM) was used to characterize and study a single nanoparticle of Pd@Pt core-shell nanoparticle. It is shown in Figure 4-3 that core-shell structure is completely obtained and the contrast difference between Pd and Pt, which is arising from their different atomic number, is endorsing Pt loading on palladium core. It is also shown in both Figure 4-3 and Figure 4-4 that palladium is still preserving its octahedral shape after following the other required synthesis steps and even by loading four layers of a thin shell, either Pt or Pt-Co, the whole particle is still having {111} facets on the side faces and {100} facets on the rounded corners. STEM energy-dispersive X-ray (STEM-EDX) elemental mapping is also shown in Figure 4-3B-E, confirming the existence of Pd in the core and

its coverage by a dense and smooth shell of Pt. Cobalt signal in STEM energy-dispersive X-ray (STEM-EDX) elemental mapping of Figure 4-4 also confirms the successful doping method of Pd@Pt and its existence in the surface of nanoparticle. Elemental line scanning profiles in Figure 4-3 and Figure 4-4 are also showing the distribution of platinum, cobalt, and palladium in a single nanoparticle.

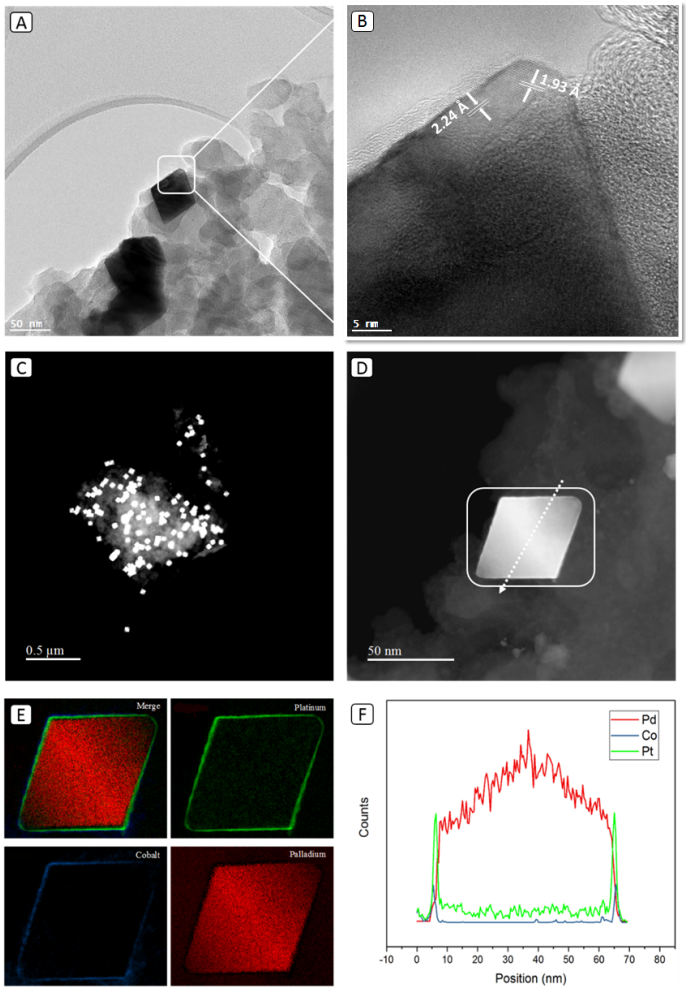

Figure 4-4 (A, B) Bright-field TEM image of octahedral Pd@Pt-Co core-shell nanocrystal C) The typical low-resolution STEM image of the octahedral cobalt doped Pd-Pt nanocrystals D) HAADF-STEM image of a single Pd@Pt-Co nanoparticle E) STEM-EDX elemental mapping images of Pd, Pt and Co and the merged image F) Elemental line-scanning profiles along the direction marked by a white line in "D".

Elemental mapping and line-scanning, presented in Figure 4-4, confirms the existence of platinum and cobalt just in the shell and the palladium core within this dense shell. The sharp peaks at the sides of Elemental line-scanning profiles are showing the existence of platinum shell, with the thickness of 0.8 nm which is equivalent to 4 atomic layers of Pt, on Pd core. The line scanning is also showing the less proportion of cobalt compared to platinum in the shell, which is in good consistency with the nanoparticle composition obtained using ICP-MS. As it is specified in Figure 4-4-B, two lattice spacings of 2.24 Å and 1.93 Å, corresponding to {111} and {200} planes, can be determined. These are confirming that incorporation of cobalt, with smaller atomic radius, in the platinum structure has shrunk the lattice of platinum compared to the pure Pt.

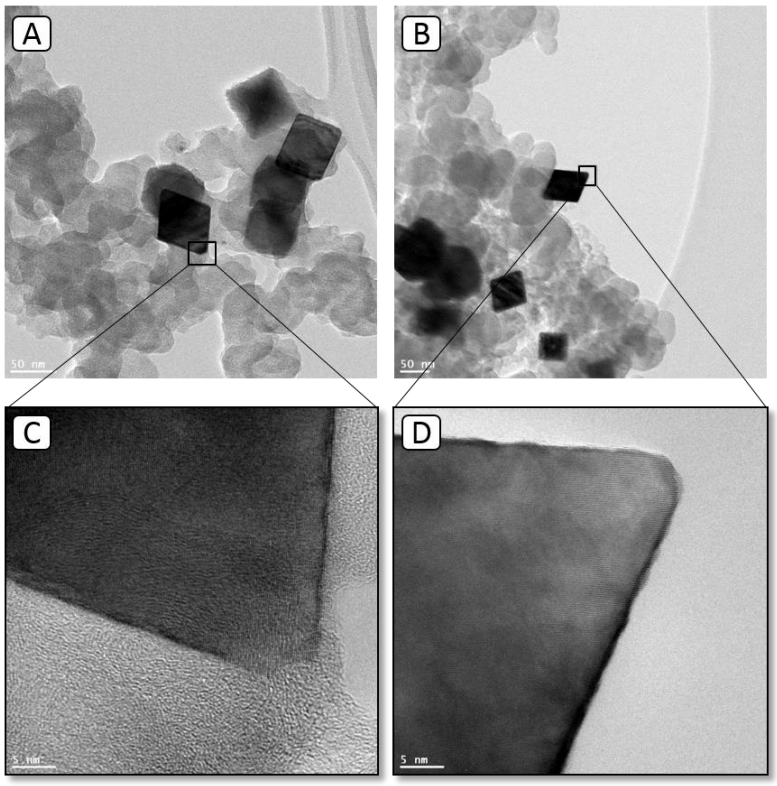

Figure 4-5 HR-TEM image of the octahedral Pd@Pt core-shell nanoparticles before (A, C) and after (B, D) doping with cobalt.

High-resolution transmission electron microscopy (HRTEM) images of a doped and undoped Pd@Pt nanoparticle are presented in Figure 4-5. It is shown that these carbon-supported

nanoparticles are consisted of single-crystal structure which has platinum as a shell covering palladium core.

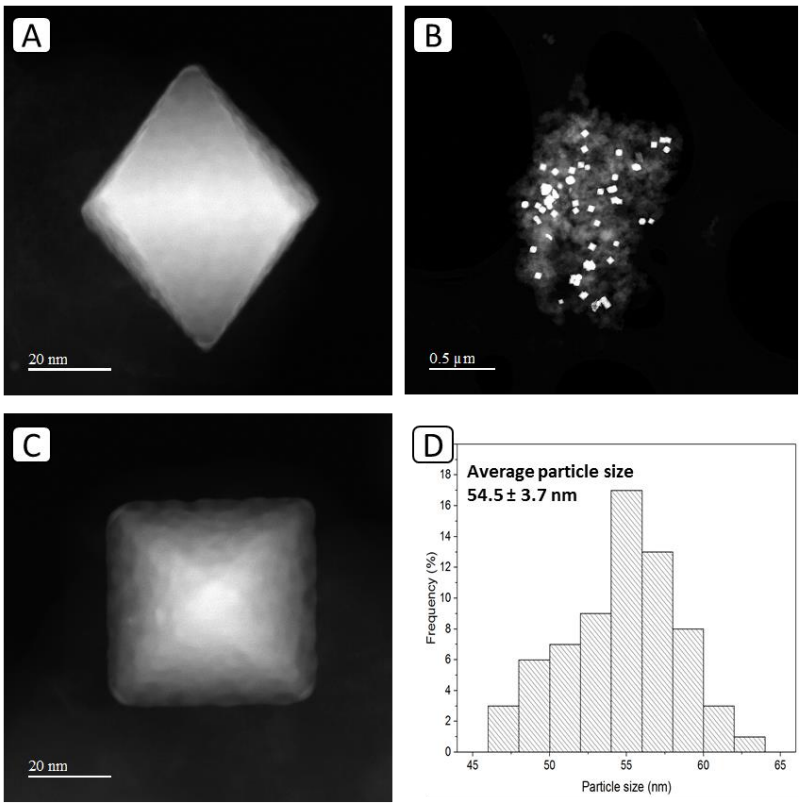

Figure 4-6 (A, C) HR-TEM image of the front and top view of the Pd@Pt octahedra nanocrystal. (B, D) The typical low-resolution STEM image of the Pd-Pt nanocrystals and their particle size distribution histogram.

Cobalt doped Pd@Pt were loaded on carbon black for further electrochemical characterizations and the supported nanoparticles are shown in Figure 4-6. It is obvious that these nanoparticles, which are having an average edge length of 54.5 ± 3.7 nm, are uniformly distributed on the support. As it is shown in Figure 4-6, the side and top view of the Pd@Pt-Co nanoparticle are further confirming the formation of octahedral shape.

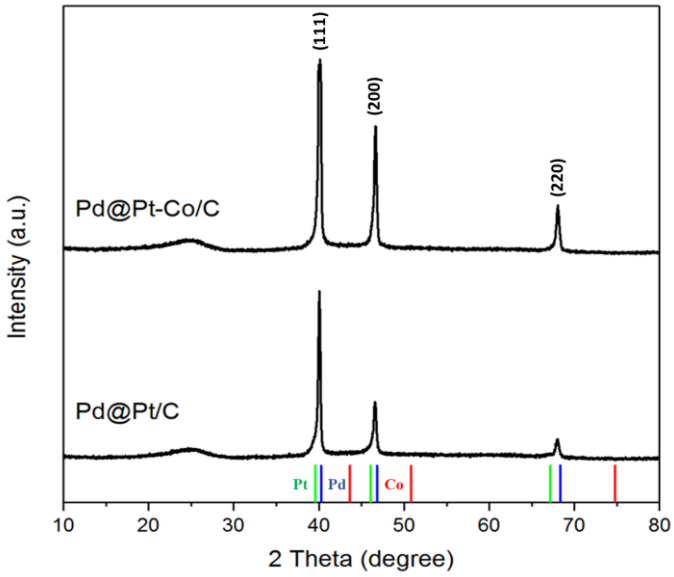

Figure 4-7 XRD spectra of Pd@Pt/C and Pd@Pt-Co/C octahedra.

The morphology of the Pd@Pt-Co/C powder was further characterized using X-ray diffraction (XRD). As presented in XRD patterns of core-shell nanoparticles before and after doping, all peaks can be assigned to face-centered cubic (f.c.c) structure [18]. Lattice structure information was also acquired via XRD analysis. Compared to pure platinum, the diffractions from both samples are shifted to higher 2θ angles due to the decreased lattice constant of the Pd@Pt core-shell NP both before and after doping with Co. The positive shift is attributed to the smaller radius of both Pd and Co compared to platinum and is supported by Vegard's law calculations [19, 20]. Bragg's law can be also employed to calculate the d-spacing and lattice parameter of these two samples [21]. Using Equation 1, Bragg's law, can help to obtain the quantitative parameters shown in Table 4-1.

$$\boldsymbol{\lambda = 2d \sin \theta} \qquad (1)$$

Where λ is the wavelength of incident X-ray (0.154nm), d is the distance between two adjacent planes of atoms, and Θ is the diffraction angle.

All these together are confirming the contraction in platinum structure due to Pd and Co influence.

Table 4-1 Summary of XRD results regarding (111) facet.

Catalyst	Lattice Parameter (nm)	d-spacing (Å)	Relative $\varepsilon_{microstrain}$ compared to Pt/C (%)
Pd@Pt	3.897	2.25	0.63
Pd@Pt-Co	3.879	2.24	1.08

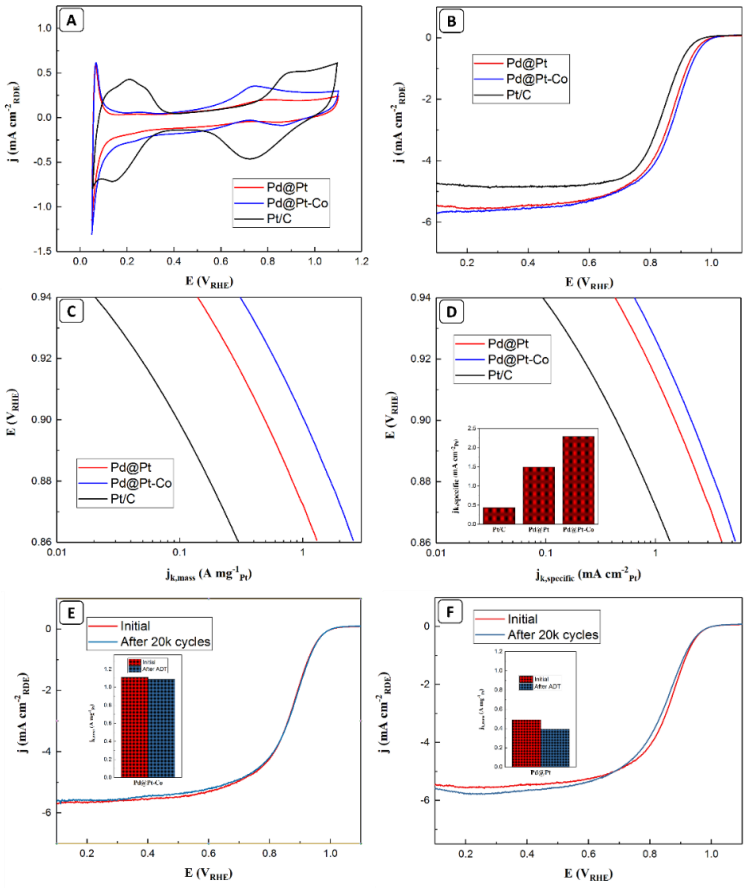

Figure 4-8 A) CVs and B) ORR polarization curves for the Pd@Pt/C and cobalt doped Pd@Pt/C catalysts. The current densities (j) were normalized against the geometric area of RDE (0.196 cm^2). C) Mass and D) Specific activities given as kinetic current densities (j_k) normalized against the mass of Pt and the ECSA of the catalyst, respectively. (Inset is showing the specific activity of the two catalysts at 0.9 V_{RHE}.). (E, F) linear sweep voltammetry of Pd@Pt-Co (E) and Pd@Pt (F) catalysts before and after 20,000 cycles between 0.6−1.0 V_{RHE} in O_2 saturated 0.1 M $HClO_4$ electrolyte. (Insets are showing the mass activity (at 0.9 V_{RHE}) of the catalysts before and after the accelerated durability tests.

To determine the kinetics of the ORR on the Pd@Pt electrocatalyst before and after doping, the rotating disk electrode was utilized [22]. A working electrode was prepared by loading 20 μL of ink (3 mg Pd@Pt/C + 1 mL DI water + 1 mL 2-propanol + 20 μL Nafion) on the glassy carbon rotating disk electrode. The first step was cycling the nanoparticles in the potential range of 0.05-1.1 V_{RHE} in N_2 saturated 0.1 M $HClO_4$. This cycling was continued until a constant CV was obtained and the surface of the catalyst was completely cleaned and stabilized [23]. By integrating the H_{UPD} region, charge corresponding to the hydrogen adsorption/desorption on platinum surface will be acquired. Using ECSA formula shown in Equation 2 and assuming 210 μC/cm^2 as a charge related to the full hydrogen coverage of Pt, electrochemical surface active area of these samples were calculated [24].

$$ECSA_{Pt}(m^2 g_{Pt}^{-1}) = \left[\frac{Q_{H-adsorption}(C)}{210\ \mu C\ cm_{Pt}^{-2}\ L_{Pt}(mg_{Pt}\ cm^{-2})\ A_g(cm^2)}\right] 10^5 \qquad (2)$$

In this formula, L_{Pt} is the platinum loading on RDE, A_g is the geometric surface area of the RDE which is 0.196 cm^2 in this study, and $Q_{(H\text{-}adsorption)}$ is corresponding to the hydrogen adsorption charge.

As shown in Figure 4-8 and Table 4-2, core-shell catalyst has higher ECSA compared to the commercial Pt/C catalyst. This is occurring due to the higher efficiency in usage of platinum and having more active sites compared to the commercial platinum [25]. It is also worth mentioning that Pd@Pt nanoparticles before and after doping are having an almost same active surface area and this is happening due to their identical facet, size, and structure [26].

Figure 4-8 also shows the ORR polarization curves of core-shell and commercial platinum nanoparticles, measured in oxygen saturated 0.1 M $HClO_4$ electrolyte using the potential scan rate of 10 mV s^{-1} and the rotation rate of 1600 rpm. Due to existence of mixed diffusion and activation processes on rotating disk electrode, Koutecky-Levich equation (Equation 3) was used to obtain kinetic current and compare ORR activity of these samples [10].

$$\frac{1}{I} = \frac{1}{I_k} + \frac{1}{I_{lim}} \qquad (3)$$

Where I_k is the kinetic current (A) and I_{lim} is the limiting current measured at the potential of 0.4 V_{RHE} and I is the measured current.

Calculated kinetic currents were further normalized by platinum loading and ECSA to determine the mass and surface specific activity. As shown in Tafel plots of Figure 4-8, mass and specific activity of Pd@Pt-Co shows the enhanced activity compared to the undoped Pd@Pt and the commercial Pt/C. Mass activity of ORR on Pd@Pt-Co nanoparticle is 1.1 (A mg_{Pt}^{-1}), which is approximately 11 and 2.3 times higher compared to the commercial platinum and the undoped Pd@Pt at 0.9 V_{RHE}. All the calculated data are shown in Table 4-2. The superior activity of cobalt doped Pd@Pt is mainly induced by cobalt dopants interactions with Pt which can weaken the adsorption of oxygen species intermediates on Pt active sites after the reaction [14]. In addition, the geometric and electronic interaction between Pd and platinum shell has also further assisted, by shortening the Pt-Pt bonding distance through strain effects, in the enhanced activity of these core-shell nanoparticles [27].

The durability test was carried out to evaluate the stability of the electrocatalysts. A total of 20,000 cycles were scanned between 0.6 and 1.0 V_{RHE} at the scan rate of 100 mV s^{-1} for each sample, and the ECSAs, specific and mass activities were determined after ADT. As presented in Figure 4-8, the stability of Pd@Pt has greatly improved after the introduction of cobalt. As mentioned in Table 4-2, Pd@Pt has lost 19% of its initial mass activity after ADT which is much higher than the cobalt doped sample which its activity has dropped by only 2 % after 20k cycles. The substantial stability of cobalt doped nanoparticle is mainly originating from the beneficial role of cobalt which can help to enhance mass activity and preserve the nanoparticle octahedral shape simultaneously [28, 29].

Table 4-2 Electrochemical performance of cobalt doped Pd@Pt nanoparticles compared to Pd@Pt and commercial Pt/C.

Catalyst	ECSA ($m^2 g_{Pt}^{-1}$)	SA at 0.9 V_{RHE} (mA cm_{Pt}^{-2})	MA at 0.9 V_{RHE} (A mg_{Pt}^{-1})	Mass activity loss after ADT
Pt/C	69	0.43	0.09	-
Pd@Pt	73	1.49	0.48	19 %
Pd@Pt-Co	74	2.28	1.10	2%

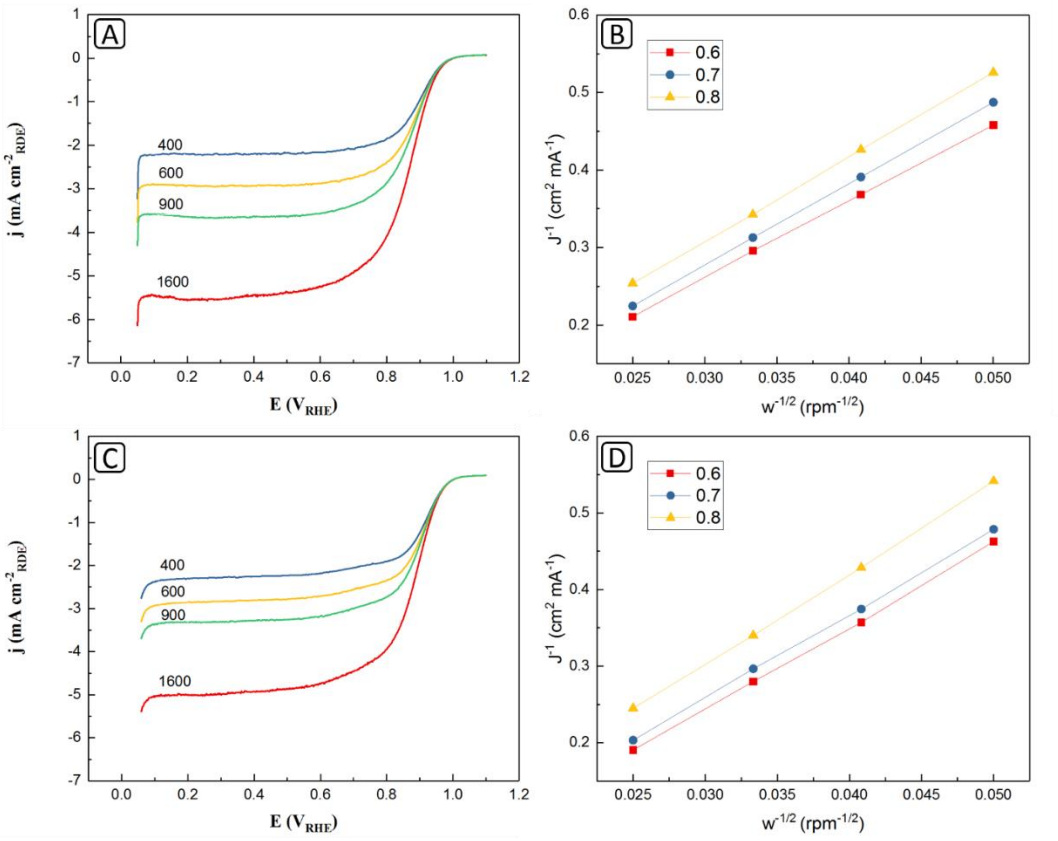

Figure 4-9 (A, C) LSV curves at different rotation rates recorded for ORR at Pd@Pt/C (A) and Pd@Pt-Co/C (C) catalysts in oxygen-saturated 0.1 M HClO4. Scan rate: 10 mV s^{-1}. Rotation rate: 400, 600, 900, 1600. (B, D) Koutecky-Levich plots of Pd@Pt and Pd@Pt-Co catalysts at different electrode potentials.

To find out the kinetics of ORR on core-shell nanoparticles, polarization curves at different rotation rates of 400 to 1600 were obtained [30]. Various ORR curves acquired at different rotation speeds are shown in the Koutecky–Levich (K–L) plots presented in Figure 4-9. The linear relation of j^{-1} and $\omega^{-0.5}$ is confirming the existence of first-order kinetics on these Pt-based nanoparticles and is endorsing the possibility of using Koutecky–Levich (K–L) equation (Equation 5) for calculations [31].

$$\frac{1}{j} = \frac{1}{j_k} + \frac{1}{j_{lim}} = \frac{1}{j_k} + \frac{1}{B\omega^{0.5}} \quad (4)$$

$$B = 0.62nFD^{2/3}\nu^{-1/6}C_0 \quad (5)$$

In RDE, reactant species are being supplied to the electrode surface with convention and increasing the electrode rotation speed can enhance the supplied reactant species and increase the monitored current. In order to have some idea about the proportionality of the current and rotation speed, Koutecky–Levich (K–L) equation, is being used. In this equation (Equation 4, 5), *j* is the measured current density using rotating disk electrode (RDE), *n* is the number of electrons involved in the reaction, *F* is Faraday's constant (96485 C/mol), *D* is the diffusion coefficient of O_2 in 0.1 M $HClO_4$ electrolyte, C_0 is the oxygen concentration in 0.1 M $HClO_4$ solution, and *v* is the kinematic viscosity of the solution.

It is clear in Figure 4-9 that fitted lines were plotted at different electrode potentials and each line is having a specific slope. As it is mentioned in Equation 4, slope of the fitted lines can be used to obtain B value and this parameter can be utilized to determine the number of participating electrons in ORR. The average number of transferred electrons was calculated to be 3.73 and 3.91 for Pd@Pt and cobalt doped Pd@Pt respectively. This result indicates that cobalt is assisting to the nanoparticle to get much closer to the desired four-electron pathway [32, 33].

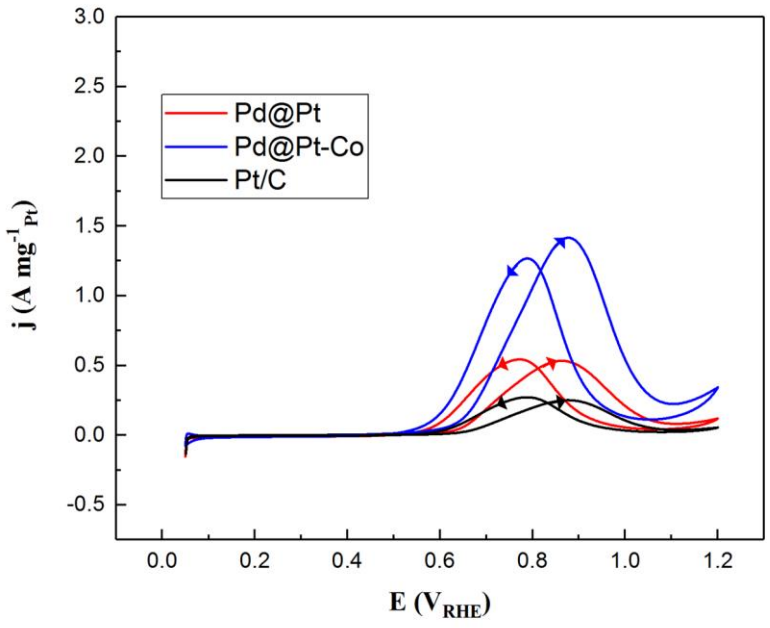

Figure 4-10 Cyclic voltammetry (CVs) of methanol oxidation for Pd@Pt/C and Pd@Pt-Co/C catalysts in 0.1 M $HClO_4$ and 1 M CH_3OH solution at 25 °C with a sweep rate of 10 mV s^{-1}.

Cobalt dopant has been also found to be advantageous in enhancing methanol oxidation activity of Pd@Pt NPs. Figure 4-10 shows the CV curves of Pd@Pt and Pd@Pt-Co nanoparticles in 0.1 M $HClO_4$ + 1 M CH_3OH electrolyte. The oxidation current density of the forward scan, which was recorded at the scan rate of 10 mV s^{-1}, is showing a significant enhancement in MOR activity after cobalt doping. Cobalt doped Pd@Pt exhibited a mass activity of 1.42 A mg_{Pt}^{-1}, which is 2.6 and 5.7 times higher than undoped Pd@Pt (0.53 A mg_{Pt}^{-1}) and commercial Pt/C (0.25 A mg_{Pt}^{-1}) respectively.

To know the origin of this enhancement in methanol oxidation, the MOR mechanism on Pt surface should be discussed. The summary of the MOR is mentioned as follows:

$$Pt + CH_3OH \rightarrow Pt\text{-}CO_{ads} + 4H^+ + 4e^- \quad (6)$$

$$Pt + H_2O \rightarrow Pt(OH)_{ads} + H^+ + e^- \quad (7)$$

$$Pt\text{-}CO_{ads} + Pt(OH)_{ads} \rightarrow CO_2 + 2Pt + H^+ + e^- \quad (8)$$

The main problem in methanol oxidation is CO oxidation, via the Langmuir–Hinshelwood mechanism, which requires a neighboring surface OH (Pt–OH) as shown in Equation 8. Adsorbed OH on platinum surface is produced by water dissociation and low capability of Pt in water dissociation has limited its ability for CO oxidation. As platinum is not able to oxidize CO and clean its surface from poisonous carbon monoxide for further reactions, its MOR activity will be diminished by time.

To overcome this challenge, cobalt is doped in platinum structure in this study. Cobalt which has high ability in water dissociation will enhance platinum activity in two strategies of bi-functional and electronic modification. In the first strategy, the required OH (Equation 7), for CO oxidation on Pt surface, will be adsorbed on cobalt surface and this will increase the platinum surface available active site by carbon monoxide elimination. In the second strategy, cobalt influence on platinum electronic structure modification and Pt-Pt bonding length contraction will be used to enhance Pt activity towards methanol oxidation.

This idea can be endorsed by having a look at MOR oxidation peaks shown in Figure 4-10. It is shown that there are two distinct peaks in forward and backward scans. The peak currents seen in the forward and backward scans are corresponding to methanol oxidation and oxidation of residual carbon species

from forward scan, respectively. In this case, the ratio between forward and backward peak current densities can be employed to investigate the CO tolerance of the catalyst. It is obvious in Figure 4-10 that cobalt doped Pd@Pt is having higher ratio of I_f/I_b and this is confirming that CO intermediates are mostly removed during forward scan and the lower oxidation peak in the backward scan is endorsing the existence of more fresh active site on its Pt surface.

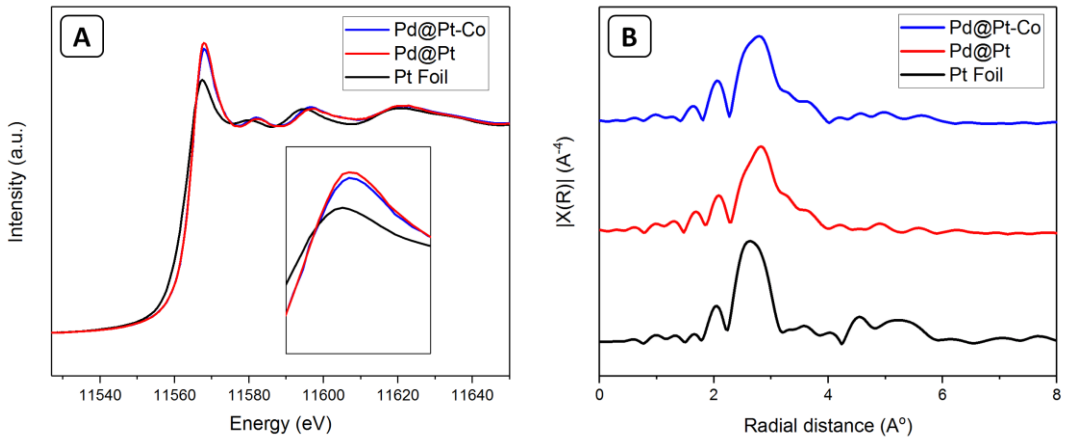

Figure 4-11 X-ray absorption studies of the Pd@Pt and cobalt doped Pd@Pt catalysts in comparison with Pt foil. A) The normalized XANES spectra at Pt L_3 edge and B) The K3-weighted Fourier transform spectra from EXAFS. Inset in (A) shows the enlarged spectra at Pt L_3 edge.

To correlate the catalytic activity and electronic structure of these nanoparticles, XAFS have been employed in this study. The characterization of the structure and behavior of the Pd@Pt-M (M=Transition metal dopant) system can be ideally carried out through ex-situ XAFS measurements. XAFS can probe the local and electronic structure of the absorbing atom by monitoring the absorption coefficient using tunable X-ray from a synchrotron light source and, can provide us information on the oxidation state, coordination number, and local symmetry of the atom of interest (Pt, dopant element, and Pd) before and after doping [34, 35]. In addition, the Pt $L_{3,2}$ edge can be also investigated to track the unoccupied densities of states of 5d electrons which essentially determines the catalytic activity [36]. In the Pt L_3 –edge XANES spectra, the whiteline (strong peak just above the threshold) intensity is associated with electronic transition from the Pt $2p_{3/2}$ orbital to the unoccupied 5d orbitals and the degree of oxidation of Pt as well [37].

In this study, all XAS measurements were conducted under fluorescence mode and were extracted and fitted using Athena and Artemis software. As it is clear in Figure 4-11, cobalt doped Pd@Pt showed lower white line peak intensity, which indicates electron transfer from Co to Pt [38].

Another imperative parameter in defining the catalytic activity of catalysts is the geometrical structure of nanoparticles which can be determined using EXAFS [39]. The EXAFS can be used to reveal the Pt−Pt distance in the Pd@Pt NPs before and after doping. The changes in the bond length and the interaction between Pt, dopant, and Pd atoms can affect the d-band structure of Pt and can be effective in optimizing the adsorption energy of intermediate oxygen species on Pt [14]. Fitting the presented EXAFS data in Figure 4-11, Fourier-transformed EXAFS shows that Co has slightly reduced the Pt-Pt bonding distance and this has assisted to weaken the Pt-O bond and further enhance its ORR activity [34]. This compressive strain is also observed by XRD pattern in Figure 4-7 and is reasonable based on the radius of cobalt atom. The platinum lattice contraction can be beneficial in terms of d-band center downshift and can diminish surface poisoning species and weaken hydroxyl adsorption energy.

4.4 Conclusions

We have demonstrated the synthesis of an advanced ORR catalyst based on Pd@Pt-Co octahedra by effectively combining three different strategies that involved utilization of transition metal, shape control, and the formation a core-shell. After 20k cycles of stability test, cobalt doped Pd@Pt have lost only 2 % of its initial activity and this is confirming that cobalt can be efficient in simultaneously enhancing catalytic activity and stabilizing the octahedral shape of Pd@Pt NPs by diminishing Pt dissolution. EXAFS results showed that the shorter Pt-Pt distance in Pd@Pt-Co NPs, is beneficial in weakening the Pt-O bond and enhancing the ORR activity. The lower whiteline intensity of Pd@Pt-Co XANES has also confirmed electron transfer from Co to Pt which can be beneficial in terms of catalytic activity. XRD patterns have also endorsed the lattice contraction in platinum with cobalt doping, which can be advantageous in terms of oxygen species adsorption on platinum surface.

4.5 References

1. *Xie, X., Gao, G., Pan, Z.et al., Large-scale synthesis of palladium concave nanocubes with high-index facets for sustainable enhanced catalytic performance. Scientific reports, 2015.* ***5****: p. 8515.*

2. *Wu, J., Zhao, J., Qian, H.et al., Deep insights into the growth pattern of palladium nanocubes with controllable sizes. RSC Advances, 2016.* ***6****(70): p. 66048-66055.*

3. *Zalineeva, A., Baranton, S., Coutanceau, C.et al., Octahedral palladium nanoparticles as excellent hosts for electrochemically adsorbed and absorbed hydrogen. Science Advances, 2017.* ***3****(2): p. e1600542.*

4. *Park, J., Zhang, L., Choi, S.-I.et al., Atomic layer-by-layer deposition of platinum on palladium octahedra for enhanced catalysts toward the oxygen reduction reaction. ACS nano, 2015.* ***9****(3): p. 2635-2647.*

5. *Xie, S., Choi, S.-I., Lu, N.et al., Atomic Layer-by-Layer Deposition of Pt on Pd Nanocubes for Catalysts with Enhanced Activity and Durability toward Oxygen Reduction. Nano Letters, 2014.* ***14****(6): p. 3570-3576.*

6. *Lim, J., Shin, H., Kim, M.et al., Ga–Doped Pt–Ni Octahedral Nanoparticles as a Highly Active and Durable Electrocatalyst for Oxygen Reduction Reaction. Nano Letters, 2018.* ***18****(4): p. 2450-2458.*

7. *Shao, M., Electrocatalysis in fuel cells: a non-and low-platinum approach. Vol. 9. 2013: Springer Science & Business Media.*

8. *Vielstich, W., Lamm, A. and Gasteiger, H.A., Handbook of fuel cells: fundamentals technology and applications. Vol. 2. 2003: Wiley New York.*

9. *ENERGY, U., Multi-year research, development, and demonstration plan. EE a. R. Energy, Ed., ed. USA, 2016: p. 3.4-17.*

10. *Zhang, H., Jin, M. and Xia, Y., Enhancing the catalytic and electrocatalytic properties of Pt-based catalysts by forming bimetallic nanocrystals with Pd. Chemical Society Reviews, 2012.* ***41****(24): p. 8035-8049.*

11. *Wang, C., Daimon, H., Onodera, T.et al., A general approach to the size-and shape-controlled synthesis of platinum nanoparticles and their catalytic reduction of oxygen. Angewandte Chemie International Edition, 2008.* ***47****(19): p. 3588-3591.*

12. *Choi, S.-I., Xie, S., Shao, M.et al., Synthesis and Characterization of 9 nm Pt–Ni Octahedra with a Record High Activity of 3.3 A/mgPt for the Oxygen Reduction Reaction. Nano Letters, 2013.* ***13****(7): p. 3420-3425.*

13. *Stamenkovic, V., Mun, B.S., Mayrhofer, K.J.et al., Changing the activity of electrocatalysts for oxygen reduction by tuning the surface electronic structure. Angewandte Chemie International Edition, 2006.* ***45****(18): p. 2897-2901.*

14. *Stamenkovic, V.R., Mun, B.S., Arenz, M.et al., Trends in electrocatalysis on extended and nanoscale Pt-bimetallic alloy surfaces. Nature materials, 2007.* ***6****(3): p. 241.*

15. *Lee, Y.-W., Lee, J.-Y., Kwak, D.-H.et al., Pd@ Pt core–shell nanostructures for improved electrocatalytic activity in methanol oxidation reaction. Applied Catalysis B: Environmental, 2015.* ***179****: p. 178-184.*

16. *Zhao, R., Liu, Y., Liu, C.et al., Pd@ Pt core–shell tetrapods as highly active and stable electrocatalysts for the oxygen reduction reaction. Journal of Materials Chemistry A, 2014.* ***2****(48): p. 20855-20860.*

17. *Xia, M., Liu, Y., Wei, Z.et al., Pd-induced Pt (IV) reduction to form Pd@ Pt/CNT core@ shell catalyst for a more complete oxygen reduction. Journal of Materials Chemistry A, 2013.* ***1****(46): p. 14443-14448.*

18. *Jia, Q., Liang, W., Bates, M.K.et al., Activity descriptor identification for oxygen reduction on platinum-based bimetallic nanoparticles: in situ observation of the linear composition–strain–activity relationship. Acs Nano, 2015.* ***9****(1): p. 387-400.*

19. *Petkov, V., Maswadeh, Y., Vargas, J.A.et al., Deviations from Vegard's law and evolution of the electrocatalytic activity and stability of Pt-based nanoalloys inside fuel cells by in operando X-ray spectroscopy and total scattering. Nanoscale, 2019.* ***11****(12): p. 5512-5525.*

20. *Chen, S., Wu, H., Tao, J.et al., Pt–Ni Seed-Core-Frame Hierarchical Nanostructures and Their Conversion to Nanoframes for Enhanced Methanol Electro-Oxidation. Catalysts, 2019.* ***9****(1): p. 39.*

21. *Zignani, S., Baglio, V., Sebastián, D.et al., Towards highly performing and stable ptni catalysts in polymer electrolyte fuel cells for automotive application. Materials, 2017.* ***10****(3): p. 317.*

22. *Inaba, M., Quinson, J., Bucher, J.R.et al., On the Preparation and Testing of Fuel Cell Catalysts Using the Thin Film Rotating Disk Electrode Method. JoVE (Journal of Visualized Experiments), 2018(133): p. e57105.*

23. *Nagasawa, K., Takao, S., Higashi, K.et al., Performance and durability of Pt/C cathode catalysts with different kinds of carbons for polymer electrolyte fuel cells characterized by electrochemical and in situ XAFS techniques. Physical Chemistry Chemical Physics, 2014.* ***16****(21): p. 10075-10087.*

24. *Shao, M., He, G., Peles, A.et al., Manipulating the oxygen reduction activity of platinum shells with shape-controlled palladium nanocrystal cores. Chemical Communications, 2013.* ***49****(79): p. 9030-9032.*

25. *Lim, B., Wang, J., Camargo, P.H.et al., Facile synthesis of bimetallic nanoplates consisting of Pd cores and Pt shells through seeded epitaxial growth. Nano letters, 2008.* ***8****(8): p. 2535-2540.*

26. *Adzic, R.R., Zhang, J., Sasaki, K.et al., Platinum monolayer fuel cell electrocatalysts. Topics in Catalysis, 2007.* ***46****(3-4): p. 249-262.*

27. *Bao, S., Vara, M., Yang, X.et al., Facile Synthesis of Pd@ Pt3–4L Core–Shell Octahedra with a Clean Surface and Thus Enhanced Activity toward Oxygen Reduction. ChemCatChem, 2017.* ***9****(3): p. 414-419.*

28. *Dai, S., Chou, J.-P., Wang, K.-W.et al., Platinum-trimer decorated cobalt-palladium core-shell nanocatalyst with promising performance for oxygen reduction reaction. Nature communications, 2019.* ***10****(1): p. 440.*

29. *Chong, L., Wen, J., Kubal, J.et al., Ultralow-loading platinum-cobalt fuel cell catalysts derived from imidazolate frameworks. Science, 2018.* ***362****(6420): p. 1276-1281.*

30. *Guo, S., Zhang, S., Wu, L.et al., Co/CoO nanoparticles assembled on graphene for electrochemical reduction of oxygen. Angewandte chemie international edition, 2012.* ***51****(47): p. 11770-11773.*

31. *Wang, Q., Zhou, Z.-Y., Lai, Y.-J.et al., Phenylenediamine-based FeN x/C catalyst with high activity for oxygen reduction in acid medium and its active-site probing. Journal of the American chemical Society, 2014.* ***136****(31): p. 10882-10885.*

32. *Yu, D., Zhang, Q. and Dai, L., Highly efficient metal-free growth of nitrogen-doped single-walled carbon nanotubes on plasma-etched substrates for oxygen reduction. Journal of the American Chemical Society, 2010.* ***132****(43): p. 15127-15129.*

33. *Qu, L., Liu, Y., Baek, J.-B.et al., Nitrogen-doped graphene as efficient metal-free electrocatalyst for oxygen reduction in fuel cells. ACS nano, 2010.* ***4****(3): p. 1321-1326.*

34. *Kitchin, J.R., Nørskov, J.K., Barteau, M.A.et al., Role of strain and ligand effects in the modification of the electronic and chemical properties of bimetallic surfaces. Physical review letters, 2004.* ***93****(15): p. 156801.*

35. *Beermann, V., Gocyla, M., Willinger, E.et al., Rh-Doped Pt–Ni Octahedral Nanoparticles: Understanding the Correlation between Elemental Distribution, Oxygen Reduction Reaction, and Shape Stability. Nano Letters, 2016.* ***16****(3): p. 1719-1725.*

36. *Jia, Q., Zhao, Z., Cao, L.et al., Roles of Mo Surface Dopants in Enhancing the ORR Performance of Octahedral PtNi Nanoparticles. Nano Letters, 2018.* ***18****(2): p. 798-804.*

37. *Cheng, X., Li, Y., Zheng, L.et al., Highly active, stable oxidized platinum clusters as electrocatalysts for the hydrogen evolution reaction. Energy & Environmental Science, 2017.* ***10****(11): p. 2450-2458.*

38. *Huang, X., Zhao, Z., Cao, L.et al., High-performance transition metal–doped Pt3Ni octahedra for oxygen reduction reaction. Science, 2015.* ***348****(6240): p. 1230-1234.*

39. *Wang, M., Árnadóttir, L., Xu, Z.J.et al., In Situ X-ray Absorption Spectroscopy Studies of Nanoscale Electrocatalysts. Nano-Micro Letters, 2019.* ***11****(1): p. 47.*

Chapter 5

5 Summary and Future Work

5.1 Conclusions

This thesis has focused on enhancing the activity and stability of proton exchange membrane fuel cell catalysts thorough various methods including metal-support interaction and use of facet-controlled nanoparticles. A series of shape-controlled Pd and Pd@Pt samples, supported on diverse carbon supports, were synthesized and their electrochemical performance were correlated with their electronic structure using powerful tools such as XAFS and XPS.

In chapter 2, uniform cubic Pd NPs were synthesized, using colloidal chemistry methods. Although there are various of studies focused on electrochemical performance of metal nanoparticles, the influence of outside organic layers, which is a vital component of colloidal chemistry, on the catalytic activity of nanoparticles is still unclear [1]. Various methods were used in this study to eliminate the surfactant, which is necessary to be used in colloidal chemistry synthesis and can hinder the optimum catalytic activity. The main objective in surfactant removal is to obtain a clean surface without altering the size, shape, and composition of the nanoparticle. To have an effectively clean catalyst, several methods were used and the influence of each method on both catalytic activity and surface features were discussed. It is found that the cleaning procedures such as UV-Ozone treatment and acid washing can passivate the metallic surface and leach out metal components respectively, while calcination can keep the nanoparticle perfectly unchanged and can enhance its activity to an incredibly high level compared to other methods [2]. The surface sensitive mode of X-ray absorption technique was also helpful to unveil the PVP-Pd interaction which involves electron transfer from PVP to Pd through N atom in the ring of capping agent [3].

In chapter 3, the influence of metal support interactions on the acquired electrochemical performance is thoroughly investigated. The formic acid oxidation on palladium nanocubes, which were grown on different carbon supports, was showing the superior mass activity on nitrogen doped carbon nanotube (NCNT) support [4]. The enhanced activity of palladium grown on NCNT, was mainly originating from the nitrogen interaction with palladium nanoparticles. It is found that nitrogen is having an electron donor role in contact with palladium and this manipulation of Pd

electronic structure can end in electron-enriched nanoparticles with an elevated FAO activity [5]. The nitrogen-palladium interaction can be also helpful in anchoring nanocubes and is the reason of smaller particle size, higher dispersion, and better stability in Pd/NCNT sample. Thus, the features of nitrogen in NCNT can be a big asset for enhancing stability, performance and metal utilization and can make the cathode catalysts one step closer to commercialization.

In chapter 4, Pd@Pt core-shell NPs were surface doped with cobalt and the ORR activity and stability results were correlated with the acquired information about their electronic structure using XAS. We have demonstrated the synthesis of an advanced ORR catalyst based on Pd@Pt-Co octahedra by effectively combining three different strategies that involved utilization of transition metal, shape control, and the formation of a core-shell structure [6]. The superior activity of cobalt doped Pd@Pt in acidic electrolyte was concluded to be resultant of electronic and geometrical modification of platinum. EXAFS results showed the shorter Pt-Pt distance in Pd@Pt-Co NPs, which can be beneficial in weakening the Pt-O bond, enhancing the ORR activity. XANES region of the XAS data also showed the electronic interaction between platinum and cobalt, which was an electron transfer from Co to Pt, determined from the lower whiteline intensity of Pd@Pt-Co in XAS data [7]. Having core-shell structure was also shown to be beneficial in reducing the utilized amount of platinum in the catalyst and this was determined to further enhance the mass activity of the catalyst with diminishing platinum loading. Accelerate durability test was also confirming the beneficial role of cobalt as a dopant in platinum structure which could simultaneously enhance catalytic activity and stabilize the octahedral shape of Pd@Pt NPs.

5.2 Future Work

As ORR is still known as an obstacle for commercialization of PEM fuel cell, a thorough fundamental study of ORR is necessary to overcome this challenge. In order to know the exact steps which are occurring in oxygen reduction reaction and distinguish the rate determining step, in-situ XAS can be used. Using in-situ XAS cell at the time of ORR can provide us information on the oxidation state, coordination number, and local symmetry of the atom of interest (Pt and Co) in a chemical environment as a function of electrode potential [8]. It can also show the active sites on the surface which will be vital in the synthesis of the future catalysts. For in situ measurements, by applying a specific potential in the double layer potential region, the electronic and geometric parameters of catalysts can be compared without interference of any type of ionic,

oxygen-containing intermediates, adsorption [9, 10]. By increasing the potential to the activation control region, absorbance of the oxygenated species and their influences on the catalyst can be compared with the results from double-layer region. Higher potential can be utilized to check the stability of the bimetal, e.g. Pt-Pd. Pt-Ni. This in-situ analysis will reveal information about the effect of the Pt thickness, catalysts facets, dopant element, and the inter-atomic distance of Pt-Pd and Pt-Pt on the catalytic activity of the synthesized catalysts at different potentials [11].

There is also another challenge in confirming the existence of core-shell nanoparticles using normal characterization methods. By utilizing the in-situ cell and applying various potentials, the position of palladium metal in the nanoparticle will be determined [12]. Having palladium metal just in the core will show palladium XAS data independent to the applied potential and platinum dense shell will preserve the palladium core from oxidation at high potentials.

5.3 References

1. *Lee, H., Utilization of shape-controlled nanoparticles as catalysts with enhanced activity and selectivity. RSC Advances, 2014.* ***4****(77): p. 41017-41027.*

2. *Niu, Z. and Li, Y., Removal and utilization of capping agents in nanocatalysis. Chemistry of Materials, 2013. 26(1): p. 72-83.*

3. *Borodko, Y., Humphrey, S.M., Tilley, T.D.et al., Charge-transfer interaction of poly (vinylpyrrolidone) with platinum and rhodium nanoparticles. The Journal of Physical Chemistry C, 2007. 111(17): p. 6288-6295.*

4. *Huang, H. and Wang, X., Pd nanoparticles supported on low-defect graphene sheets: for use as high-performance electrocatalysts for formic acid and methanol oxidation. Journal of Materials Chemistry, 2012. 22(42): p. 22533-2254.*

5. *Chen, Y., Wang, J., Liu, H.et al., Nitrogen doping effects on carbon nanotubes and the origin of the enhanced electrocatalytic activity of supported Pt for proton-exchange membrane fuel cells. The Journal of Physical Chemistry C, 2011. 115(9): p. 3769-3776.*

6. *Xie, S., Choi, S.-I., Lu, N.et al., Atomic layer-by-layer deposition of Pt on Pd nanocubes for catalysts with enhanced activity and durability toward oxygen reduction. Nano letters, 2014.* ***14****(6): p. 3570-3576.*

7. *Lim, J., Shin, H., Kim, M.et al., Ga–Doped Pt–Ni Octahedral Nanoparticles as a Highly Active and Durable Electrocatalyst for Oxygen Reduction Reaction. Nano Letters, 2018.* ***18****(4): p. 2450-2458.*

8. *Jia, Q., Zhao, Z., Cao, L.et al., Roles of Mo Surface Dopants in Enhancing the ORR Performance of Octahedral PtNi Nanoparticles. Nano Letters, 2018.* ***18****(2): p. 798-804.*

9. *Yang, Y., Wang, Y., Xiong, Y.et al., In Situ X-ray Absorption Spectroscopy of a Synergistic Co–Mn Oxide Catalyst for the Oxygen Reduction Reaction. Journal of the American Chemical Society, 2019.* ***141****(4): p. 1463-1466.*

10. *Arruda, T.M., Shyam, B., Lawton, J.S.et al., Fundamental Aspects of Spontaneous Cathodic Deposition of Ru onto Pt/C Electrocatalysts and Membranes under Direct Methanol Fuel Cell Operating Conditions: An in Situ X-ray Absorption Spectroscopy and Electron Spin Resonance Study. The Journal of Physical Chemistry C, 2010.* ***114****(2): p. 1028-1040.*

11. *Jia, Q., Liang, W., Bates, M.K.et al., Activity descriptor identification for oxygen reduction on platinum-based bimetallic nanoparticles: in situ observation of the linear composition–strain–activity relationship. Acs Nano, 2015.* ***9****(1): p. 387-400.*

12. *Sasaki, K., Marinkovic, N., Isaacs, H.S.et al., Synchrotron-Based In Situ Characterization of Carbon-Supported Platinum and Platinum Monolayer Electrocatalysts. ACS Catalysis, 2016.* ***6****(1): p. 69-76.*

Curriculum Vitae

Name: Ali Feizabadi

Post-secondary Education and Degrees:

The University of Western Ontario
London, Ontario, Canada
2017-present, M.Sc. Candidate in Chemistry

Amirkabir University of Technology (Tehran Polytechnic)
Tehran, Tehran, Iran
2012-2017, B.Sc. in Materials and Metallurgical Engineering

Honors and Awards:

WISE (Western's Ideas for Sustainability and the Environment) Competition Award
2018

CMC -NanoCanada Conference Support Award
2018

Nanofabrication Supporting Award
2017

Nanotechnology Research Supporting Award
2017

CLS Graduate Student Travel Award
2017-2018

Related Work Experience

Teaching Assistant in Chemistry
The University of Western Ontario
2017-2019

VP communication of The Chemistry Graduate Student
The University of Western Ontario
2018-2019

Member of Finance committee of SOGS (School of Graduate Studies)
2018-2019

Member of Financial Assistance committee of Western PSAC (Public Service Alliance of Canada)
2018-2019

Accomplishing The Leadership Education Program-Group Leadership, 2019

Academic Travel to CLS (Canadian Light Source) in Saskatoon 2018-2019

Accomplishing The Teaching Assistant Training Program (TATP) 2017

Publications:

1. **A.Feizabadi**, M. SalehiDoolabi, S.K. Sadrnezhaad, D. SalehiDoolabi, M. AsadiZarch "MCDM selection of pulse parameters for best tribological performance of Cr-Al2O3 nano-composite from trivalent chromium bath"
   (Journal of Alloys and Compounds - Dec 2017)
2. **A.Feizabadi**, M. Rezaei, M. SalehiDoolabi, S.K.Sadrnezhaad, "Cyclic oxidation characteristics of HVOF thermal-sprayed NiCoCrAlY and CoNiCrAlY coatings at 1000 °C"
   (Journal of Alloys and Compounds - May 2018)
3. M. SalehiDoolabi, B. Ghasemi, S.K. Sadrnezhaad, **A. Feizabadi,** A. HabibollahZadeha "Comparison of isothermal with cyclic oxidation behavior of "Cr-aluminide" coating on Inconel 738LC at 900 °C"
   (Oxidation of Metals journal - October 2016)

Conference Presentations:

1. **A. Feizabadi**, T.K. Sham, X.A. Sun, "Catalytic Performance of Pd Nanocubes after Removal of Surfactant and Capping Agents."
   (Poster presented at: Innovation 360 and NanoCanada's 2nd National Conference, 2018, Toronto, Canada)
2. **A. Feizabadi**, T.K. Sham, X.A. Sun, "XAS study on the Pd@Pt-M(M=Transition Metal) core@shell catalyst and tracking the correlation between the electronic structure and the catalytic activity of the catalyst in ORR."
   (Poster presented at: 102nd Canadian Chemistry Conference and Exhibition (CCCE2019), 2019, Québec, Canada)